Research Repository UCD

Title	Analysis, Prediction and Mitigation of Nonlinearity-induced Spurs and Noise in Fractional-N Frequency Synthesizers
Authors(s)	Mazzaro, Valerio
Publication date	2022
Publication information	Mazzaro, Valerio. “Analysis, Prediction and Mitigation of Nonlinearity-Induced Spurs and Noise in Fractional-N Frequency Synthesizers.” University College Dublin. School of Electrical and Electronic Engineering, 2022.
Publisher	University College Dublin. School of Electrical and Electronic Engineering
Item record/more information	http://hdl.handle.net/10197/29778

Downloaded 2026-04-24 17:21:40

The UCD community has made this article openly available. Please share how this access benefits you. Your story matters! (@ucd_oa)

© Some rights reserved. For more information

Analysis, Prediction and Mitigation of Nonlinearity-induced Spurs and Noise in Fractional-N Frequency Synthesizers

Valerio Mazzaro

Dissertation submitted to
the National University of Ireland
in partial fulfilment of the requirements
of the degree of Doctor of Philosophy

Supervisor: Professor Peter Michael Kennedy

School of Electrical and Electronic Engineering, University College Dublin

May 2022

Acknowledgements

Firstly, I would like to thank Professor Kennedy for offering the opportunity to pursue the degree at University College Dublin.

I am grateful towards my family that supported me financially and emotionally along all my studies.

Last but not least, I wish to express my appreciation to my girlfriend, Alessia, my best friend, Giovanni, and all the people that accompanied me through this journey.

Valerio Mazzaro

Cava de' Tirreni, May 2022

Contents

List of Figures

List of Tables

Abstract

Fractional-N frequency synthesizers are commonly used in communication systems. A divider controller is employed within a conventional divider-based fractional-N frequency synthesizer to achieve the desired fractional division ratio. A MultistAge Noise SHaping (MASH) Digital Delta-Sigma Modulator (DDSM) is usually used as the divider controller because of its high-pass shaped quantization error and ease of implementation. Among contributors to the output phase noise of a conventional fractional-N frequency synthesizer, the noise of the divider controller is normally high-pass shaped and its in-band contribution can be ignored under the assumption of linearity. In the presence of nonlinearity, however, the phase noise contribution of the divider controller becomes prominent in-band, denoted folded noise, and spurious tones usually appear. The causes of divider controller-induced spurious tones in the long-term spectrum have been the focus of research for many years and efforts continue to be made to identify and mitigate nonlinearity-induced spurs in synthesizers.

In this thesis, we analyze the generation of nonlinearity-induced folded noise in fractional-N frequency synthesizers with MASH-based divider controllers and an accurate prediction method is described. The phenomena of spur immunity and sub-fractional spurious tones, called “horn spurs”, are analyzed in MASH modulators. A family of DDSMs is introduced that allows one to achieve enhanced performance in terms of nonlinearity-induced noise. The so-called ENOP DDSMs are provably spur free in the presence of static polynomial nonlinearities of a specified order. Moreover, another family of DDSMs is introduced whose quantization error is inherently immune from spurs when interacting with a static nonlinearity. The so-called INIS-DDSMs are suitable for digital to analog transduction, such as for DCO controllers.

List of Publications

- **V. Mazzaro** and M. P. Kennedy, “Another moving Spur Phenomenon observed in a MASH-based Fractional-N PLL,” *2019 30th Irish Signals and Systems Conference (ISSC)*, 2019, pp. 1–5.

- **V. Mazzaro** and M. P. Kennedy, “Observations concerning “Horn Spurs” in a MASH-based Fractional-N CP-PLL,” *2019 26th IEEE International Conference on Electronics, Circuits and Systems (ICECS)*, 2019, pp. 17–20.

- **V. Mazzaro** and M. P. Kennedy, “Mitigation of “Horn Spurs” in a MASH-Based Fractional-N CP-PLL,” *IEEE Transactions on Circuits and Systems II: Express Briefs*, vol. 67, no. 5, pp. 821–825, May. 2020.

- **V. Mazzaro**, L. Gleeson and M. P. Kennedy, “Analysis and Prediction of Spurs in a Fractional-N Frequency Synthesizer with Discontinuous Nonlinearity,” *2020 31th Irish Signals and Systems Conference (ISSC)*, 2020, pp. 1–6.

- **V. Mazzaro** and M. P. Kennedy, “A Curious Result concerning Spur Generation in MASH 1-1-1 based Fractional-N CP-PLLs with a Second-Order Nonlinearity,” *2020 27th IEEE International Conference on Electronics, Circuits and Systems (ICECS)*, 2020, pp. 1–4.

- **V. Mazzaro** and M. P. Kennedy, “Spur Immunity in MASH-Based Fractional-N CP-PLLs With Polynomial Nonlinearities,” *IEEE Transactions on Circuits and Systems I: Regular Papers*, vol. 68, no. 6, pp. 2295–2306, June 2021.

- **V. Mazzaro** and M. P. Kennedy, “Folded Noise Prediction in Nonlinear Fractional-N Frequency Synthesizers,” *IEEE Transactions on Circuits and*

Systems I: Regular Papers, vol. 68, no. 10, pp. 4038–4048, Oct. 2021.

- M. P. Kennedy, **V. Mazzaro** and D. Mai, “Nonlinearity-Induced Spurs in Fractional-N Frequency Synthesizers,” *IEEE Transactions on Circuits and Systems II: Express Briefs*, doi: 10.1109/TCSII.2022.3169224..
- **V. Mazzaro** and M. P. Kennedy, “A Family of $\Delta\Sigma$ Modulators with High Spur Immunity and Low Folded Nonlinearity Noise when used in Fractional-N Frequency Synthesizers,” *IEEE Transactions on Circuits and Systems I: Regular Papers*, vol. 69, no. 11, pp. 4499-4509, Nov. 2022.
- **V. Mazzaro** and M. P. Kennedy, “Immunity of ENOP-based Fractional-N Frequency Synthesizer to Wandering and Horn Spurs,” *2022 17th IEEE International Conference on PhD Research in Microelectronics and Electronics (PRIME)*, 2022, pp. 1-4.
- **V. Mazzaro** and M. P. Kennedy, “Implementation of ENOP and Hybrid Nested ENOP Divider Controllers for Fractional-N Frequency Synthesizers,” *IEEE Transactions on Circuits and Systems I: Regular Papers*, in preparation.
- **V. Mazzaro** and M. P. Kennedy, “A Family of $\Delta\Sigma$ Modulators with Inherent Spur Immunity when interacting with a Nonlinearity,” *IEEE Transactions on Circuits and Systems II: Express Briefs*, in preparation.
- **V. Mazzaro** and M. P. Kennedy, “Apparatus for mitigating nonlinearity-induced spurs and noise in a fractional-N frequency synthesizer,” US Patent 63/292,350, Dec. 2021, provisional application.
- **V. Mazzaro** and M. P. Kennedy, “Digital delta sigma modulator with inherent spur immunity after nonlinear distortion,” US Patent 63/329,678, Apr. 2022, provisional application.

Chapter 1

Introduction

This chapter briefly introduces the topic of nonlinearity-induced phase noise and spurs in fractional-N frequency synthesizers. It then summarizes the structure and contributions of the thesis.

1.1 Spurious tones and folded noise in fractional-N frequency synthesizers

1.1.1 Nonlinearity-induced fractional spurious tones

Frequency synthesizers are used in various electronic systems for communications and clocking purposes. A generic fractional-N frequency synthesizer is shown schematically in Fig. 1.1. Variants of this basic architecture may include prescalers and digital to time converters.

A feedback loop is used in order to generate a precise output frequency. The integer-N frequency synthesizer involves a multimodulus divider (MMD) with a *fixed* division ratio, i.e. no control to the division ratio is required. One major limitation of having a fixed division ratio is that the frequency steps at the output

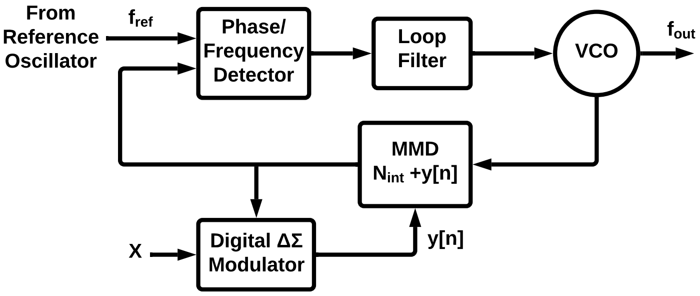

Figure 1.1: Block diagram of a generic fractional-N frequency synthesizer.

may be too large. In steady-state operation,

$$f_{OUT} = N_{int} f_{ref}, \tag{1.1}$$

where f_{out} and f_{ref} are the output frequency and the reference input at the phase/frequency detector (PFD) and N_{int} is the integer division ratio. The output frequency can be set with a minimum frequency resolution equal to the input reference frequency f_{ref}. This is not sufficient in many application scenarios and it is often desirable to have finer frequency resolution at the output.

The fractional-N frequency synthesizer provides a solution to enable a fractional ratio between the output and the input reference frequencies [1,2]. By dithering the instantaneous division ratio $N_{div}[n]$ using a divider controller, a fractional division ratio can be achieved. For a local oscillator application, the fixed output frequency can be expressed by

$$f_{OUT} = (N_{int} + \alpha)\, f_{REF} = \left(N_{int} + \frac{X}{M}\right) f_{REF}, \tag{1.2}$$

where α is the desired fractional value of the division ratio, X is the input to the divider controller which controls the division ratio, and M is the modulus of the divider controller. In a digital implementation, typically, $M = 2^B$ for a fixed-bus width B-bit divider controller and this is assumed throughout the thesis.

Despite the fact that the long-term average of the division ratio can be set very precisely, the change of the instantaneous division ratio will introduce quantization noise. To minimize the impact on the in-band noise, it is preferred that the phase noise contribution of the divider controller should be high-pass shaped. A Multi-stAge noiSe sHaping digital delta-sigma modulator (MASH DDSM) is conventionally used for this purpose.

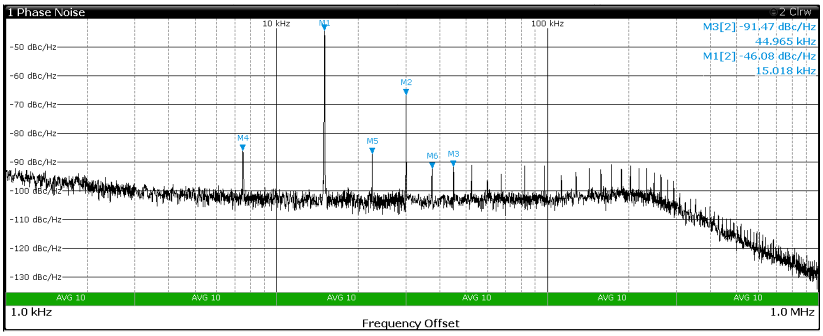

Figure 1.2: Measured output phase noise spectrum with spurious tones (marked with blue markers) from a commercial fractional-N frequency synthesizer [3].

In a realistic fractional-N frequency synthesizer, nonlinearity exists and nonlinearity-induced excess noise and spurious tones at constant offsets from the nominal output frequency will appear. Fig. 1.2 shows a typical phase noise measurement from a commercial fractional-N frequency synthesizer [4]. Different groups of spurious tones can be distinguished. Among them, the fractional spurs are the most well known. These tones appear at the fractional frequency αf_{ref} and harmonics of it. The fractional spurs are particularly bothersome in a near-to-integer condition, i.e. when α has a value very close to zero or one. In fact, in this case the fractional spurs, also called integer boundary spurs, are likely to be located inside the bandwidth of the synthesizer and, therefore, they are not attenuated by the loop filter. These spurious tones will deteriorate the system performance, for example, in a local oscillator application, due to noise overlapping from the unwanted conversion they cause. There has been much research investigating the mechanisms that cause such *fixed* spurs [5, 6].

1.1.2 Horn Spurs

Another group of spurious tones are the so called *horn spurs.* Like fractional spurs, horn spurs are fixed in frequency. It means that their positions in the frequency spectrum do not change with time, as long as the DDSM parameters remain unchanged. Horn spurs are so called because they typically appear in pairs. They belong to what are sometimes loosely called sub-fractional spurs. In practice, they can be located at frequencies that are lower than the fractional frequency αf_{ref}. In particular, their position is a function of α and the DDSM's initial condition [7]. Horn spurs can be troublesome because they can arise inside the bandwidth even though the fractional term α is far from an integer value. An example of this is shown in Fig. 1.3.

Figure 1.3: Measured output phase noise spectrum showing multiple pairs of horn spurs and from commercial fractional-N frequency synthesizers. The fractional spur of αf_{ref} is visible and at ≈2.2 MHz.

1.1.3 Wandering spurs

A phenomenon of time-varying spurs, termed *wandering spurs*, has also been reported in measurements and simulations of fractional frequency synthesizers for RF applications [8]–[11]. These spurs move with a linearly changing frequency across the short-term output phase noise spectrum of a DDSM-based fractional-N frequency synthesizer, as shown in Fig. 1.4. This phenomenon is not desirable in a system that requires a short period of operation, for example, a RADAR system [12], where the spurs can be misinterpreted as targets.

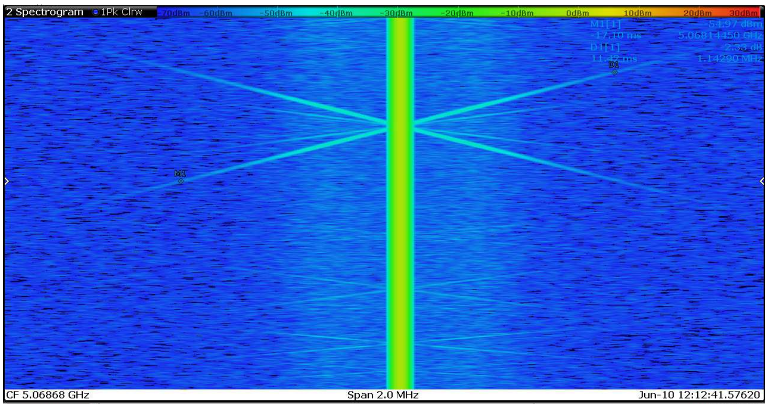

Figure 1.4: Measured output phase noise spectrogram from a commercial fractional-N frequency synthesizer. The X-shaped traces are produced by the wandering spurs.

1.1.4 Folded Noise

As anticipated above, the presence of nonlinearities in the system does not only cause the generation of a set of spurious tones, but it also leads to the introduction of excess noise due to noise folding. This additional nonlinearity-induced noise is commonly referred to as *folded noise*. It typically manifests itself as an elevated low-frequency noise floor. The nonlinearity-induced folded noise can be troublesome as it can degrade the overall in-band phase noise of the synthesizer. For this reason, it is important to analyze the folded noise in order to predict it and to understand how to mitigate it.

1.2 Contributions of the thesis

This thesis has four major contributions. The first is an investigation of the generating mechanism of the horn spurs. The cause of this spectral phenomenon in a conventional fractional-N frequency synthesizer is identified. Then, techniques are proposed in order to mitigate them.

The second contribution is an analysis of the generation mechanism of fractional spurs. The spur-related behavior of conventional DDSMs is investigated in the case of static polynomial nonlinearities. This shows how to tackle the generation of fractional spurs.

The third contribution is providing a detailed and comprehensive prediction method for the folded noise for any nonlinearity. This enables one to understand how to minimize the noise once the nonlinearity is given.

The fourth contribution is using the knowledge obtained in the previous steps to design and implement new families of DDSMs that provide enhanced performance in terms of minimizing the spurs and noise induced by a nonlinearity.

1.3 Thesis outline

In Chapter 2, some background on the operation of a conventional fractional-N frequency synthesizer and methods for simulating it are presented. In Chapter 3, divider controller-induced horn spurs in a MASH DDSM-based fractional-N frequency synthesizer are discussed. Chapter 4 analyzes conditions for the existence of nonlinearity-induced spurs in some conventional DDSMs. Then, the analysis of nonlinearity-induced folded noise is discussed, and a method for predicting the level of this component is provided in Chapter 5. A new family of DDSMs with Enhanced Nonlinearity-induced nOise performance (ENOP) when used as divider controllers is presented in Chapter 6, and various implementations thereof are discussed in Chapter 7. Moreover, another family of DDSMs with inherent Immunity from Nonlinearity-Induced Spurs (INIS) when used in a digital to analog converter is discussed in Chapter 8. The conclusions of the thesis and suggestions for future work are presented in Chapter 9.

1.4 Original contributions of the thesis

The original contributions of this thesis are as follows:

- Analysis and mitigation of wandering spurs in a MASH 1-1-1 DDSM-based conventional charge-pump fractional-N frequency synthesizer [13].
- Analysis of spur immunity in MASH-based fractional-N frequency synthesizers with polynomial nonlinearity [14].
- Analysis and prediction of folded noise in fractional-N frequency synthesizers [15].
- Proposal and analysis of a new family of DDSMs with high spur immunity and low folded noise when used as the divider controller of a fractional-N frequency synthesizer [16], [17], [18].
- Proposal and analysis of a new family of DDSMs with inherent spur immunity when used as a digital to analog transducer, such as in the case of a DCO controller [19].

Chapter 2

Background and simulation model

Before going into the details of the analysis, prediction and mitigation of nonlinearity-induced spurious tones and folded noise in fractional-N frequency synthesizers, we need to provide an overview of the system, the problematic effect of nonlinear distortion and a model for simulating these two.

2.1 Fractional-N PLLs

Fractional-N frequency synthesizers are typically implemented using a phase locked loop (PLL) structure as shown in Fig. 1.1. A conventional PLL generates an output signal whose phase is locked to that of a reference signal such that the output frequency, f_{out}, is a multiple of the reference, f_{ref}. In more detail, the output signal is generated by either a voltage controlled oscillator (VCO) or a digitally controlled oscillator (DCO). Then, f_{out} is divided down using a multi-modulus divider (MMD) by a factor N_{div}. The divided signal is compared to the reference signal by a phase frequency detector (PFD). The output of the PFD goes through a loop filter, whose output controls the oscillator and closes the loop. Practical implementations may vary from Fig. 1.1, or include other functioning blocks [20]–[23]. In particular, in this thesis we will often refer to the conventional type II charge pump (CP) PLL [24]. This is a PLL where the PFD is accompanied by a CP block which translates the detected input phase error into electric charge stored or removed by a capacitor. We will not dwell either on the details of the CP PLLs or the variety of different architectures of PLLs, as it is not the goal of this work.

As anticipated in the previous Chapter, the main advantage of fractional-N PLLs is the better frequency resolution resulting from a fractional division ratio N_{div}. This latter is typically implemented with the use of a divider controller. In practice N_{div} is obtained as the sum of two integer values that are N_{int} and the output of the divider controller $y[n]$. In most cases the divider controller is implemented with a digital $\Delta\Sigma$ modulator. While N_{int} is fixed, the integer $y[n]$ changes with time, giving, on average, a fractional value α that can be expressed by the ratio $\frac{X}{M}$, where M is the modulus and X is the constant input of the modulator. As a consequence, the output signal frequency is given by:

$$f_{out} = \left(N_{int} + \frac{X}{M}\right) f_{ref}, \tag{2.1}$$

During the operation of the system, the DDSM tries to approximate the fractional value $\frac{X}{M}$ with the integer $y[n]$, introducing a quantization error. This error will be accumulated and translated to the phase of the output signal generated by the multimodulus divider (MMD). As a result, the input signals at the phase-frequency detector (PFD) will present a phase difference that depends on the accumulation of the quantization error coming from the DDSM. The accumulated quantization error e_{acc} is designed to have a high-pass filtered and spur-free spectrum. In practice, spurious tones are regenerated at the output of the CP due to interaction between e_{acc} and nonlinearity in the PFD/CP.

2.2 Modulation error and noise

In fractional-N frequency synthesizers, a DDSM is typically used for implementing the divider controller. In particular, the modulator is characterized by a digital input word, X, and a modulus M, such that the DDSM output, denoted $y[n]$, has a mean value equal to X/M, which is also denoted by α. The DDSM introduces a quantization error, denoted $e_q[n]$, where:

$$e_q[n] = y[n] - \alpha. \tag{2.2}$$

A typical implementation of a DDSM is the error feedback modulator (EFM). It is shown in Fig. 2.1. The modulator is composed of a quantizer that generates the output $y[n]$. Moreover, the quantizer introduces an error while performing

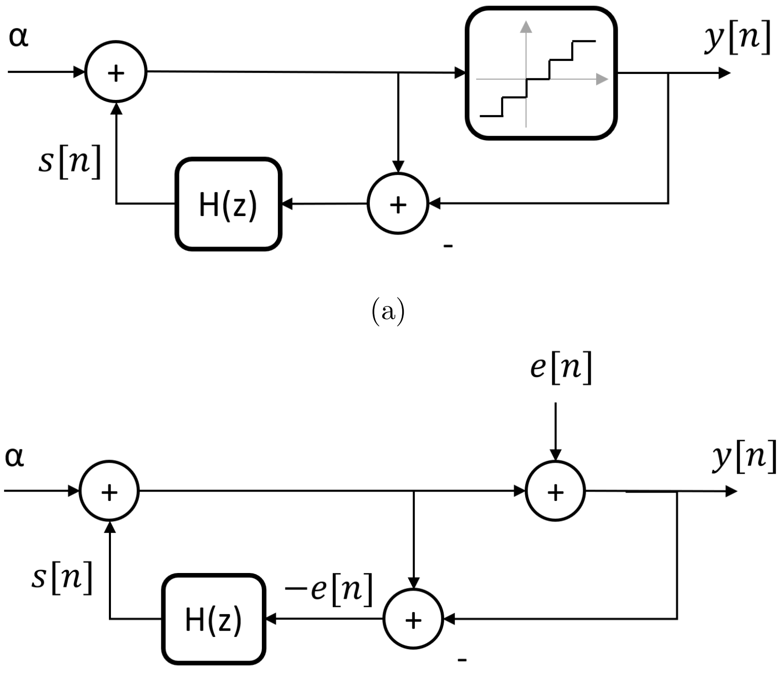

(a)

(b)

Figure 2.1: (a) Block diagram of an error feedback modulator (EFM) with a truncation quantizer and (b) its linearized model.

the truncation. This error is denoted as $e[n]$, as shown in the linearized EFM model in Fig. 2.1(b).

The quantization error, $e_q[n]$, is related to the signal $e[n]$ by the noise transfer function. The latter is typically denoted as $NTF(z)$ and it is defined such that:

$$E_q(z) = NTF(z)E(z), \tag{2.3}$$

where $E_q(z)$ and $E(z)$ are the Z-transforms of $e_q[n]$ and $e[n]$, respectively. In the case of an EFM, one can notice that the noise transfer function is given by:

$$NTF(z) = 1 - H(z). \tag{2.4}$$

Therefore, the transfer function $H(z)$ is designed in order to obtain the desired noise transfer function. One important goal of the DDSM is to high-pass shape the quantization noise. This is done so that the noise introduced into the PLL by the divider controller is filtered by the closed loop transfer function of the synthesizer. In order to do so, the $NTF(z)$ of the DDSM is usually chosen as a power of $(1 - z^{-1})$. Conventional EFMs are characterized by having an NTF equal to

$$NTF(z) = (1 - z^{-1})^l, \tag{2.5}$$

where l is the order of the modulator.

Another family of DDSMs is the MASH modulators. This type of modulator is composed of a cascade of EFM stages. The outputs of the individual stages are combined in an error cancellation network, resulting in a noise transfer function such as the one in (2.5). In order to minimize the hardware complexity of each stage, MASH DDSMs are typically implemented as a cascade of first-order EFMs, also denoted as EFM1, where the error signal $-e[n]$ of each stage represents the input of the one that follows. Fig. 2.2 shows an example of a MASH 1-1-1 DDSM which is composed of the cascade of three EFM1 stages. The advantage of the MASH structure is that it is unconditionally stable.

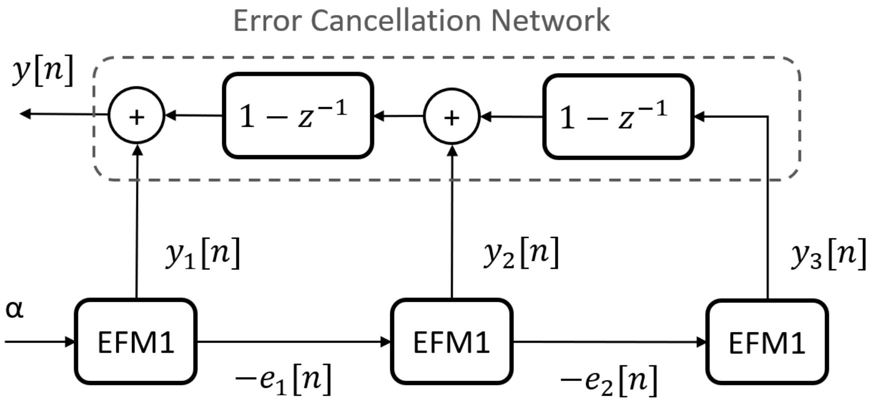

Figure 2.2: Block diagram of a conventional MASH 1-1-1 DDSM.

Another important goal of the DDSM is to randomize the quantization error. This aspect is essential to make the spectrum of $y[n]$ spur-free. Unfortunately, it is not possible to obtain perfect randomization since the DDSM is a finite state machine. Therefore, its output $y[n]$, as well as the quantization error, will be periodic when α is fixed. In order to obtain a smooth spectrum for the quantization noise one should maximize the period of $y[n]$, also called the cycle length. This is usually achieved by additive pseudorandom dithering [25]. In particular, if not differently stated, we will consider a first-order shaped dither instead of an unfiltered one. This is because the latter has the drawback of introducing a low frequency noise tail in the output phase noise. Moreover, as has been remarked in previous work [25], first-order shaped dither is sufficient to randomize the quantization error of a MASH 1-1-1, which is the conventional modulator that we mostly refer to in this thesis.

As depicted in Fig.1.1, the output of the DDSM is fed to an MMD that divides down the output frequency f_{out}, by a quantity $(N_{int} + y[n])$. Thus, (2.2) suggests that the quantization error $e_q[n]$ provides information about the error of the instantaneously synthesized frequency due to the modulator. Consequently, the accumulation of $e_q[n]$, denoted $e_{acc}[n]$, relates to the phase error introduced into the loop by the DDSM. The accumulated quantization error is defined recursively as

$$e_{acc}[n] = e_q[n] + e_{acc}[n-1], \tag{2.6}$$

or, equivalently, in the Z-domain

$$E_{acc}(z) = (1 - z^{-1})^{-1} E_q(z). \tag{2.7}$$

This latter, in conjunction with (2.3), tells us that

$$E_{acc}(z) = (1 - z^{-1})^{-1} NTF(z) E(z). \tag{2.8}$$

It is important to bear in mind what $e_{acc}[n]$ represents, and how it relates to the other error signals. In fact, the accumulated quantization error will be used frequently in the analyses and discussions presented in this thesis. Fig. 2.3 shows an example of the time waveform and power spectral density of $e_{acc}[n]$ in the case of a MASH 1-1-1. One may notice that, because of a proper design of the modulator, the PSD is spur-free and high-pass shaped.

Let us consider the case where the synthesizer is a type-II charge pump (CP) PLL. We refer to the model presented by Perrott *et al.* in [20]. Considering a tristate PFD, the frequency-domain model of the linearized synthesizer is shown in Fig. 2.4. It is worth noting that, if there are no sources of noise in the loop other than that associated with the divider controller, the phase error experienced at the input of the phase frequency detector (PFD) when the system is locked can be expressed as [20]:

$$\Delta\phi_{in}[n] = \frac{2\pi}{N_{div}} e_{acc}[n-1] + \Delta\phi_{os}, \tag{2.9}$$

where $\Delta\phi_{os}$ is a phase offset that may be present in the input phase error, in addition to the term in $e_{acc}[n]$. In more detail, a non-zero value of $\Delta\phi_{os}$ can result from the presence of nonlinearities in the system or by the voluntary introduction of offsets into the loop, such as charge pump (CP) bleed current [24]. For practical reasons, let use introduce a dimensionless term τ_{os}, defined as $\frac{N_{div}}{2\pi}\Delta\phi_{os}$. Then, the expression in (2.9) can be rewritten as:

$$\Delta\phi_{in}[n] = \frac{2\pi}{N_{div}}\left(e_{acc}[n-1] + \tau_{os}\right). \tag{2.10}$$

Let us assume, for the moment, that there are no intentionally added offsets and that the system is linear. As a consequence, τ_{os} is zero and $\Delta\phi_{in}[n]$ is proportional

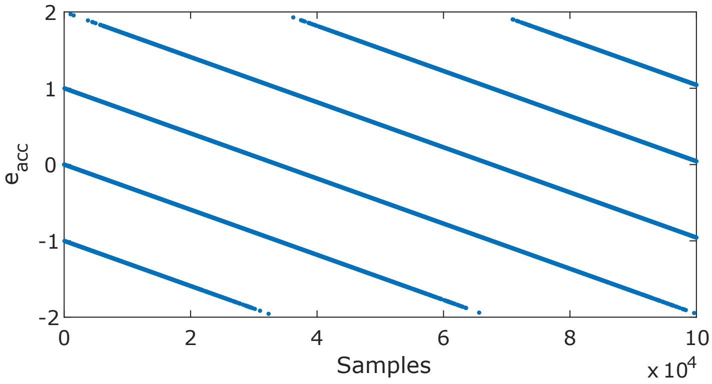

(a)

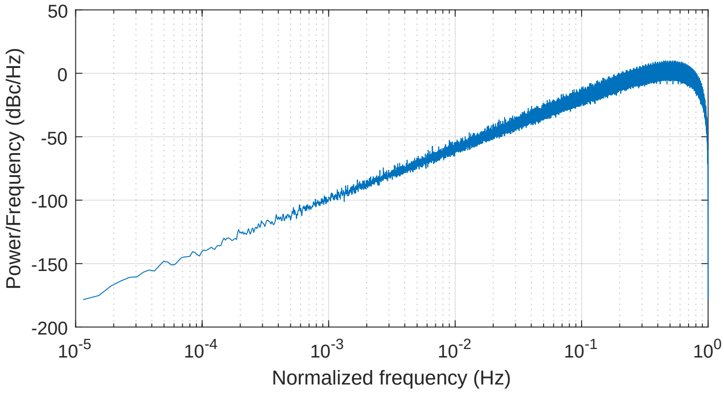

(b)

Figure 2.3: Simulated (a) time waveform and (b) power spectral density (PSD) of the accumulated quantization error e_{acc} in the case of a MASH 1-1-1 DDSM with $\alpha = 31/2^{20}$.

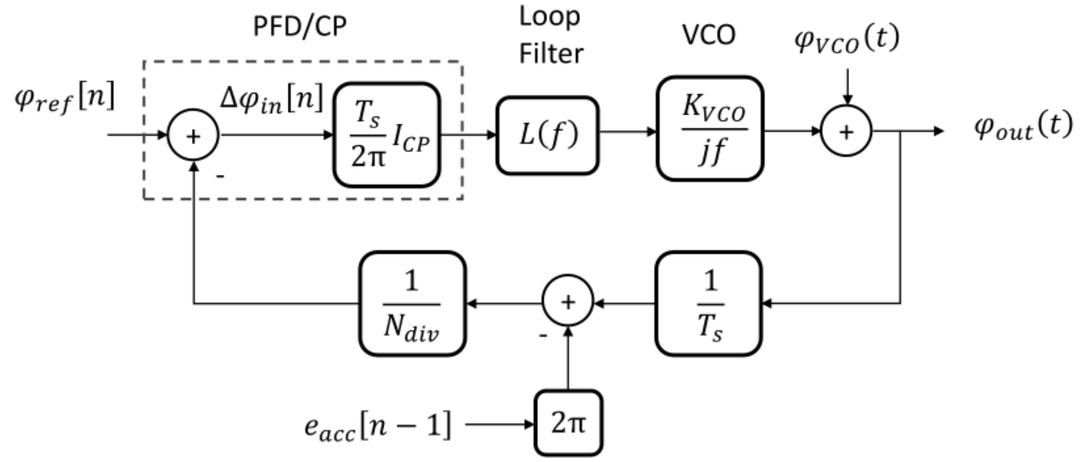

Figure 2.4: Linearized frequency-domain model presented in [20].

to a delayed version of $e_{acc}[n]$. Then, the noise component of the output phase, $\phi_{out}(t)$, due to the DDSM modulation is a filtered version of the PSD of $e_{acc}[n]$.

This is true as long as the system is linear. Unfortunately, a real PLL inevitably exhibits nonlinearities in the loop. In particular, in the case of CP-PLLs, the PFD/CP block usually exhibits a nonlinearity that can be modelled as being memoryless[1]. That said, the input phase error interacts with the nonlinearity, leading to the generation of extra noise. In order to simplify the analysis of this phenomenon, we represent the nonlinear PFD/CP block as a cascade of a nonlinear block and a linear PFD/CP. Doing so, we denote by $\Delta\phi_{in}^{NL}[n]$ the input phase error after it has been distorted by the nonlinearity; this is shown in Fig. 2.5.

In terms of its spectral appearance, the nonlinearity-induced noise is typically manifest as an elevated noise floor and spurious tones [29]. Therefore, its analysis is facilitated by the study of the spectrum of $\Delta\phi_{in}^{NL}$, denoted $S_{\Delta\phi_{in}^{NL}}(f)$. For

---

[1] In general, a PFD/CP block exhibits both static and dynamic mismatches [26], [27]. However, previous work has shown that some typical dynamic mismatches can be approximated by a memoryless nonlinear function [28].

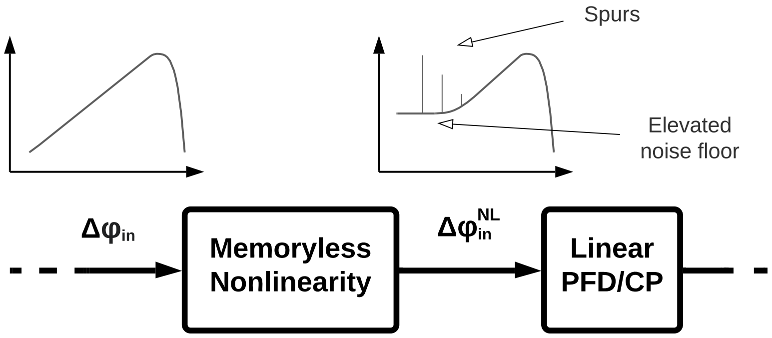

Figure 2.5: Close-in on the block diagram representation of the decomposition of a nonlinear PFD/CP inside the PLL.

calculation purposes, let us introduce the nonlinear function $\mathcal{N}(\cdot)$, and express $\Delta\phi_{in}^{NL}[n]$ as a function of $e_{acc}[n]$, namely:

$$\Delta\phi_{in}^{NL}[n] = \frac{2\pi}{N_{div}}\mathcal{N}\left(e_{acc}[n-1] + \tau_{os}\right), \tag{2.11}$$

where we define:

$$e_{acc}^{NL}[n] = \mathcal{N}\left(e_{acc}[n] + \tau_{os}\right). \tag{2.12}$$

It is worth noticing that τ_{os} is valued such that $E\left[e_{acc}^{NL}[n]\right] = 0$. This is forced by the locking condition of a type-II PLL [24]. Then, according to expressions (2.11) and (2.12), $\Delta\phi_{in}^{NL}[n]$ has zero mean if and only if $E[e_{acc}^{NL}[n]] = 0$. We denote the spectra of $\Delta\phi_{in}^{NL}$ and e_{acc}^{NL} by $S_{\Delta\phi_{in}^{NL}}$ and $S_{e_{acc}^{NL}}$, respectively.

That being said, from the linear model in Fig 2.4, while considering the decomposition in Fig 2.5 and the expressions in (2.10) and (2.11), we can draw a time domain-model for a fractional-N CP PLL with nonlinear PFD/CP block as shown in Fig. 2.6.

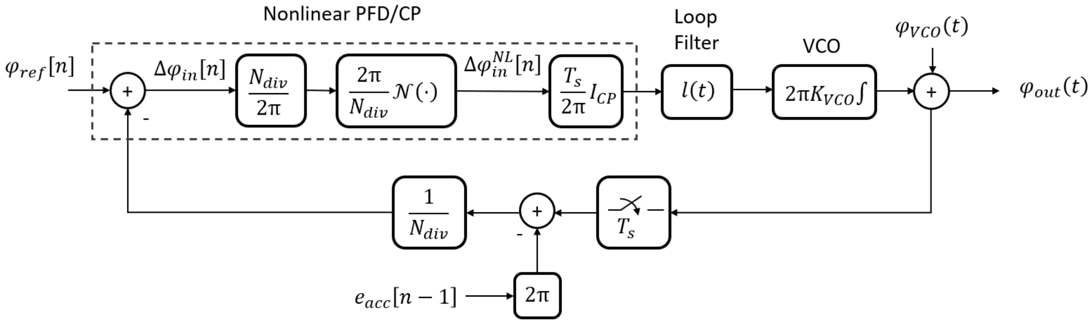

Figure 2.6: Time-domain model of a nonlinear fractional-N CP PLL inspired by [20, Fig. 6] and adjusted to the case of a nonlinear PFD/CP block.

2.3 Periodic Nonlinearity Noise

The considerations in the previous section showed that, even if we maximize the cycle length of the DDSM and get spur-free quantization noise, its accumulation e_{acc} will interact with nonidealities in the loop and give rise to spurious tones [30], [31]. In order to understand better the mechanism of spur generation, previous authors have thoroughly investigated the interaction between the quantization phase error and a nonlinearity. In particular, they focused on the evaluation of the periodic component of the nonlinearity-induced noise. In fact, it is the latter that leads to the generation of spurs. While doing that, they have presented a semi-analytical method to predict the locations and the amplitudes of the fractional spurs that are generated in a nonlinear fractional-N PLL [32].

In order to explain that result, we need to take a few steps back. From the expressions in (2.2) and (2.6), one can notice that the accumulated quantization error can also be expressed as:

$$e_{acc}[n] = \sum_{k=0}^{n} (y[k] - \alpha) = \sum_{k=0}^{n} y[k] - \sum_{k=0}^{n} \frac{X}{M}. \tag{2.13}$$

In (2.13), we can distinguish the difference of two sums. On the one hand we have the accumulation of the constant term $\alpha = \frac{X}{M}$ that produces a ramp. On the other hand, $y[k]$ can only assume integer values, and so does its accumulation. An example of the two sums is given in Fig. 2.7(a). Note that the graph of e_{acc} is a discrete set of points that lie on a set of continuous sawtooth tracks, as shown in Fig. 2.7(b). Let us denote by $\tau_k(t)$ the sawtooth tracks on which the samples

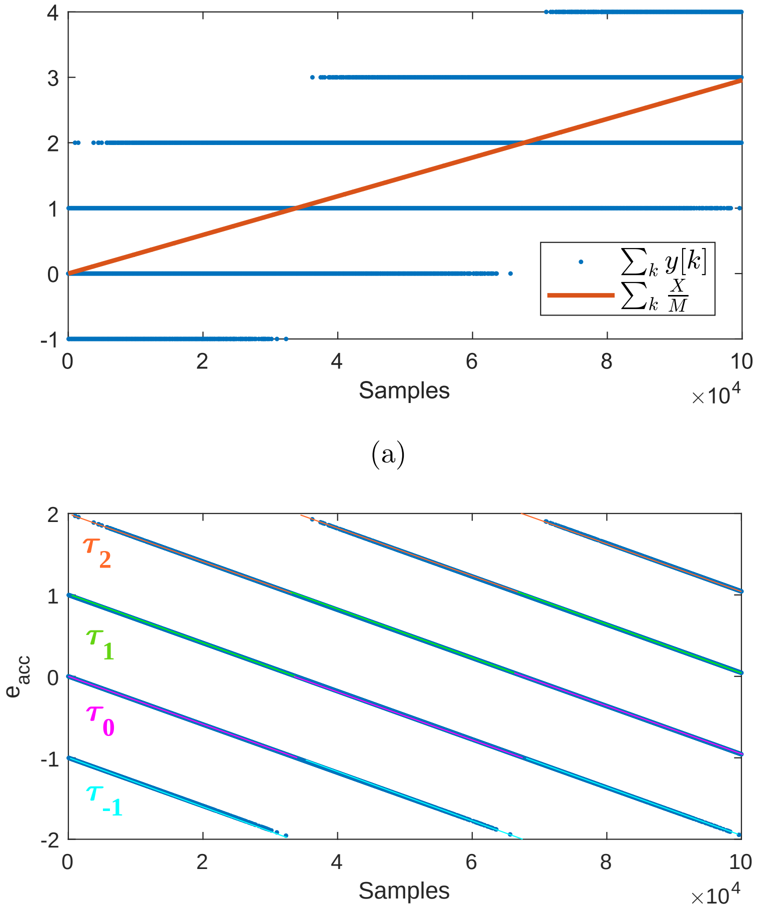

(a)

(b)

Figure 2.7: Time waveform of (a) the accumulated terms $\Sigma_k y[k]$ (blue), $\Sigma_k \frac{X}{M}$ (red) and (b) their difference e_{acc}, with the related tracks τ_k, in the case of a MASH 1-1-1 DDSM [32].

of e_{acc} lie, where $t \in \mathbb{R}$ and $k \in \mathbb{Z}$. Each track corresponds to a different value of the index k. That being said, for each sample $n \in \mathbb{N}$, $e_{acc}[n]$ assumes one of the values $\tau_k(t)|_{t=n}$, for any k. Moreover, the total number of tracks and their shapes depend on the input, type and order of the modulator.

The samples of the accumulated quantization error are not distributed over these tracks with uniform probability. The probability distribution, denoted $P(\cdot)$, depends on the architecture of the DDSM, its input X and initial state[2]. An example is shown in Fig. 2.8, where the modulator is a MASH 1-1-1 DDSM, $\alpha = 31/2^{20}$ and the initial state is odd. Knowing the analytical expressions of $\tau_k(t)$ and $P(\cdot)$ is fundamental for the analysis we will present later in the thesis.

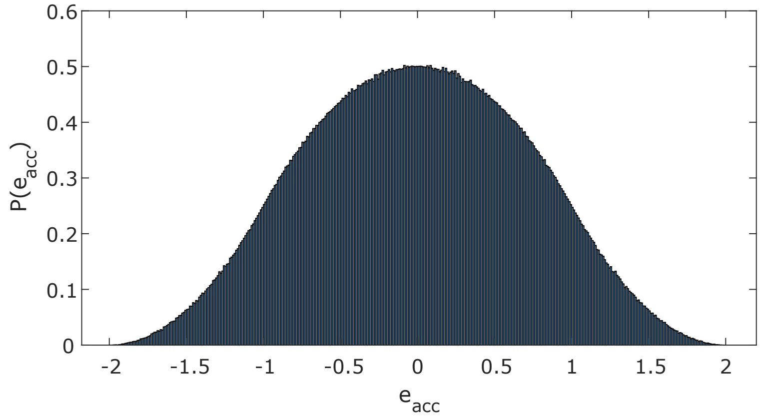

Figure 2.8: Simulated probability distribution of e_{acc} in the case of a MASH 1-1-1 DDSM.

From (2.10) one can deduce that the input phase error of the PFD is shaped similarly to e_{acc} but with a vertical offset of the sawtooth tracks. For this reason,

---

[2] For the sake of completeness, it is necessary to specify that since e_{acc} is a discrete variable, we should refer to its probability mass function (pmf). However we will usually refer to the probability distribution function $P(\cdot)$ which represents the pmf divided by the resolution of e_{acc}. This choice is made because, as the modulus of the DDSM increases, the resolution of e_{acc} gets smaller and, at the same time, e_{acc} tends to a continuous variable and $P(\cdot)$ tends to its probability density function (pdf). This concept will be resumed and used in Chapter 4.

we introduce a new set of tracks defined by:

$$\hat{\tau}_k(t) = \tau_k(t) + \tau_{os}, \tag{2.14}$$

In the presence of a nonlinearity $\mathcal{N}(\cdot)$, the accumulated quantization error is distorted in $e_{acc}^{NL}[n]$, as defined in (2.12). Note that the samples of $e_{acc}^{NL}[n]$, as well as $\Delta\phi_{in}^{NL}[n]$, do not lie on a set of straight sawtooth tracks any more. In fact, the tracks $\hat{\tau}_k$ are distorted by the nonlinearity, giving:

$$\hat{\tau}_k^{NL}(t) = N\left(\hat{\tau}_k(t)\right), \tag{2.15}$$

on which the samples of $e_{acc}^{NL}[n]$ lie. An example of $e_{acc}^{NL}[n]$ and the related distorted tracks $\hat{\tau}_k^{NL}(t)$ is shown in Fig. 2.9.

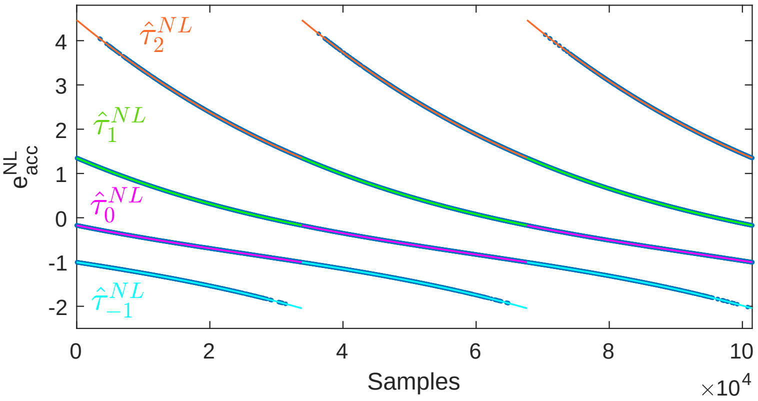

Figure 2.9: Time waveform of e_{acc}^{NL} with the related distorted tracks $\hat{\tau}_k^{NL}$ in the case of a MASH 1-1-1 DDSM and third-order nonlinearity $\mathcal{N}(x) = -0.23+0.99x+0.32x^2+0.15x^3$ [33].

The nonlinearity interacts with the accumulated quantization noise from the divider controller to produce additional phase noise in the loop. The nonlinearity-induced noise is typically composed of noise-like and periodic components. In a recent work by Donnelly and Kennedy [32], the authors have presented a method to predict the periodic component of the nonlinearity noise that allows one to obtain the locations and the amplitudes of the nonlinearity-induced fractional spurs. By definition, for each sample n, the distorted accumulated quantization error, $e_{acc}^{NL}[n]$, lies on one of the distorted tracks, assuming one of the values $\hat{\tau}_k^{NL}(t)|_{t=n}$ with probability $P\left(\tau_k(t)|_{t=n}\right)$. Therefore, the average value of $e_{acc}^{NL}[n]$, called the Periodic Nonlinearity Noise (PNN), is defined as [32]:

$$PNN[n] = \sum_k \hat{\tau}_k^{NL}(n) P(\tau_k(n)), \tag{2.16}$$

where the number of tracks indexed by k depends on the DDSM, and $n \in \mathbb{N}$[3]. It is worth noting that the value of τ_{os} is such so that the PNN has zero mean, which reflects the locking condition of the type II CP PLL. Fig. 2.10 shows an example of the PNN time waveform obtained using (2.16) from the distorted tracks presented in Fig. 2.9 and the probability distribution $P(\cdot)$ characterized like

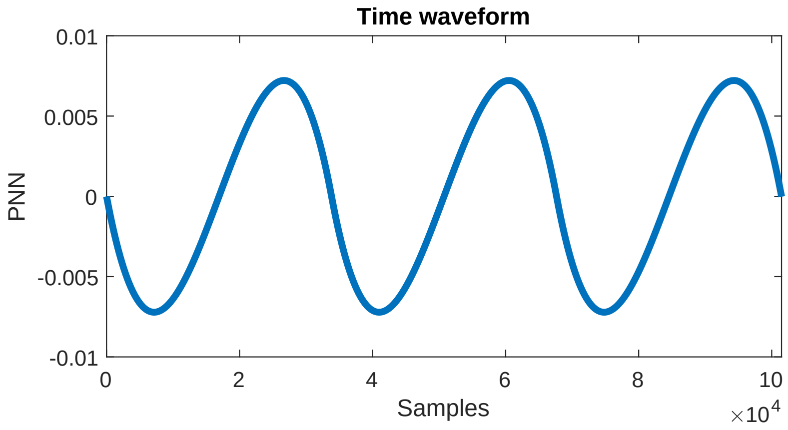

Figure 2.10: Time waveform of the PNN in the case of a MASH 1-1-1 DDSM and third-order nonlinearity $\mathcal{N}(x) = -0.23 + 0.99x + 0.32x^2 + 0.15x^3$ [33].

---

[3] Even though the tracks are defined as continuous signals, the accumulated quantization error and its distorted version are indexed by the samples n. As a consequence, the same is valid for the PNN. For this reason, in (2.16) we understand $\tau_k(n)$ and $\hat{\tau}_k^{NL}(n)$ to mean, respectively, $\tau_k(t)|_{t=n}$ and $\hat{\tau}_k^{NL}(t)|_{t=n}$.

the one shown in Fig. 2.8. More details about the expressions for $\tau_k(t)$ and $P(\cdot)$ will be given in the following. Using (2.16), it is possible to derive the noise terms associated with the spurious tones once one calculates analytical expressions for the tracks, the probability distribution of e_{acc}, and the nonlinearity [32].

It is also worth noting that the expression for the PNN holds in the presence of CP bleed current as long as the PFD/CP characteristic is properly adjusted and its contribution to τ_{os} is considered. Note that the resulting PNN always has a zero mean and, therefore, the case of no spurs will coincide with a PNN equal to zero. For the sake of simplicity we will not consider any bleed current or other offset that is intentionally added to the loop. This does not affect the validity of the analysis.

2.4 Simulation model

In the following chapters, we will present various studies on the analysis, prediction and mitigation of detrimental phenomena induced by nonlinearities in frequency synthesizers. This will be done with the support of simulation results. In particular, we have implemented a phase-domain model in MATLAB which describes a fractional-N type-II CP-PLL. The system is described with a time-based domain model as shown in Fig. 2.6 which is implemented with a recursive instantiation where each iteration represents a cycle around the loop. The information that travels around the loop is in terms of phase and the signals are sampled at the period of the reference frequency. What we describe is based on the analytical model developed by Perrott *et al.* [20]. The divider controller will be implemented by different DDSMs, as required. Furthermore, the PFD/CP is often modelled as a nonlinear block in order to show the consequences of nonlinearities in the system.

Apart from the modulation noise, other noise sources are present in a PLL, such as the VCO noise and the input referred noise. The latter typically represents the combination of the reference noise and physical divider, PFD and CP noise. All these components of noise contribute to the in-band phase noise of the synthesizer. These physical noise sources are considered zero in all the simulations performed. This does not represent what happens in a real circuit; however, it allows one to visualize better the effects of the interaction between the quantization noise and the nonlinearity, so-called "mathematical noise". On the other hand, instead, the VCO noise is assumed different from zero. However, for the sake of simplicity, the VCO is assumed to exhibit a phase noise profile with a constant roll-off of -20 dB/decade. Its magnitude at a 10 MHz offset is considered equal to -146 dBc/Hz. These and other parameters of the simulated loop are listed in Table 2.1. They will remain the same for all the following simulations. Details of other parameters of the simulated PLL, such as bandwidth or nonlinearity, are not given in Table 2.1, as they will change from case to case.

Table 2.1: Simulation model parameters

Parameter	Value
f_{ref}	122.88 MHz
I_{CP}	1.5 μA
Loop filter tansfer function order	3^{nd}
$S_{\Phi,VCO}(10MHz)$	-146 dBc/Hz
K_{VCO}	6 MHz/V
N_{int}	41
M	2^{20}

2.5 Summary

In this chapter we have discussed the generic structure of a fractional-N PLL and the modulation error associated to its operation. Some considerations and formulae are given for the evaluation of the periodic component of the nonlinearity-induced noise. Lastly, details are given on the simulation model of the PLL that is used in the following chapters for supporting the analyses that are presented in the thesis.

Chapter 3

Horn Spurs

In addition to the well-known reference spur and integer boundary spur, fractional-N frequency synthesizers exhibit sets of nonlinearity-induced subfractional spurs that appear in pairs. They have been called “horn spurs”. In this chapter, the behavior of the “horn spurs” is discussed and techniques for mitigating them are presented.

3.1 Introduction

“Horn spurs” have been observed in fractional-N frequency synthesizers based on a MASH 1-1-1 modulator. The distance between the spurs in each pair depends on the initial condition of the first EFM stage, $s_1[0]$. They are called “horn spurs” because the spurs always show up in pairs and with similar magnitudes [7]. An example of horn spurs measured on a commercial synthesizer is shown in Fig. 3.1,

As discussed in the previous Chapter, it is important to randomize the quantization error generated by the modulator in order to make its spectrum spur-free. This can be done by maximizing the cycle length that, in the case

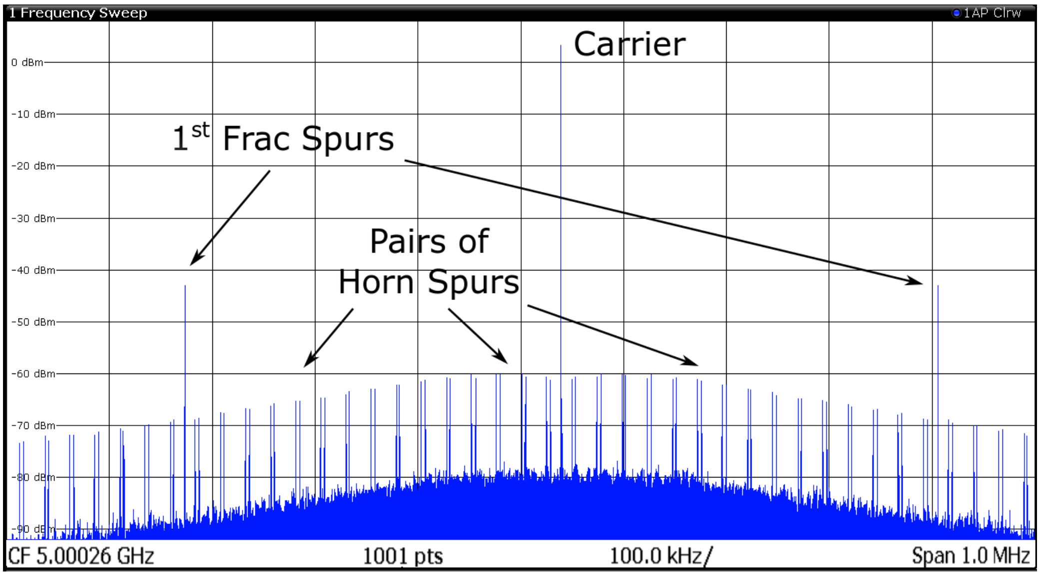

Figure 3.1: Spectrum measured at the output of the commercial wideband synthesizer ADF 4371 (Analog Devices) [34], that shows several pairs of "horn spurs".

of a MASH 1-1-1, is obtained by setting an odd initial condition in the first EFM stage [35]. Another way to increase the cycle length is to introduce a pseudorandom dither signal $d[n]$ in the modulator. In the case of a MASH 1-1-1, the dither is usually added to the input of the second stage, [25]. However, even if we do so, the modulation error retains some internal periodicities and, when the signal experiences nonlinear distortion, it leads to the phenomenon of horn spurs. To capture these spurs in simulation, a mismatch is considered between the UP and DOWN currents of the charge pump. In particular, we model an 8% CP current mismatch.

3.2 Horn Spurs Analysis

In order to understand the relation between the positions of the "horn spurs" and the parameters of the system, we express the input X of the DDSM in the following form:

$$X = \frac{a\,M}{b}, \tag{3.1}$$

where a and b are coprime. It has been noticed [7, 36] that this phenomenon repeats in frequency with period:

$$\Delta_f = \frac{f_{ref}}{b}, \tag{3.2}$$

and that it is periodic with respect to $s_1[0]$ with a period:

$$N_s = \frac{M}{b}. \tag{3.3}$$

In particular, it has been empirically noticed that the horn spurs are placed at

$$f_{hornspur} = \left(\frac{1}{2} + m\right)\Delta_f \pm f_h, \tag{3.4}$$

where $m \in \mathbb{N}$ and f_h is equal to

$$f_h = \frac{f_{PFD}}{M} \times \begin{cases} \big(s_1[0] + E(d[n])\big) \mod N_s & \text{if } (s_1[0] + E(d[n])) \mod N_s < \frac{N_s}{2} \\ \big(-s_1[0] - E(d[n])\big) \mod N_s & \text{if } (s_1[0] + E(d[n])) \mod N_s \geq \frac{N_s}{2} \end{cases} \tag{3.5}$$

Note that $E(d[n])$ represents the expected value of a dither signal applied to the second stage of our DDSM.

Fig. 3.2 shows the simulated output phase noise of this model when $X = 15 \times 256$, $M = 2^{20}$ and sweeping $s_1[0]$, the initial condition of the first stage of the DDSM, with $s_2[0] = s_3[0] = 0$.

Notice multiple sets of "horn spurs" that repeat in frequency every Δ_f, where $\Delta_f = \frac{122.88\times10^6}{2^{12}} \approx 30kHz$. The distance between the two spurs of each pair follows

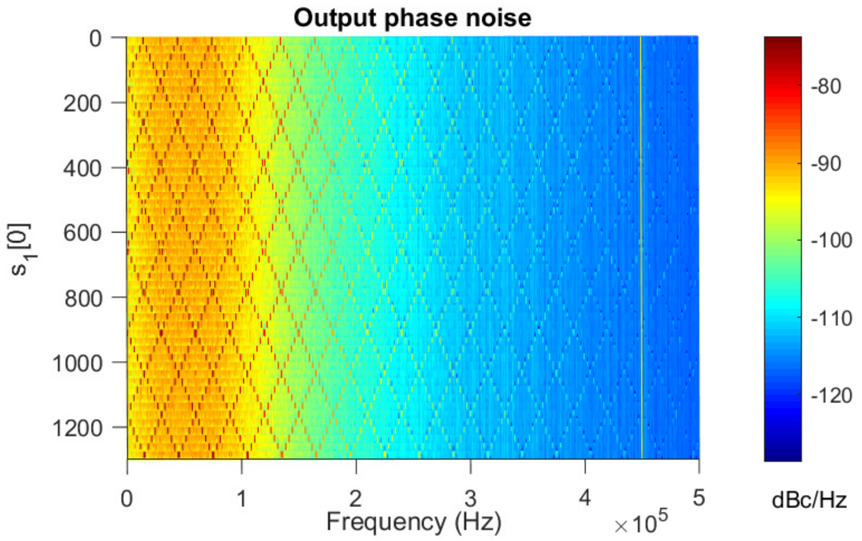

Figure 3.2: Simulated phase noise of the synthesizer, when $X = 3840 = 15 \times 256$, $M = 2^{20}$ and $s_1[0]$ is swept from 1 to 1300. There is a fixed fractional spur at 450 kHz and 15 pairs of horn spurs at lower frequencies.

(3.5). In fact, the spurs assume a different position in frequency for every value of $s_1[0]$, tracing out rhomboid shapes that repeat every N_s, as shown in Fig. 3.2. Therefore, changing the initial condition simply changes the *positions* of the spurs; it does not eliminate them. A particular case is shown in Fig. 3.3, where the initial condition is equal to 0 in the presence and absence of LSB dithering. Both result show horn spurs; however, in the undithered case of Fig. 3.3(a) the spurs of each pair perfectly overlap, as predicted by the formula in (3.5). As a consequence, more power of the noise gets concentrated at those single frequencies, leading to higher amplitude spurious tones. Moreover, because of the lack of randomization of the noise due to the absence of dithering, one may notice that the overall nonlinearity-induced noise manifests itself in a more spurious-like form. In particular, Fig. 3.3(a) shows more tones rather than in-band folded noise like the case of Fig. 3.3(b). For the sake of completeness, in the case of Fig. 3.3(b)

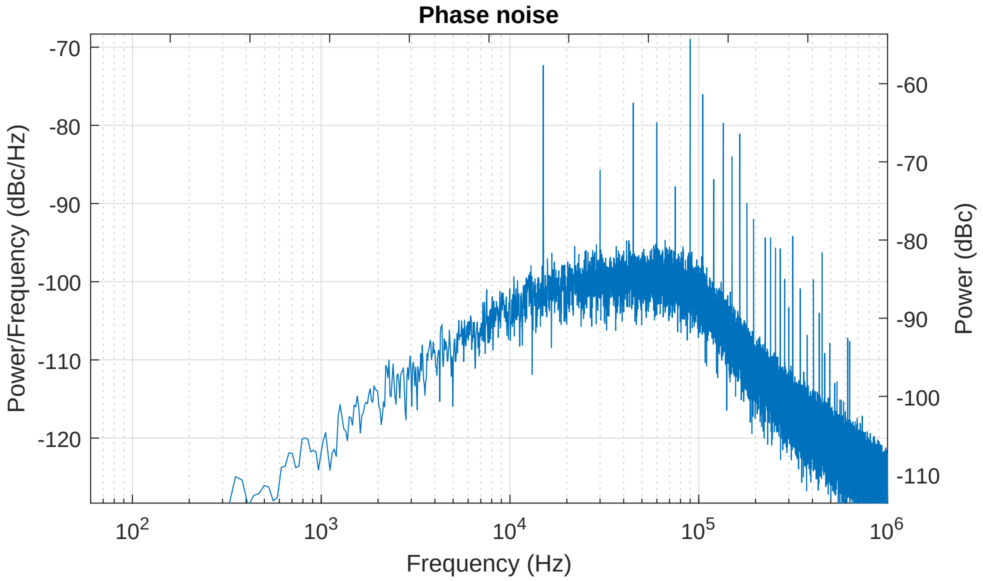

(a)

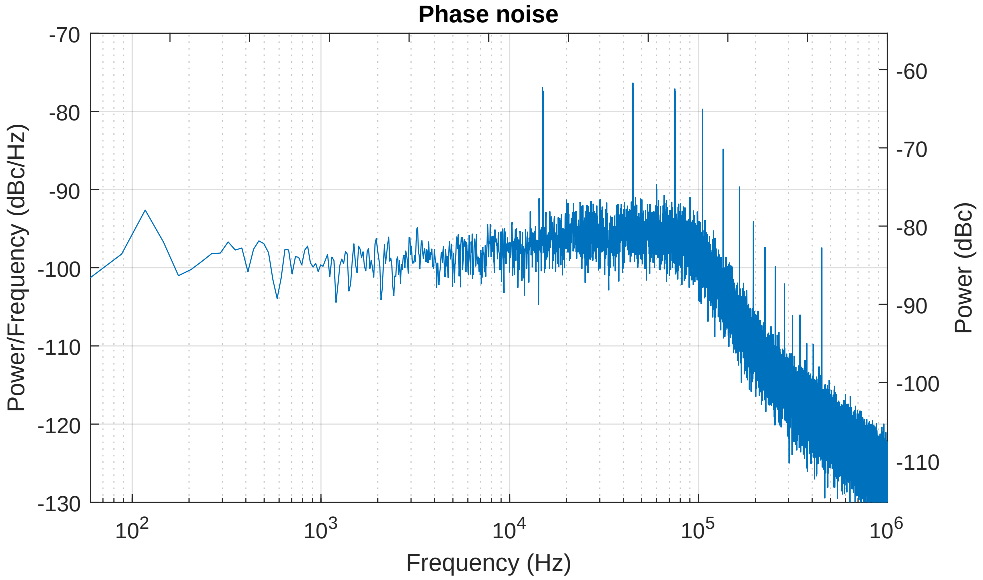

(b)

Figure 3.3: Simulated phase noise of the synthesizer, when $X = 3840 = 15 \times 256$, $s_1[0] = 0$ and (a) no dither, (b) LSB dither $d[n]$ applied to the second stage of the DDSM. There is a fixed fractional spur at 450 kHz and several horn spurs at lower frequencies. In the undithered case, the horn spurs overlap; in the dithered case, they are ≈ 117 Hz apart.

each pair of horn spurs almost but not exactly overlaps. In fact, according to equations (3.4) and (3.5), the spurs of each pair are $\approx$ 117 Hz apart.

Even though "horn spurs" are typically weaker than the fractional ones as in the example in Fig. 3.1, the former show up at subfractional frequencies. Consequently, they can be much closer to the carrier than the fractional ones. In particular, we know that the system may suffer from undesired inband spurs when it works at near integer-N conditions, that is when X is small or close to M [37]. One might attempt to avoid these fractional spurs by making $\frac{X}{M}f_{ref}$ larger than the bandwidth. Note, however, that the "horn spurs" are experienced every $\frac{f_{PFD}}{b}$, independently of the value of a in (3.1). Therefore, they can fall inside the bandwidth, even though $\frac{X}{M}$ itself is apparently sufficiently large, as is the case in Fig. 3.2.

In order to eliminate these spurs, we need to understand where they are coming from. We have already mentioned that it is common practice to maximize the cycle length of the DDSM. Despite this, throughout a cycle length of the DDSM there are sequences of values of $y[n]$ that are repeated, generating repetitive patterns in the quantization noise. When the accumulated quantization noise interacts with the nonidealities present in the loop, spurs are generated.

In the case of the "horn spurs", we can trace these patterns to the accumulation of the input of the *second stage* of the DDSM, $e_1[n]$. In fact, if we look at the quantization error of the second stage, $e_2[n]$, we can see patterns repeating with periods that relate to the frequencies of the first couple of spurs. These are shown in Fig. 3.4 for the cases of $s_1[0]$ equal to 13 and 29, respectively. From equations (3.2), (3.3), (3.4) and (3.5) one can derive the position of the first couple of spurs. Therefore, in the cases of Fig. 3.4 the first pairs are at 15 kHz ± 1582 Hz and 15 kHz ± 3457 Hz, respectively. The first two frequencies give periods of $60.31\mu s$ and $74.53\mu s$ that match the periods of the patterns in Fig. 3.4(a) of $59.79\mu s$ and

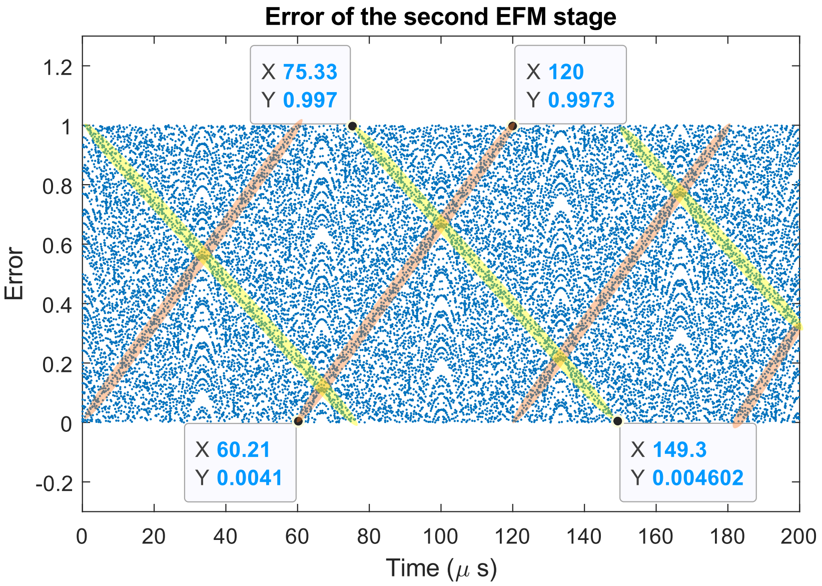

(a)

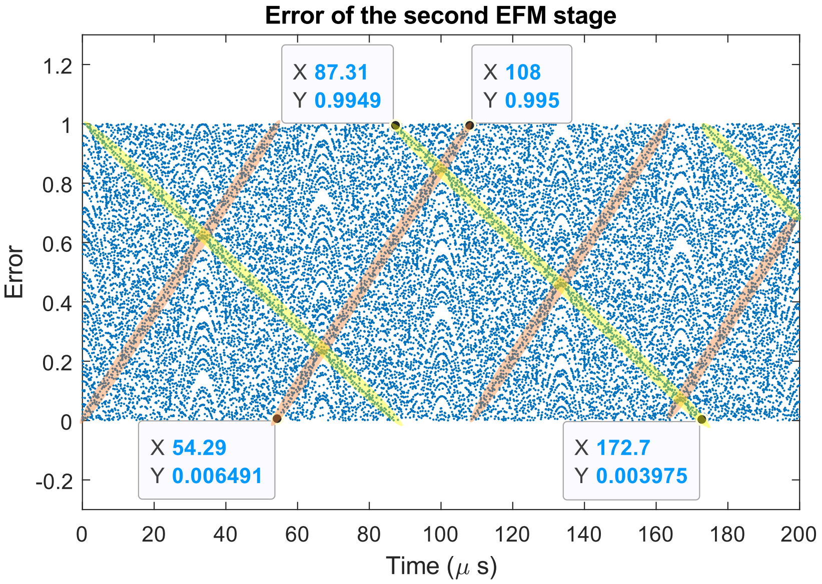

(b)

Figure 3.4: Simulated values of $s_2[n]$, when $X = 38406$ and, respectively, (a) $s_1[0] = 13$, (b) $s_1[0] = 29$. There are patterns, highlighted in the pictures, that repeat with a frequency of $\frac{\Delta_f}{2} \pm f_h$.

$73.97\mu s$. For the case of Fig. 3.4(b) we are expecting periods of $54.47\mu s$ and $89.63\mu s$; in simulation we obtain $53.71\mu s$ and $85.39\mu s$, confirming our empirical prediction.

We claim that the phenomenon of the "horn spurs" is generated in the second stage EFM and that it is strictly related to its input $e_1[n]$. In fact, if we take into account the period of $e_1[n]$ [35]:

$$L_{s1} = \left(\frac{M}{GCD(M, X)} \right), \tag{3.6}$$

and replace X with its expression from (3.1), we obtain the term b, on which Δ_f and N_s depend.

3.3 Mitigation Techniques

From the considerations above, we propose a few techniques to mitigate the phenomenon of "horn spurs". For all the following examples we are considering the case of $X = 3840$ and $s_1[0] = 13$, that gives unpleasant inband horn spurs, as shown by simulation in Fig. 3.5. The expected fractional spur is at $\frac{X}{M} f_{ref} =$ 450 kHz, which is outside the loop bandwidth in our example.

3.3.1 LSB extension

The most intuitive solution is to increase L_{s1}, which is maximized when X is odd [35]. This can be obtained by increasing the number of bits of the modulator, denoted by n_0, to $n_0 + 1$ and setting the least significant bit (LSB) of X to 1. This way, independently of the choice we make for the other n_0 most significant bits (MSBs), the resulting value of X is odd. This is an easy solution but introduces, as a drawback, an error of $\frac{1}{2^{n_0+1}} f_{ref}$ in the output frequency. Fig. 3.6 confirms that this technique eliminates the horn spurs but also changes the synthesized

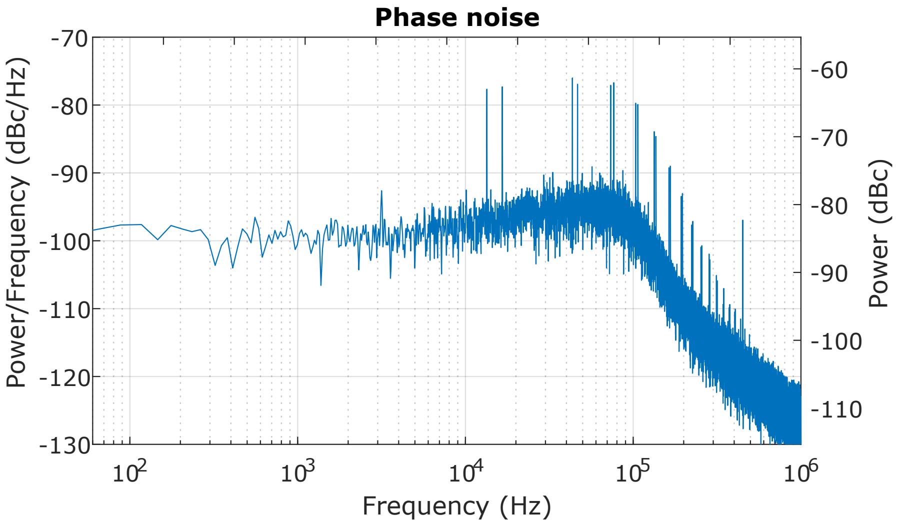

Figure 3.5: Simulated phase noise, when $X = 3840 = 15 \cdot 256$, $s_1[0] = 13$, and respectively LSB dither on the second EFM stage

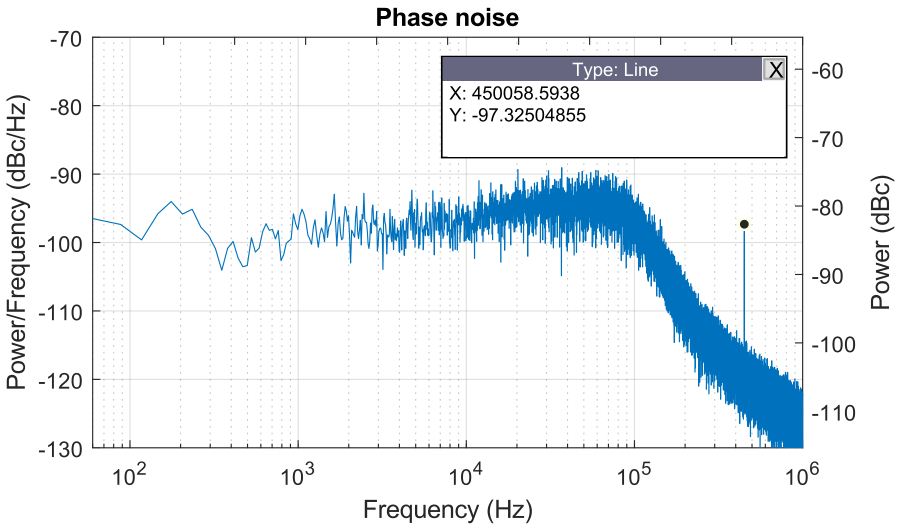

Figure 3.6: Simulated phase noise, when $X = 3840 = 15 \times 256$, $s_1[0] = 13$, and LSB extension on the input word.

frequency. This can be deduced from the offset in the position of the fractional spur.

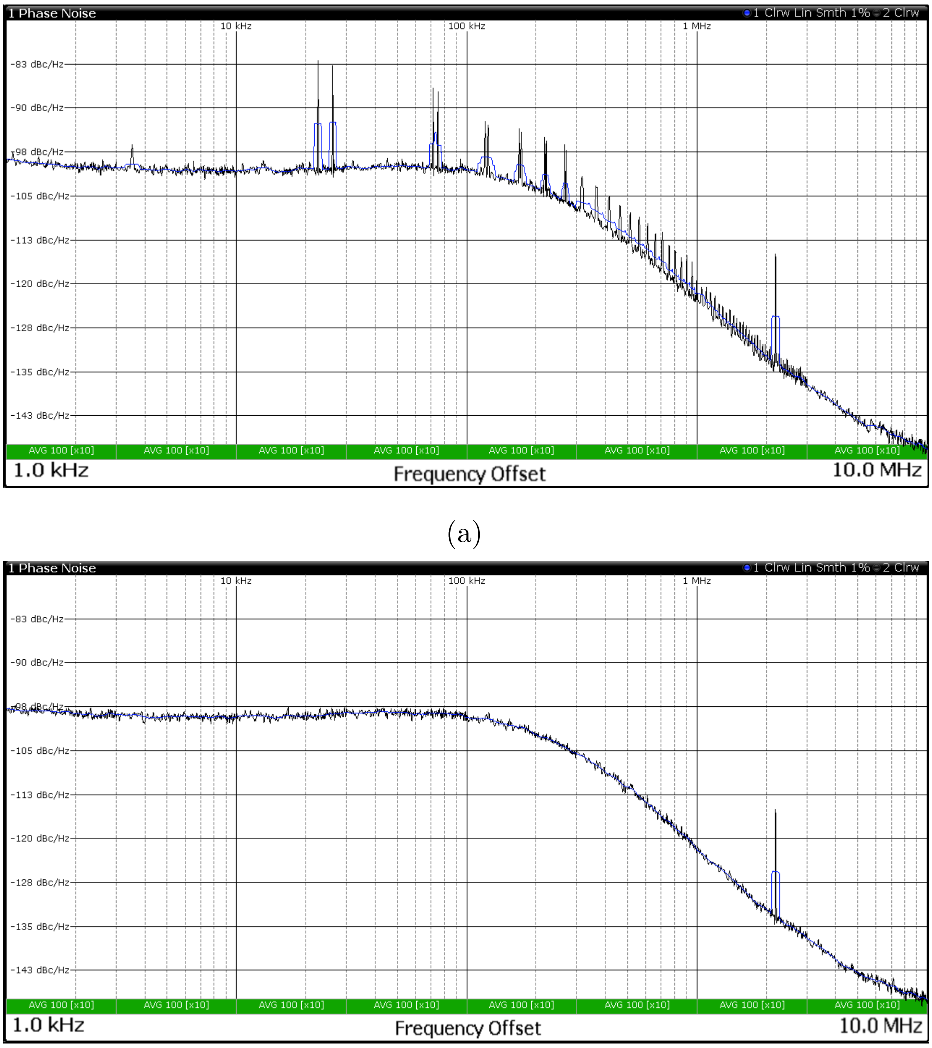

(a)

(b)

Figure 3.7: Phase noise measured on the ADF4371 with $f_{ref} = 100MHz$, when $s_1[0] = 300$, $X = 737280 = 45 \times 2^{14}$ and the LSB is set to (a) 0 and (b) 1. “Horn spurs” are visible in (a) but missing in (b).

This method has been tested on a commercial synthesizer, the Analog Devices' ADF4371, that comes with a primary modulator that is a programmable 26 bit MASH 1-1-1, where the 25 MSBs are used to set the value of the desired output frequency [34]. The LSB, which is set to 0 by default, can be programmed to be 1 to implement LSB extension. Figs. 3.7(a) and 3.7(b) show, respectively, the cases where the extended LSB is set to 0 and 1. In the case of an odd input, there are no "horn spurs" but there is a slight offset in the center frequency at the LSB level.

3.3.2 Unfiltered dither

An alternative to LSB extension is to break the periodicity of $e_1[n]$ by means of dithering. To do so, it is not sufficient to use dither on the second EFM stage. To eliminate "horn spurs" we must also add dithering to the *first* EFM stage. This signal should ideally be generated with zero average to avoid an offset, i.e. $d[n] = U(-1, 1)$.

It is important to specify that every time we apply dither we are adding a source of noise into the system. In particular, introducing unfiltered dither into the first EFM stage has the drawback that the accumulated noise will have a PSD with a -20 dB/dec slope. For $f \ll f_{ref}$ we can evaluate the output phase noise contribution of the dither as:

$$S_{\Phi,unfilt,dither} = \frac{f_{ref}}{f^2} \cdot \sigma^2 \cdot |G(f)|^2, \tag{3.7}$$

where, in the case of uniformly distributed dither $U(i, j)$, the variance is $\sigma^2 = \frac{(j-i+1)^2-1}{12 \cdot M^2}$, and $G(f) = \frac{A(f)}{1+A(f)}$, where $A(f)$ is the open-loop transfer function of the PLL [20]. Hence, when the modulus of the DDSM is not large enough, the phase noise contribution of the dither is dominant at low frequencies, as shown in Fig. 3.8.

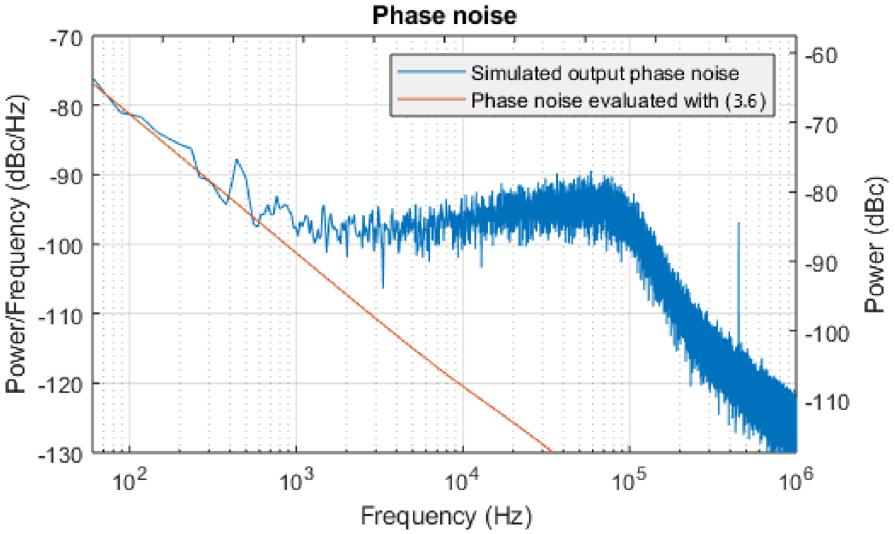

Figure 3.8: Simulated phase noise, when $X = 3840 = 15 \times 256$, $s_1[0] = 13$, and $U(-1, 1)$ dither on the first EFM stage.

One might think of avoiding this issue by filtering the dither with a simple $(1 - z^{-1})$ function. Unfortunately, the filtered signal would be accumulated by the first EFM stage and its effect would be similar to applying unfiltered dither directly to the second EFM stage. As we have already noted, that is not sufficient to mitigate the “horn spurs”. Other types of filtering can be investigated with the drawback of higher implementation complexity. In real applications, the phase noise expressed in (3.7) will typically be masked by the phase noise of the reference if M is sufficiently large.

3.3.3 HK-MASH 1-1-1

Thirdly, it is also possible to modify the architecture of the modulator itself, for example to use an HK-MASH 1-1-1 instead of a conventional MASH 1-1-1. The structure and the operation of this type of DDSM are extensively described in [35] and [38]. Every n_0-bit wide EFM stage, shown in Fig. 3.9, is designed such that

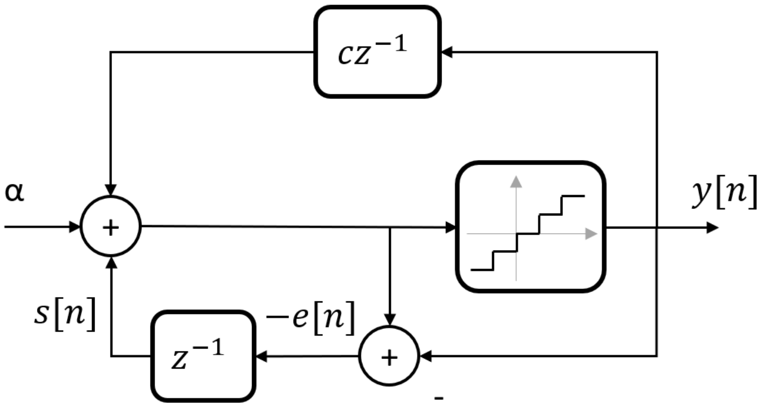

Figure 3.9: Block diagram of a modified first order EFM, comprising an HK-MASH 1-1-1 [35].

the equivalent modulus is a prime number close to 2^{n_0}. This is denoted M_p and it is expressed as $(2^{n_0} - c)$.

In the case of $n_0 = 20$, the first prime number smaller than 2^{n_0} is $(2^{20} - 3)$. The cycle length L_{s1} is maximized independently of the value of X, following (3.6).

Fig. 3.10 shows the simulated phase noise when we use an HK-MASH 1-1-1. As in the case of LSB extension, the synthesized output frequency differs slightly from the desired one. However, we get a relatively insignificant error of $\left(\frac{X}{M_p} - \frac{X}{M}\right) f_{PFD}$ that is just 1.2875 Hz in this example.

Here, the size of the error depends on both the desired frequency $\frac{X}{M} f_{PFD}$ and the value of the modulus. Therefore, the worst case error would be equal to $\frac{1}{2M_p} f_{PFD}$, i.e. half a frequency step of the HK-MASH, as with LSB extension. The downside of this approach is the slightly more complex structure of the modulator.

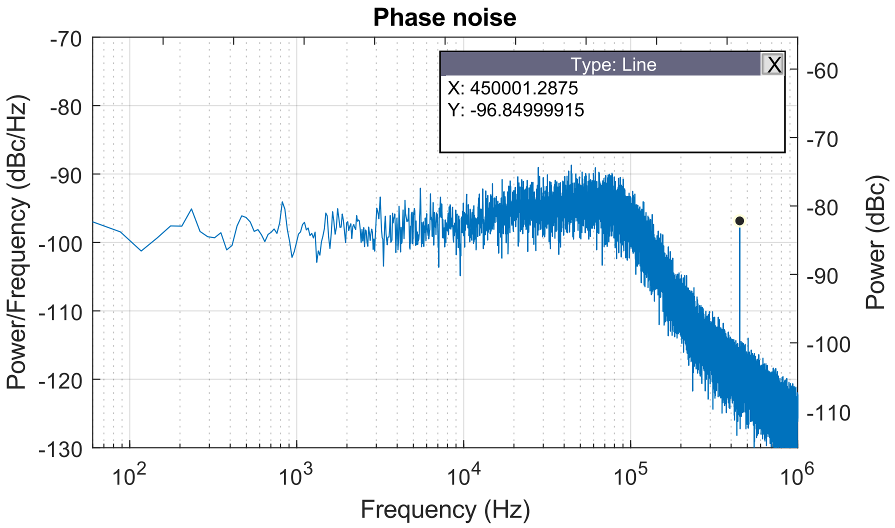

Figure 3.10: Simulated phase noise, when $X = 3840 = 15 \cdot 256$, $s_1[0] = 13$, and the modulator is an HK-MASH 1-1-1, with equivalent modulus $M_p = 2^{20} - 3$.

3.3.4 Comparison of techniques

All three techniques have been shown, by simulation, to mitigate the horn spurs. Each one operates in a slightly different way, with different results and drawbacks. In particular, the use of DC-free zeroth order dither allows one to synthesize the output frequency with no error, but introduces higher noise at low frequencies. This does not happen with the other two techniques but they introduce a frequency error in the output signal. The size of the error depends on the technique and the number of bits of the modulator.

The cost of hardware also depends on those aspects. We can compare the hardware implementation of the techniques presented in Sec. 3.3.1 and Sec. 3.3.3 in the case of similar frequency error. With the approximation of neglecting c compared to 2^{n_0}, the maximum frequency error of an n_0-bit HK-MASH 1-1-1 is equal to that of an $(n_0 + 1)$-bit MASH 1-1-1 with its LSB fixed to 1.

That said, for values of n_0 such that c is equal to 1, an n_0-bit HK-MASH 1-1-1 uses approximately the same amount of hardware as a regular $(n_0 + 1)$-bit MASH 1-1-1 [35]. For cases where c is greater than 1, the HK-MASH implementation requires approximately 10% extra area and power.

3.4 Summary

In this chapter, we have analyzed and characterized the phenomenon of the horn spurs in a fractional-N CP-PLL-based frequency synthesizer with a MASH 1-1-1 DDSM. We have presented three techniques that allow one to mitigate the horn spurs with negligible downside. Their successful functioning has been confirmed by simulation and one of the mitigation techniques has also been validated on a commercial synthesizer.

Chapter 4

Spur Immunity in MASH-based Fractional-N Frequency Synthesizers

Even if horn spurs are successfully mitigated, a nonlinear fractional-N frequency synthesizer still suffers from fractional spurs. In this chapter, we will present and discuss the performance of MASH-based fractional-N PLLs in terms of fractional spurs when the system is affected by polynomial nonlinearities.

4.1 Introduction

Significant efforts have been made to improve the spur performance of fractional-N synthesizers [39]—[44]. Some techniques aim to linearize the system while others try to compensate for or avoid the effects of the nonlinearity. Most of these techniques attenuate but do not eliminate the spurs completely because a residual nonlinearity is inevitably present. Excellent worst case in-band fractional spur performance has been realized using Successive Requantizers (SR) [45] and

Probability Modulator Redistributors (PMR) [46] which exploit the statistical properties of the DDSM signal. SR modulators are theoretically capable of providing spur-free operation in the case of polynomial nonlinearities up to a certain order, which can be selected with the compromise of higher quantization noise [43]. However, the SR implementation incurs a higher hardware cost compared to other DDSM architectures.

In this Chapter we discuss the effect of polynomial nonlinearities on traditional MASH-based fractional-N PLLs. In particular, we analyze the connection between the modulator, the nonlinearity, and the resulting spurious behavior. We prove immunity from spurs for certain combinations of modulator and polynomial nonlinearity and illustrate the results by simulation.

4.2 MASH DDSMs

As mentioned in Chapter 2, the DDSM plays a key role in the operation of a fractional-N frequency synthesizer, causing fractional division via modulation of the division ratio. In addition to that, the DDSM has the task of properly randomizing and high-pass filtering the quantization noise that it generates. In this Chapter we consider one of the most commonly used DDSM architectures, namely the multi-stage noise shaping (MASH) structure [47]—[50]. It has been introduced in Section 2.2, and the example of a MASH 1-1-1 was shown in Fig. 2.2. Generally, a MASH DDSM is composed of a series of error feedback modulators (EFM). For the sake of simplicity, we consider the cases where only first-order EFMs (EFM1) are used, as shown in Fig. 4.1(a). The number of EFM1 stages in series determines the order of the modulator. As depicted in Fig. 4.1(b), each i^{th} EFM1 is composed of a delay block and a 1-bit quantizer which introduces a quantization error $e_i[n]$.

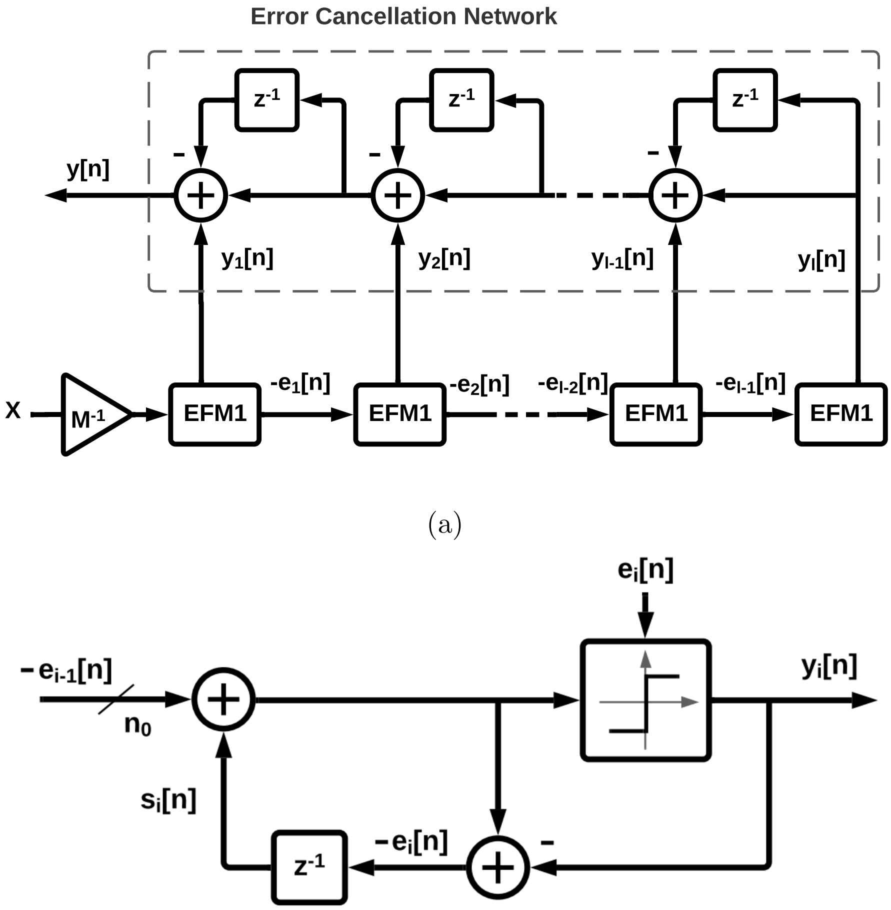

(a)

(b)

Figure 4.1: Block diagram of (a) a l-order MASH DDSM and (b) the i^{th} first-order error feedback modulator (EFM1), with $i \in [2, l]$.

An l^{th} order MASH DDSM generates an output $y[n]$ that is expressed in the frequency domain as:

$$Y(z) = \frac{X}{M} + E_l(z) \cdot \left(1 - z^{-1}\right)^l, \tag{4.1}$$

where $E_l(z)$ is the Z-transform of the error $e_l[n]$ of the l^{th} EFM1 stage. In (4.1), the term $E_l(z)\left(1 - z^{-1}\right)^l$ represents the quantization error generated by an l^{th} order MASH DDSM. Its accumulation $E_{acc}(z)$ is then equal to:

$$E_{acc}(z) = E_l(z) \cdot \left(1 - z^{-1}\right)^{l-1}, \tag{4.2}$$

and its expression in the time domain is:

$$e_{acc}[n] = \sum_{k=0}^{l-1} (-1)^k \binom{l-1}{k} e_l[n-k]. \tag{4.3}$$

Since every EFM1 has a 1-bit quantizer, each error $e_i[n]$ has a range of $(-1, 0]$. That being so, and considering the expression in (4.3), one can demonstrate that the full range of $e_{acc}[n]$ is equal to $\left(-2^{l-2}, 2^{l-2}\right)$ in the case of an lth-order MASH DDSM.

In order to perform our analysis on the spurious behavior of MASH-based fractional-N PLLs we evaluate the PNN. However, as discussed in Section 2.3, we need to derive the expressions for the tracks and the probability distribution of e_{acc} in order to calculate the PNN. In Section 2.3 we defined the tracks $\tau_k(t)$ as the set of line segments on which the samples of $e_{acc}[n]$ lie. Therefore, $\tau_k(t)$ has values in $\left(-2^{l-2}, 2^{l-2}\right)$. Moreover, in the case of a *near-to-integer condition*[1], i.e. $X \ll M$ or $(M - X) \ll M$, one can empirically notice that the total number of tracks is 2^{l-1} and that they repeat with period $\frac{M}{X}$. From these considerations we

---

[1] The near-to-integer condition represents the case we are most interested in, since the primary spurs, located at $\frac{X}{M} f_{ref}$ and $\frac{M-X}{M} f_{ref}$ [37], are more likely to appear inside the bandwidth where they are not attenuated by the loop filter.

can express the tracks as:

$$\tau_k(t) = k - \left(\frac{t \cdot X}{M} \mod 1 \right), \tag{4.4}$$

where k goes from $\left(-2^{l-2}+1\right)$ to $+2^{l-2}$. This is confirmed in Fig. 4.2 that shows the simulated time waveform of e_{acc} in the cases of second, third and fourth-order MASH modulators in the near-to-integer condition. In this example, the input

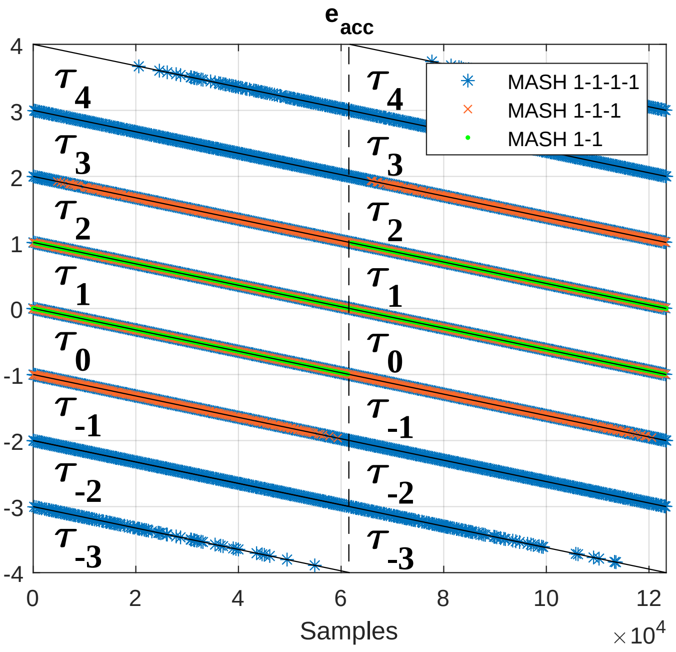

Figure 4.2: Time waveform of e_{acc}, in the cases of a second, third and fourth-order MASH DDSMs with $X = 17$ and $M = 2^{20}$.

and the modulus of all three DDSMs are respectively 17 and 2^{20}, returning a period $\frac{M}{X}$ for e_{acc} approximately equal to 61680. These values for X and M are used hereinafter. The fact that X and M are coprime maximizes the cycle length in the DDSM [35]. If (but not limited to) it is not possible to choose a coprime value of X, LSB dithering can also be used for this purpose [25]. Either one of these two methods allows one to disrupt the cycles of the modulator, by randomizing its quantization error and, therefore, mitigating idle tones in the PSD of e_{acc}. As a consequence, the randomization of e_{acc} provides a probability distribution function that can be approximated by the continuous expressions for $P(\cdot)$, as listed in the following[2].

The pseudo-analytical expression for the probability distribution of e_{acc} is harder to find and it changes according to the order of the modulator. The expressions for $P(\cdot)$ have been derived pseudo-analytically with the method presented in Appendix A. In particular, for the case of a MASH 1-1, the probability distribution function is:

$$P(x) = \begin{cases} 1+x & \text{if } -1 \leq x \leq 0 \\ 1-x & \text{if } \quad 0 \leq x \leq 1 \end{cases} \tag{4.5}$$

In the case of MASH 1-1-1, $P(\cdot)$ can be expressed as:

$$P(x) = \begin{cases} \frac{1}{4}(x+2)^2 & \text{if } -2 \leq x \leq -1 \\ \frac{1}{2} - \frac{1}{4}x^2 & \text{if } -1 \leq x \leq 1 \\ \frac{1}{4}(x-2)^2 & \text{if } \quad 1 \leq x \leq 2 \end{cases} \tag{4.6}$$

---

[2] We would like to remark that the assumption of expressing the probability distribution of e_{acc} as a continuous function is only an approximation as it represents the case where the modulus of the DDSM tends to infinity. However, since the modulus is typically large and the quantization error is reasonably randomized, the aforementioned assumption is qualitatively acceptable in practical applications.

whereas, for a MASH 1-1-1-1 the function $P(\cdot)$ is:

$$P(x) = \begin{cases} \frac{1}{54}(x+4)^3 & \text{if } -4 \le x \le -3 \\ \frac{x}{9} - \frac{1}{54}(x+2)^3 + \frac{1}{3} & \text{if } -3 \le x \le -2 \\ \frac{x}{9} + \frac{1}{3} & \text{if } -2 \le x \le -1 \\ \frac{x}{9} - \frac{1}{27}(x+1)^3 + \frac{1}{3} & \text{if } -1 \le x \le 0 \\ -\frac{x}{9} + \frac{1}{27}(x-1)^3 + \frac{1}{3} & \text{if } \quad 0 \le x \le 1 \\ -\frac{x}{9} + \frac{1}{3} & \text{if } \quad 1 \le x \le 2 \\ -\frac{x}{9} + \frac{1}{54}(x-2)^3 + \frac{1}{3} & \text{if } \quad 2 \le x \le 3 \\ -\frac{1}{54}(x-4)^3 & \text{if } \quad 3 \le x \le 4 \end{cases} \tag{4.7}$$

Fig. 4.3 shows the probability distributions of e_{acc} for the three cases considered. These have been produced by histogramming the samples of e_{acc} for sufficiently long sequences of samples (four times M). The functions in (4.5), (4.6) and (4.7) are plotted as red curves, respectively in Figs 4.3(a), 4.3(b) and 4.3(c), showing a good match with the histograms of the simulated signals.

4.3 Analysis and Simulations

A real frequency synthesizer inevitably has nonlinearities in the system. We have already mentioned that, in the case of CP-PLLs, the PFD/CP block typically exhibits a nonlinearity that can be considered memoryless [28]. The shape of the PFD/CP nonlinear function, $\mathcal{N}(\cdot)$, determines the PNN. As a consequence, the function $\mathcal{N}(\cdot)$ determines the magnitude and pattern of the fractional spurs. What matters is the shape of $\mathcal{N}(\cdot)$ over the range of values that its input assumes. In other words, we are only interested in the nonlinearity encountered over the range of $\hat{\tau}_k$, as evidenced by (2.16).

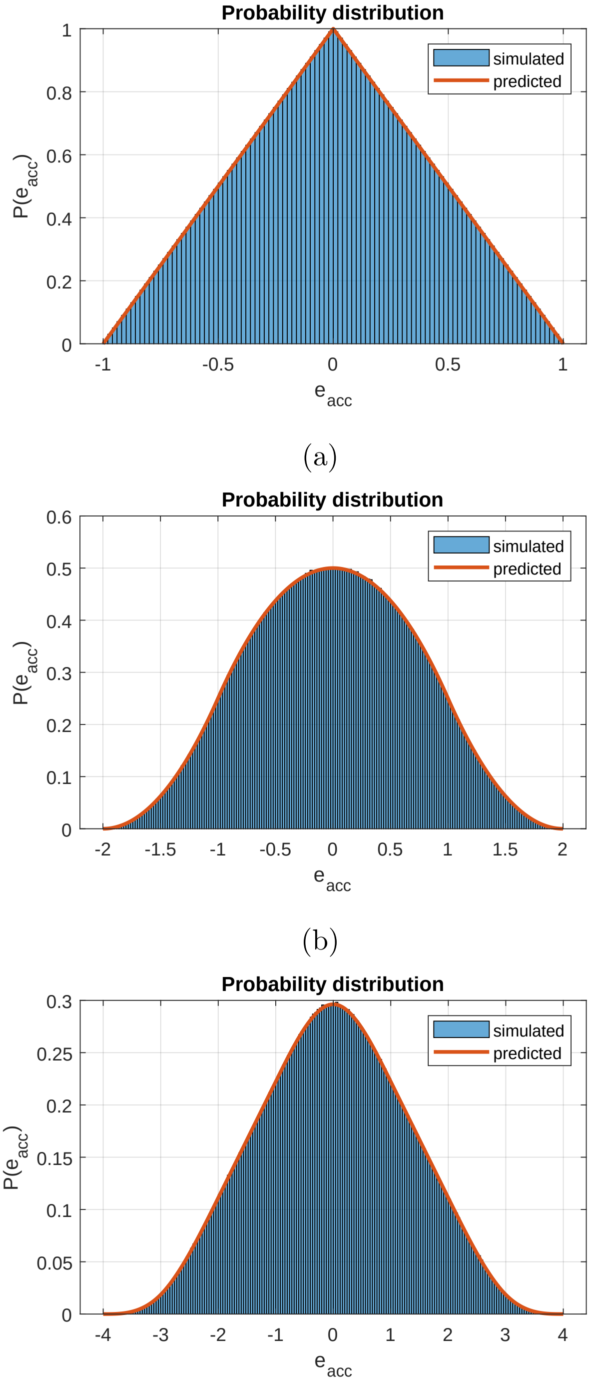

(a)

(b)

(c)

Figure 4.3: Probability distribution of e_{acc}, in the case of (a) MASH 1-1, (b) MASH 1-1-1 and (c) MASH 1-1-1-1 DDSMs with $X = 17$ and $M = 2^{20}$.

In general, the nonlinearity $\mathcal{N}(\cdot)$ can exhibit a variety of shapes. However, we are interested in what happens over the limited range of inputs defined by e_{acc}. Let us assume that this function can be expressed locally as a power series centred at zero [42], [43], [51]. In the hypothesis of no CP bleed current, the zeroth-order term is equal to zero. Let us assume, without loss of generality, that the coefficient of the first-order term is equal to unity. In Appendix B, it is shown that these assumptions do not undermine the generality of the analysis. Doing so, the expression for the nonlinear function becomes:

$$\mathcal{N}(x) = x + a_2x^2 + a_3x^3 + a_4x^4... \tag{4.8}$$

It is true that nonlinearities are inevitable but they are also undesirable. A lot of design effort is normally made to minimize the nonlinear terms of $\mathcal{N}(\cdot)$. Therefore, we would expect the coefficients of the nonlinear terms to be much smaller than unity.

In this chapter we consider cases where the nonlinearity is a polynomial up to third-order. In particular, in this section we analyze the cases of quadratic, cubic and generic third-order polynomial nonlinearities in MASH-based CP-PLLs [42], [43].

The analysis is accompanied by simulations of the PLL that support our analytical results.

4.3.1 Quadratic Nonlinearity

First, we analyze the case of a quadratic nonlinearity. This means that the nonlinear function represented in (7.10) has all coefficients except a_2 equal to zero.

$$\mathcal{N}(x) = x + a_2x^2 \tag{4.9}$$

We can calculate the periodic term of the noise introduced by a quadratic nonlinearity exactly by substituting (4.4) and (2.14) into (2.16), to obtain

$$PNN[n] = \sum_k \left(k - \left(\frac{n \cdot X}{M} \bmod 1 \right) + \tau_{os} + a_2 \left(k - \left(\frac{n \cdot X}{M} \bmod 1 \right) + \tau_{os} \right)^2 \right) P \left(k - \left(\frac{n \cdot X}{M} \bmod 1 \right) \right) \quad (4.10)$$

In order to simplify the expression for the PNN, we define the following function of n:

$$w[n] = - \left(\frac{n \cdot X}{M} \bmod 1 \right), \quad (4.11)$$

that describes a sawtooth trace lying between -1 and 0.

To evaluate the PNN, we need to provide an expression for the probability distribution $P(\cdot)$. This function depends on the modulator. Therefore, we analyze separately the cases for the different MASH DDSMs.

MASH 1-1

In Sec. 4.2 we showed that a MASH 1-1 produces only two tracks, corresponding to k equal to 0 and 1. Therefore, the summation in (4.10) reduces to the sum of two terms. Applying the simplification (4.11), the sum becomes:

$$\begin{aligned} PNN[n] &= \left(w[n] + \tau_{os} + a_2 \left(w[n] + \tau_{os} \right)^2 \right) \cdot P(w[n]) + \\ &+ \left(1 + w[n] + \tau_{os} + a_2 \left(1 + w[n] + \tau_{os} \right)^2 \right) \cdot P(1 + w[n]) \end{aligned} \quad (4.12)$$

From the definition of $w[n]$, the arguments of $P(w[n])$ and $P(1 + w[n])$ have ranges that are equal to $(-1, 0]$ and $(0, 1]$. Therefore, substituting the expression for the probability distribution (4.5) into (4.12), we obtain that $P(w[n])$ and $P(1 + w[n])$ are respectively equal to $(1 + w[n])$ and $(-w[n])$.

Carrying out the calculations, the final expression for the PNN becomes:

$$PNN[n] = a_2 \tau_{os}^2 + \tau_{os} - a_2 w[n](w[n] + 1), \quad (4.13)$$

that is indeed a function of n. The result suggests that a quadratic nonlinearity generates spurs in a CP-PLL with a MASH 1-1 modulator; this is confirmed by simulation. An example is given in Fig. 4.4 that shows the simulated output phase noise when $a_2 = 0.02$.

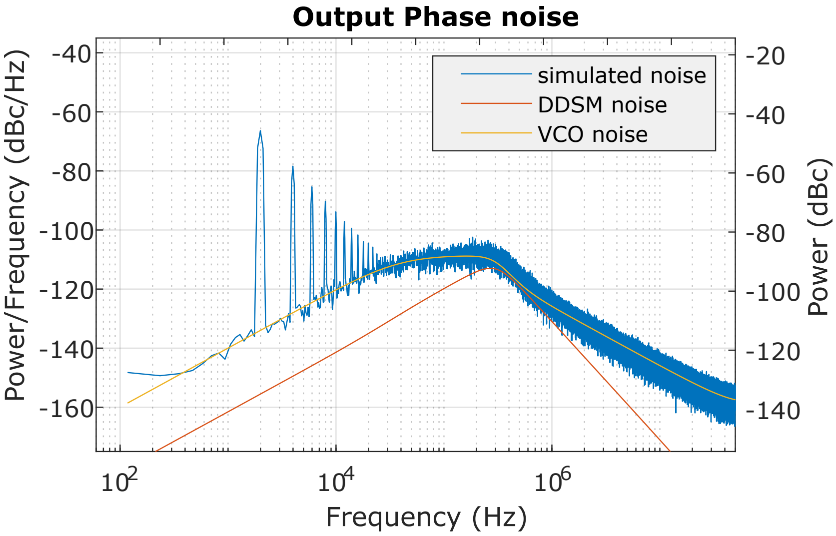

Figure 4.4: Simulated output phase noise in the case of a MASH 1-1 DDSM and quadratic nonlinearity with $a_2 = 0.02$.

It is worth noticing that, by definition, τ_{os} assumes a value such that the expression in (4.13) has zero mean. This leads to:

$$\tau_{os} = \frac{-1 + \sqrt{1 - \frac{2}{3}a_2^2}}{2a_2} \tag{4.14}$$

In Appendix C we discuss in detail how the solution of τ_{os} was obtained in this and subsequent cases.

MASH 1-1-1

In the case of a MASH 1-1-1, the number of tracks is four. As before, we can express the PNN as the development of the summation in (4.10) using the expression in (4.6) for the probability distribution function.

Doing so, we obtain that:

$$PNN[n] = a_2\tau_{os}^2 + \tau_{os} + \frac{a_2}{2}, \tag{4.15}$$

where the offset τ_{os} is:

$$\tau_{os} = \frac{-1+\sqrt{1-2a_2^2}}{2a_2}. \tag{4.16}$$

The result in (4.15) shows that the PNN is independent of n. This suggests that a quadratic nonlinearity does not produce spurs when a MASH 1-1-1 modulator is employed.

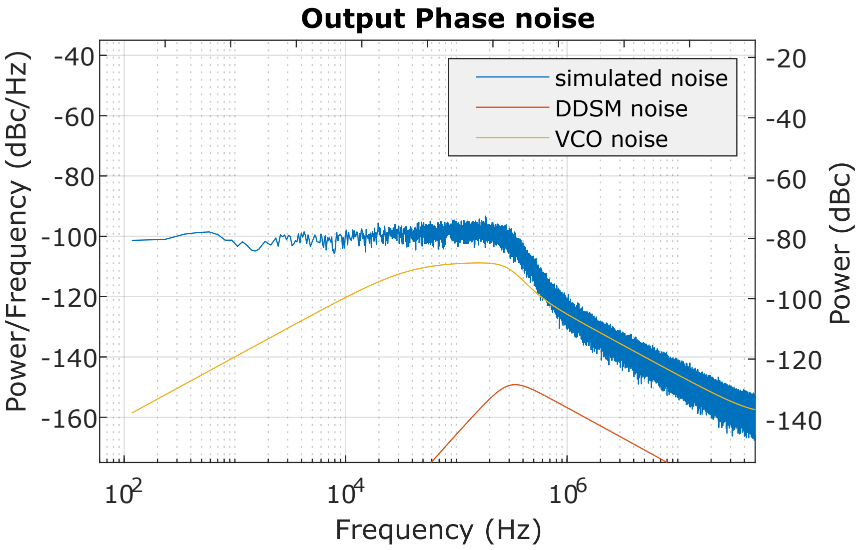

Figure 4.5: Simulated output phase noise in the case of a MASH 1-1-1 DDSM and quadratic nonlinearity with $a_2 = 0.02$.

Fig. 4.5 shows the output phase noise simulated with the closed loop model when $a_2 = 0.02$. The result confirms the absence of spurious tones. On the other hand, the folded noise introduced by the nonlinearity produces a flat component of noise that puts a lower bound on the in-band noise floor. Performing multiple simulations with different values of a_2, we note that the level of the in-band noise floor scales with the value of a_2. We do not go into the details of the relationship between the in-band noise floor and the coefficients of the nonlinearity, as this will be further discussed in the next chapter.

MASH 1-1-1-1

Lastly, the fourth-order MASH 1-1-1-1 modulator generates an accumulated error e_{acc} that lies on eight tracks. Following the same procedure, we obtain a PNN equal to:

$$PNN[n] = a_2\tau_{os}^2 + \tau_{os} + \frac{5}{3}a_2, \tag{4.17}$$

with τ_{os} that is:

$$\tau_{os} = \frac{-1+\sqrt{1-\frac{20}{3}a_2^2}}{2a_2}. \tag{4.18}$$

The PNN is also constant in this case; Fig. 4.6 is spur-free. It is worth noting that the in-band phase noise level is higher than in the previous case. This is due to the fact that, even if the nonlinearity is the same, a MASH 1-1-1-1 generates

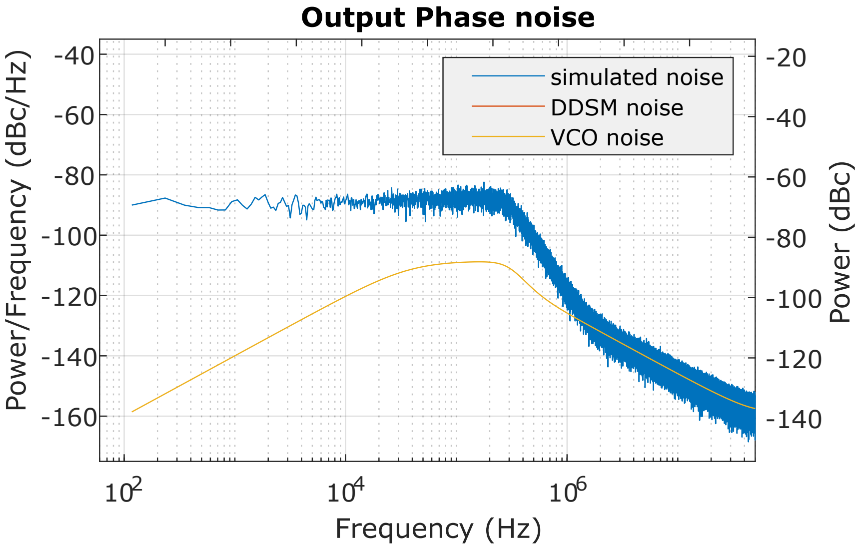

Figure 4.6: Simulated output phase noise in the case of a MASH 1-1-1-1 DDSM and quadratic nonlinearity with $a_2 = 0.02$.

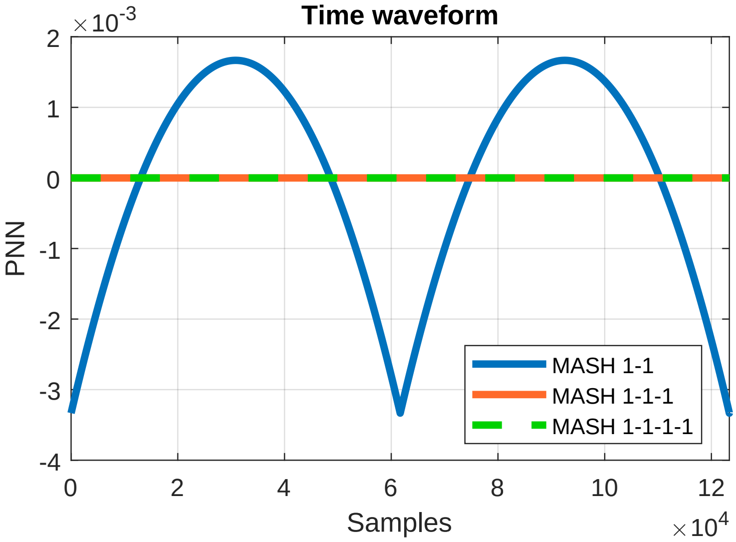

Figure 4.7: PNN time waveforms in the cases of MASH 1-1, MASH 1-1-1 and MASH 1-1-1-1 DDSMs and quadratic nonlinearity with $\alpha = 0.02$.

an e_{acc} with a wider range. Therefore, the input phase error interacts with the nonlinearity over a larger range, generating more folded noise that appears as in-band noise. The level again scales with the coefficient a_2.

The PNN time waveforms for the cases of Figs. 4.4, 4.5, and 4.6 are plotted in Fig. 4.7 using the expressions (4.13), (4.15), and (4.17) with τ_{os} given, respectively, as in (4.14), (4.16), and (4.18) with $a_2 = 0.02$.

4.3.2 Cubic Nonlinearity

Next we analyze the case where the nonlinearity is cubic. Specifically, the nonlinear function $\mathcal{N}(\cdot)$ is composed of the sum of only the linear and cubic terms. Similarly to what we have seen in the previous subsection, we can write the PNN explicitly as:

$$PNN[n] = \sum_{k} \left[\left(k + w[n] + \tau_{os} + a_3 \left(k + w[n] + \tau_{os} \right)^3 \right) \cdot P\left(k + w[n] \right) \right] \quad (4.19)$$

The range of k and the function $P(\cdot)$ vary according to the order of the MASH modulator. Next we calculate the PNN for each of three considered modulators.

MASH 1-1

The MASH 1-1 modulator generates a signal e_{acc} whose samples lie on two tracks, τ_1 and τ_2. This information and the probability distribution function in (4.5) combined with (4.19) give:

$$PNN[n] = a_3\left(-2w^3[n] - 3(1+\tau_{os})w^2[n] - (1+3\tau_{os})w[n] + \tau_{os}^3\right) + \tau_{os}, \quad (4.20)$$

where τ_{os} is equal to 0. This result is discussed in detail for τ_{os} in Appendix C.

From (4.20) we deduce that a MASH 1-1 based CP-PLL will exhibit spurs when it has a cubic nonlinearity. Fig. 4.8 shows the simulated output phase noise when $a_3 = 0.02$. The result exhibits a spurious pattern, as expected.

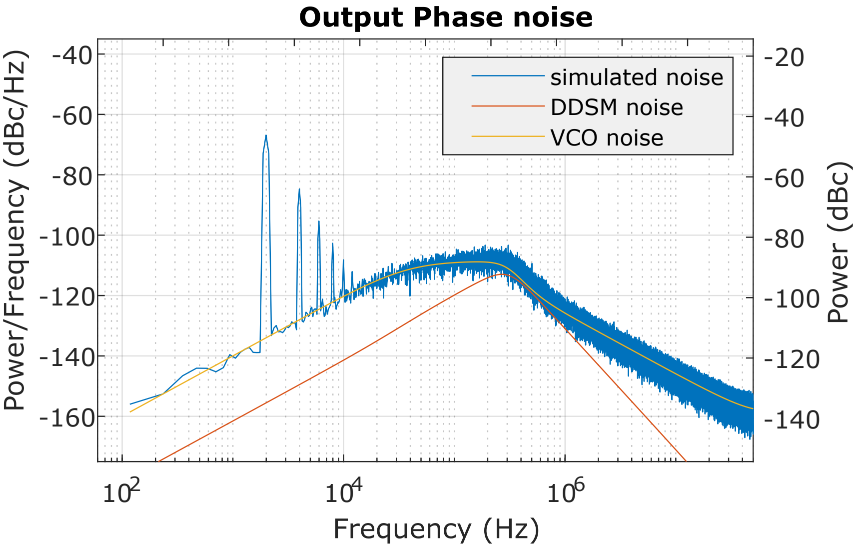

Figure 4.8: Simulated output phase noise in the case of a MASH 1-1 DDSM and quadratic nonlinearity with $a_3 = 0.02$.

MASH 1-1-1

Repeating the analysis in the case of a MASH 1-1-1 DDSM returns the following expression for the PNN:

$$PNN[n] = a_3\left(w^3[n] + \frac{3}{2}w^2[n] + \frac{1}{2}w[n] + \frac{3}{2}\tau_{os} + \tau_{os}^3\right) + \tau_{os}, \tag{4.21}$$

where τ_{os} is also equal to 0 in this case.

According to (4.21), a CP-PLL with a MASH 1-1-1 modulator will exhibit spurs when there is a cubic nonlinearity in the system.

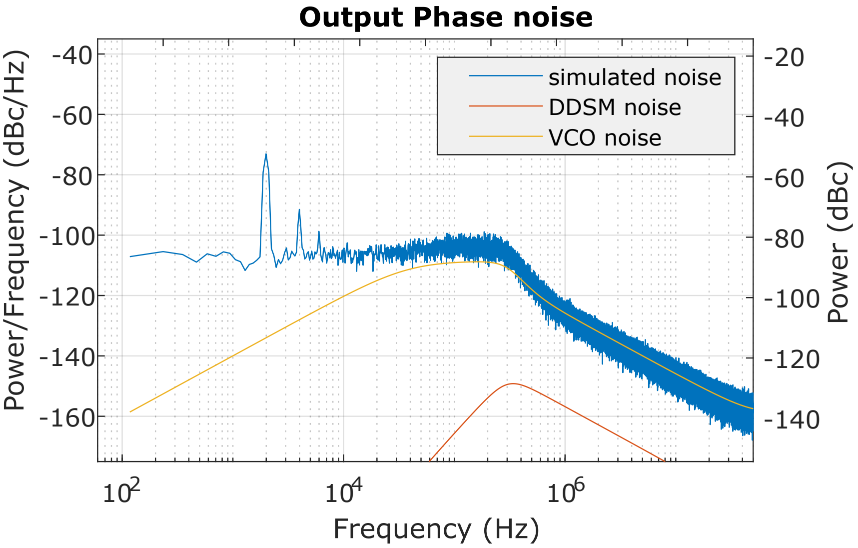

Figure 4.9: Simulated output phase noise in the case of a MASH 1-1-1 DDSM and quadratic nonlinearity with $a_3 = 0.02$.

An example is given in Fig. 4.9 with $a_3 = 0.02$. The simulated output phase noise exhibits a set of spurs, as expected. Moreover, the spurious tones decrease in magnitude (by $\approx$ 6 dB) compared to those in the previous case while, on the other hand, a larger component of nonlinearity-induced noise shows up as in-band floor noise. The reduction in the magnitudes of the spurs can be deduced from (4.20) and (4.21). In fact, knowing that τ_{os} is equal to zero in both cases, the resulting PNN in (4.20) is equal to minus two times that in (4.21). Therefore, the PSDs of the two functions are identical, except for a 6 dB offset.

In conclusion, this modulator guarantees immunity to spurs when the nonlinearity is quadratic but *not* when it is cubic.

MASH 1-1-1-1

Doing the same analysis once again and considering eight tracks with $k \in \{-3, -2, ..., 4\}$ and the function $P(\cdot)$ as in (4.7), we obtain:

$$PNN[n] = a_3 \left(5\tau_{os} + \tau_{os}^3\right) + \tau_{os}, \tag{4.22}$$

where τ_{os} is equal to 0.

By contrast with the previous case, a MASH 1-1-1-1 is immune from spurs when the nonlinearity is cubic. This result is illustrated by the example shown in Fig. 4.10 where we considered $a_3 = 0.02$. The simulated output phase noise exhibits no spurs, while the PNN time waveform is zero.

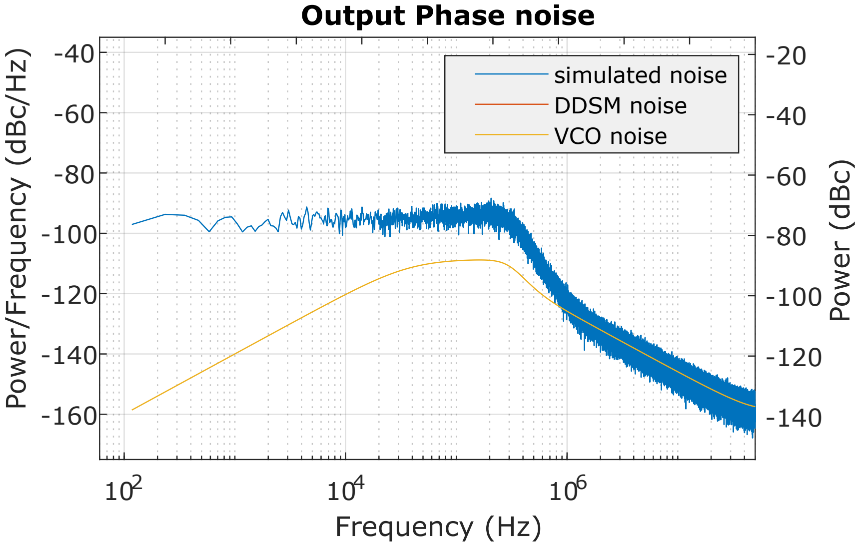

Figure 4.10: Simulated output phase noise in the case of a MASH 1-1-1-1 DDSM and quadratic nonlinearity with $a_3 = 0.02$.

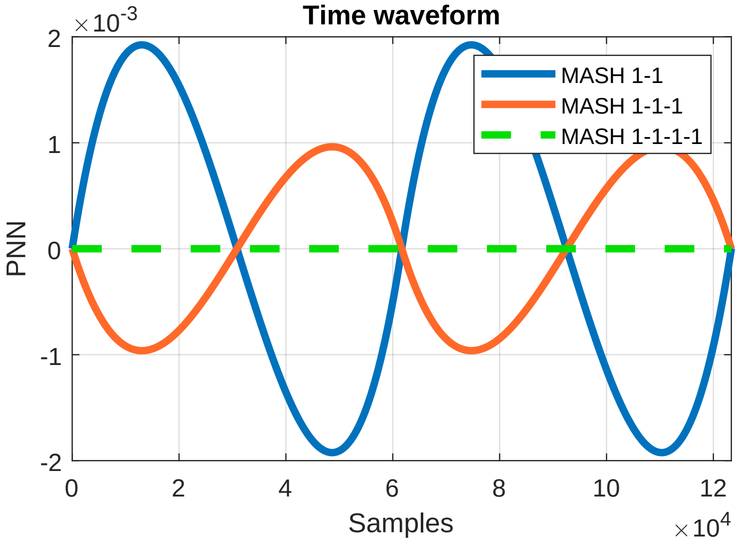

Figure 4.11: PNN time waveforms in the cases of MASH 1-1, MASH 1-1-1 and MASH 1-1-1-1 DDSMs and cubic nonlinearity with $a_3 = 0.02$.

Fig. 4.11 shows the PNN time waveforms for the cases of Figs. 4.8, 4.9, and 4.10 obtained from (4.20), (4.21), and (4.22) with τ_{os} null and $a_3 = 0.02$.

4.3.3 Third-order Polynomial Nonlinearity

Finally, we consider the generic case where both the coefficients a_2 and a_3 are non-zero. The nonlinear function is expressed as:

$$\mathcal{N}(x) = x + a_2 x^2 + a_3 x^3 \tag{4.23}$$

Substituting (4.23) in (2.16), gives:

$$PNN[n] = \sum_k \left(\hat{\tau}_k(n) + a_2\hat{\tau}_k^2(n) + a_3\hat{\tau}_k^3(n)\right) P(\tau_k(n)). \tag{4.24}$$

By virtue of the fact that summation is a linear operation, we can express the PNN as:

$$PNN[n] = \sum_k \hat{\tau}_k(n)P(\tau_k(n)) + \sum_k a_2\hat{\tau}_k^2(n)P(\tau_k(n)) + \sum_k a_3\hat{\tau}_k^3(n)P(\tau_k(n)), \tag{4.25}$$

where the first summation returns τ_{os} for all the MASH modulators we consider. The other two sums in (4.25) are obtained directly from the results of the previous two subsections.

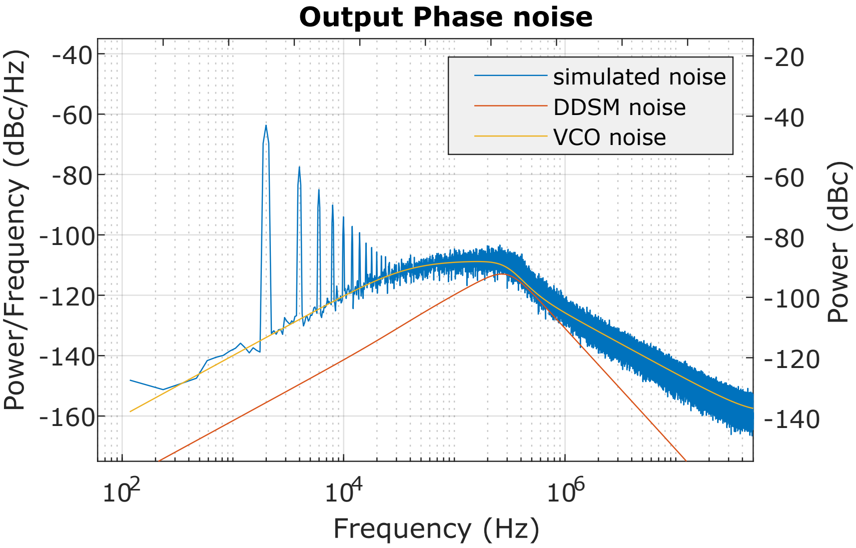

Figure 4.12: Simulated output phase noise in the case of a MASH 1-1 DDSM and third-order polynomial nonlinearity with $a_2 = 0.02$ and $a_3 = 0.02$.

In the case of a MASH 1-1, the PNN is:

$$\begin{aligned} PNN[n] = \tau_{os} + a_2\left(\tau_{os}^2 - w[n]\right)(w[n]+1) + a_3 \cdot \\ \left(-2w^3[n] - 3\left(1+\tau_{os}\right)w^2[n] - \left(1+3\tau_{os}\right)w[n] + \tau_{os}^3\right), \end{aligned} \tag{4.26}$$

while, in the case of a MASH 1-1-1, the PNN becomes:

$$PNN[n] = \tau_{os} + a_2\left(\frac{1}{2} + \tau_{os}^2\right) + a_3\left(w^3[n] + \frac{3}{2}w^2[n] + \frac{1}{2}w[n] + \frac{3}{2}\tau_{os} + \tau_{os}^3\right) \tag{4.27}$$

Lastly, in the case of a MASH 1-1-1-1 the PNN is:

$$PNN[n] = \tau_{os} + a_2 \left(\frac{5}{3} + \tau_{os}^2 \right) + a_3 \left(5\tau_{os} + \tau_{os}^3 \right) \tag{4.28}$$

In summary, a third-order nonlinearity will induce spurs if at least one of the quadratic or cubic terms would lead to a non-constant PNN time waveform. Therefore, among the modulators considered, only the MASH 1-1-1-1 guarantees no spurs when a third-order nonlinearity is present.

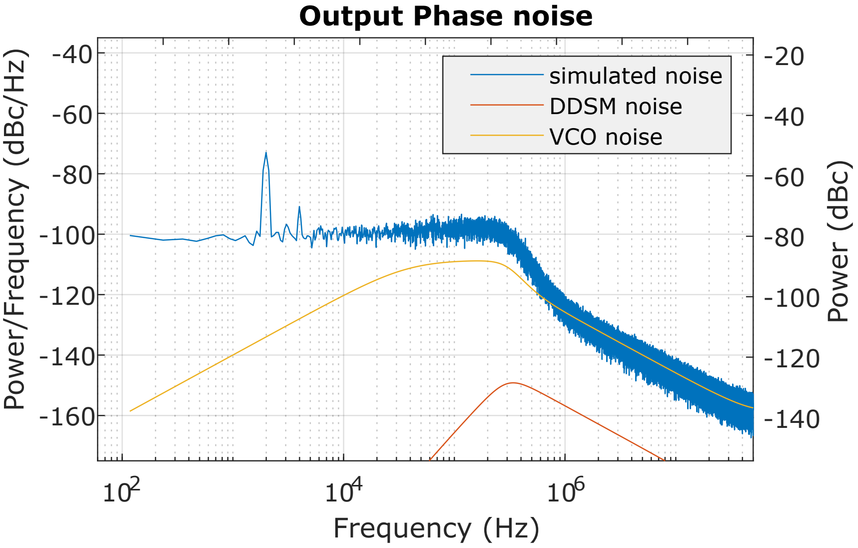

Figure 4.13: Simulated output phase noise in the case of a MASH 1-1-1 DDSM and third-order polynomial nonlinearity with $a_2 = 0.02$ and $a_3 = 0.02$.

As mentioned before, the value of τ_{os} must zero the mean value of the PNN. In order to find τ_{os} analytically, one should solve a parametric third-order equation with the two parameters a_2 and a_3. Alternatively, one can derive the value of τ_{os} numerically once the coefficients a_2 and a_3 are known.

Figs. 4.12, 4.13, 4.14 and 4.15 show the results for the three MASH modulators when both a_2 and a_3 are equal to 0.02. As forecast by the equations, only the MASH 1-1-1-1 is immune from spurs when there is a third-order nonlinearity. As

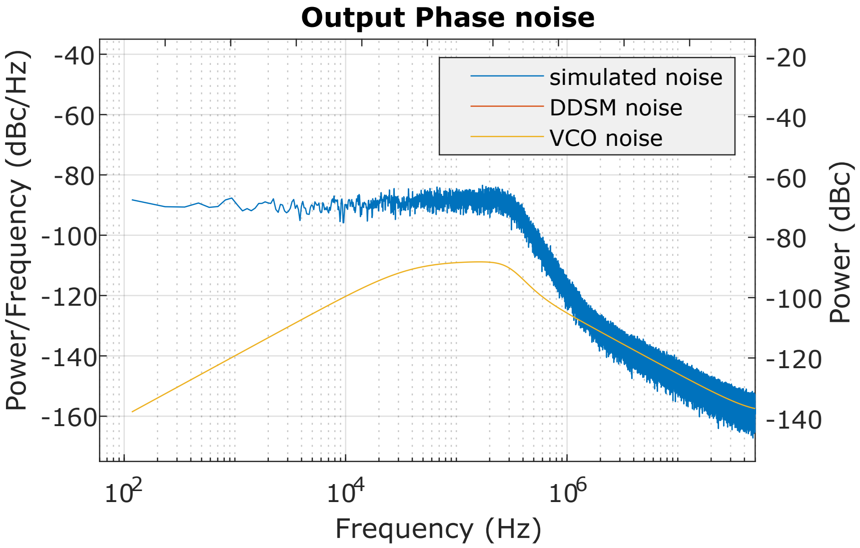

Figure 4.14: Simulated output phase noise in the case of a MASH 1-1-1-1 DDSM and third-order polynomial nonlinearity with $a_2 = 0.02$ and $a_3 = 0.02$.

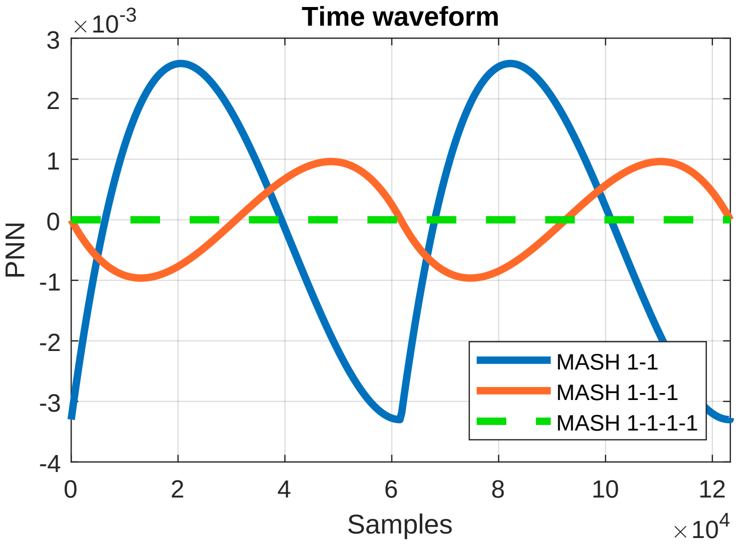

Figure 4.15: PNN time waveforms in the cases of MASH 1-1, MASH 1-1-1 and MASH 1-1-1-1 DDSMs and third-order polynomial nonlinearity with $a_2 = 0.02$ and $a_3 = 0.02$.

a drawback, this case is affected worse by the nonlinearity because of the wider range of e_{acc}. This translates into a higher in-band noise floor.

Both cases with MASH 1-1 and MASH 1-1-1 modulators show spurs in the output phase noise. However, they show different magnitudes for the spurs and the in-band noise levels. The trade-off between spurs and noise floor is mainly due to the fact that, in the case of a MASH 1-1, both the quadratic and the cubic terms contribute to the generation of spurs while, in the case of a MASH 1-1-1, this is true only for the cubic component.

4.4 Discussion

From the analysis carried out in Section 4.3, we notice a relationship between the order of a MASH modulator and the order of the polynomial nonlinearity to which the DDSM has spur immunity. In particular, the results shown so far demonstrate that a MASH 1-1 is spur-free only in the case of a first-order function $\mathcal{N}(\cdot)$ while a MASH 1-1-1 is immune to spurs in the case of polynomial nonlinearities up to second order. Regarding the case of a MASH 1-1-1-1 modulator, we showed that a third-order polynomial nonlinearity does not induce spurs. For the sake of completeness, we ask if a third-order nonlinearity constitutes a limit beyond which a MASH 1-1-1-1 modulator does not guarantee the immunity from spurs any more.

Fig. 4.16 shows the simulated output phase noise and PNN time waveform when a fourth-order nonlinearity $(x + 0.02x^4)$ is applied. The PNN displayed in Fig. 4.16(b) shows a periodic non-zero time waveform. Therefore, we expect spur generation. This is confirmed by Fig. 4.16(a) which shows a visible spur emerging from the in-band noise floor[3]. The spur is highlighted by the PSD of the PNN

---

[3] In order to make the spur in Fig. 4.16(a) visible and distinguishable, the length of the

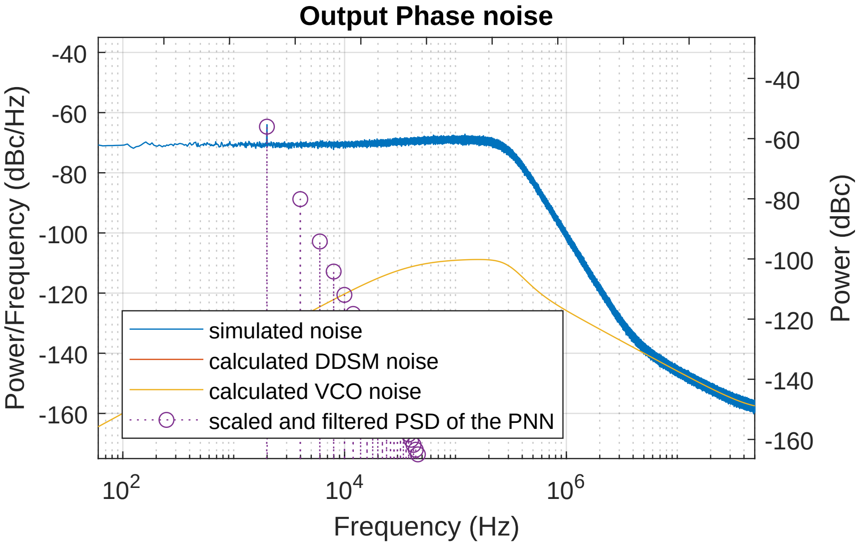

(a)

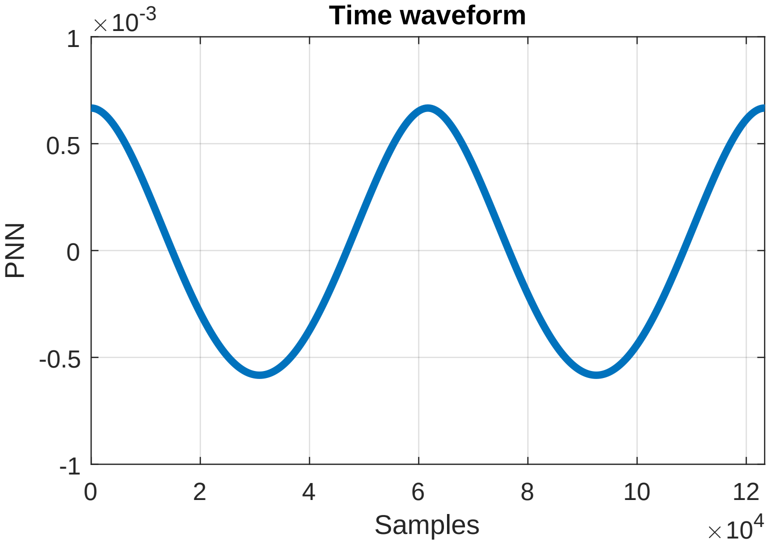

(b)

Figure 4.16: (a) Simulated output phase noise and (b) PNN time waveform (calculated numerically from (2.16)) in the case of a MASH 1-1-1-1 DDSM and fourth-order polynomial nonlinear function $\mathcal{N}(x) = x + 0.02x^4$.

---

simulation has been increased to achieve a smaller frequency resolution. First-order shaped LSB dither has been used to improve the randomization of the DDSM quantization noise. The plotted simulated output phase noise has been obtained by averaging multiple simulation results.

after being scaled and filtered by the closed loop transfer-function. In fact, this represents a prediction of nonlinearity-induced spurs [32].

In summary, we have shown that lth-order MASH modulators, with l ranging from 2 to 4, are inherently immune to spurs in cases of polynomial nonlinearities up to $(l - 1^{st})$-order. We hypothesize that the result holds for all l.

For the sake of completeness, it is important to consider also other performance characteristics for a frequency synthesizer, such as in-band phase noise and RMS jitter. For comparison purposes, these performances are listed in Table 4.1 for the simulated cases shown in Section 4.3[4]. One might notice that, for the cases considered, the MASH 1-1 provides the best in-band phase noise, which is actually determined by the VCO noise, at the expense of big spurious tones. These spurs are larger than those produced by the other MASH modulators with the same nonlinearity. The low in-band phase noise and the large spurs counterbalance each other when evaluating the integrated phase noise. In fact, when a MASH 1-1 is employed, the calculated RMS jitter is comparable to that obtained when using a MASH 1-1-1, despite the fact that the latter case experiences higher in-band phase noise. That being said, the choice of a MASH 1-1-1 provides a fairly good compromise between spur generation and integrated phase noise. Lastly, the MASH 1-1-1-1 allows one to benefit from a more extensive spur immunity at the cost of a markedly higher in-band phase noise and RMS jitter. Note again that, in our simulations, we did not consider the reference noise or charge pump current noise contributions, which will typically dominate in band.

---

[4] The RMS jitter has been calculated in the range from 1 kHz to 10 MHz using the MATLAB algorithm in [52].

Table 4.1: Performances for the simulated cases

Nonlinear function $\mathcal{N}(x)$	DDSM	Spur Immunity	Worst Spur (dBc)	In-band Phase Noise at 1 kHz (dBc/Hz)	RMS Jitter (fs)
$x + 0.02x^2$	MASH 1-1	×	-45.7	-140	290
	MASH 1-1-1	✓	N.D.	-102	322
	MASH 1-1-1-1	✓	N.D.	-89	1082
$x + 0.02x^3$	MASH 1-1	×	-46.2	-140	273
	MASH 1-1-1	×	-52.4	-107	219
	MASH 1-1-1-1	✓	N.D.	-96	563
$x + 0.02x^2 + 0.02x^3$	MASH 1-1	×	-43	-138	380
	MASH 1-1-1	×	-52.3	-102	372
	MASH 1-1-1-1	✓	N.D.	-89	1139

4.5 Summary

In this chapter, we have demonstrated how MASH modulators can theoretically exhibit spur immunity in fractional frequency synthesizers with memoryless polynomial nonlinearities. In particular, we analyzed three modulators: MASH 1-1, MASH 1-1-1 and MASH 1-1-1-1. If l is the order of the modulator, we hypothesize that for $l \geq 2$ spur immunity is guaranteed in the case of a polynomial nonlinearity with an order up to $(l-1)$. This was shown analytically for $2 \leq l \leq 4$ by studying the PNN and confirmed by simulation of a closed loop model of the synthesizer.

Chapter 5

Folded Noise Prediction in Nonlinear Fractional-N Frequency Synthesizers

The presence of nonlinearities in a synthesizer leads not only to the generation of spurious tones but also an elevated noise floor [29], [30], [53], [54]. The latter can be interpreted as folding of the high-frequency quantization noise into the passband of the PLL. Therefore, it is also referred to as folded noise [28], [51]. In this chapter, we provide a detailed analysis on the generation of folded noise and a method to predict it.

5.1 Introduction

In the past, several authors have presented different predictions for the folded noise induced by nonlinearities in the frequency synthesizer: see [28], [55] and [56] for example. Their analyses follow diverse analytical approaches; however, they all share the assumption of a Gaussian distribution for the phase error induced by the modulator. This allows one to determine the variance of the noise when distorted by the nonlinearity [28], or to derive mathematically its autocorrelation and power spectral density (PSD) using Price's theorem[1] [55]. In this chapter we present a different approach for analyzing the folded noise which does not require the assumption that the modulation noise has a Gaussian distribution. The method is developed for different DDSMs, allowing one to predict the folded noise for various types of memoryless nonlinearities. The results, which are compared with the predictions provided by previous works, and also confirmed by simulation, show that this method is the most accurate developed to date.

5.2 Prediction Method

The purpose of this work is to predict the elevated noise floor generated by the nonlinearity in the synthesizer. In the past, several different ways to predict the nonlinearity-induced folded noise have been presented [28], [55] and [56]. Even though these methods were different from each other, they all assumed that the modulation error, herein denoted $e_{acc}[n]$, is characterized by a Gaussian distribution. It is clear that the hypothesis of Gaussian distribution for $e_{acc}[n]$, is just an approximation for modulators with NTFs like (2.5), since the signal $e_{acc}[n]$ is bounded by definition (4.3). That said, this assumption may be a fairly good approximation in some cases, while in others it is not [58], [59]. Let us denote by $P(e_{acc})$ the probability distribution of $e_{acc}[n]$. Fig. 5.1 shows the simulated $P(e_{acc})$ for the cases of third-order and fourth-order MASH modulators. One may notice that they are qualitatively different from each other. In particular, while the probability distribution resembles a truncated Gaussian in Fig. 5.1(b),

---

[1] Price's theorem relates the input and output autocorrelation functions of a nonlinear block under the hypothesis of a Gaussian process as input [57].

this is less clear for the case in Fig. 5.1(a).

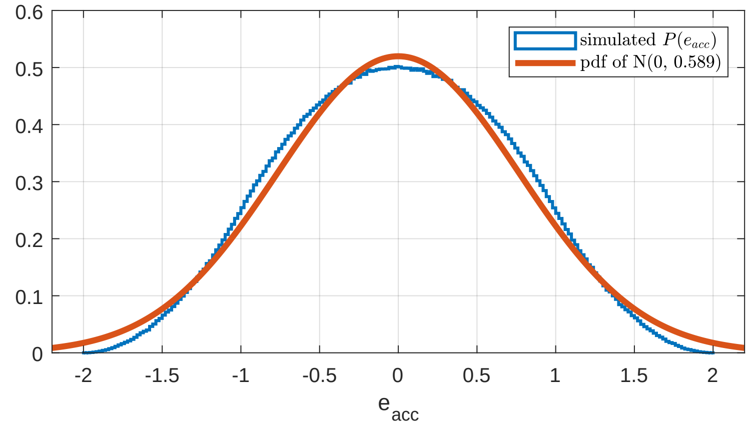

(a)

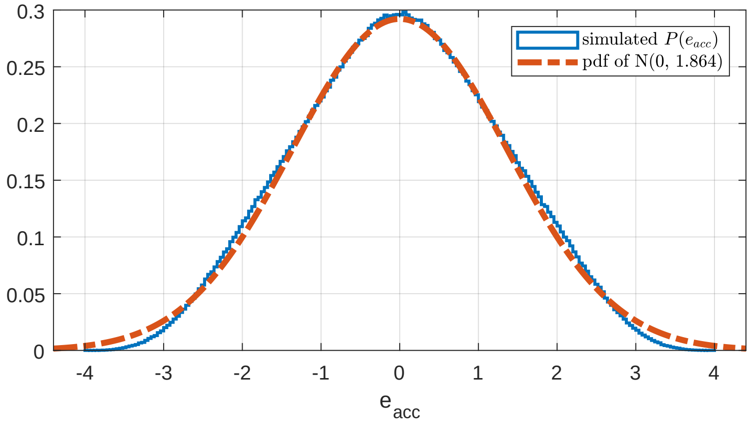

(b)

Figure 5.1: Simulated probability distributions of $e_{acc}[n]$ in the cases of (a) MASH 1-1-1 and (b) MASH 1-1-1-1 modulators.

In this section we provide a new prediction method for the noise floor that follows a different approach. We do not assume a specific probability distribution for $e_{acc}[n]$ *a priori*. In fact, the proposed method aims to evaluate directly and analytically the power spectral density of $e_{acc}^{NL}[n]$, i.e. the accumulated quantization error after distortion by the nonlinearity, given $\mathcal{N}(\cdot)$. From (4.3) and (2.12), one can see that $e_{acc}^{NL}[n]$ is a function of the error $e[n]$ generated by the quantizer. By definition, $e[n]$ is a discrete-valued signal, in the range $\left[-1+\frac{1}{M}, 0\right]$ with steps $\frac{1}{M}$. However, the modulus of a DDSM is generally quite large so we make the approximation to assume that $e[n]$ is continuous-valued.

At this point, we need to make two assumptions about e, which are that it is a uniform and independent and identically distributed (i.i.d.) stochastic process. As mentioned before, it is possible to randomize $e[n]$ sufficiently so that it can be considered uniformly distributed [25], [60]. Therefore, we regard e as a $\mathcal{U}(-1,0)$ random process. The independence of the process e is only an approximation. However, we will see later that this assumption provides accurate results in important practical cases.

The i.i.d. hypothesis for e implies that its autocorrelation, namely $R_e[n_0]$, is equal to the squared mean value, μ_e^2, for any $n_0 \neq 0$, whereas it is equal to μ_e^2 plus the variance σ_e^2 for $n_0 = 0$ [61]. According to the assumption of a uniform distribution $\mathcal{U}(-1,0)$, μ_e^2 and σ_e^2 are respectively equal to $\frac{1}{4}$ and $\frac{1}{12}$ [61]. Then, the Wiener–Khinchin theorem can be used. This states that the power spectral density of a wide-sense-stationary (WSS) random process is given by the Fourier transform of its autocorrelation function [62], [63]. Because of the i.i.d. assumption, e is WSS and the Wiener–Khinchin theorem is applicable. Furthermore, from the expression in (4.3), one may notice that, because e is WSS, so is e_{acc}. Therefore, $S_{e_{acc}}(f)$ is obtained by the discrete-time Fourier transform of the autocorrelation function of e_{acc}, namely $R_{e_{acc}}[n_0]$. The latter is equal to:

$$\begin{aligned} R_{e_{acc}}[n_0] = E\Bigg[&\left(\sum_{k=0}^{l-1}(-1)^k\binom{l-1}{k}e[n-k]\right) \\ &\qquad\left(\sum_{p=0}^{l-1}(-1)^p\binom{l-1}{p}e[n-p-n_0]\right)\Bigg], \end{aligned} \tag{5.1}$$

that, according to the hypotheses on e and considering $l > 1$, returns:

$$R_{e_{acc}}[n_0] = \sum_{k=0}^{l-1} \sum_{p=0}^{l-1} (-1)^{k+p} \binom{l-1}{k} \binom{l-1}{p} \frac{\delta[n_0 + p - k]}{12}. \tag{5.2}$$

This expression can be equivalently written as:

$$R_{e_{acc}}[n_0] = \binom{2(l-1)}{l-1} \frac{\delta[n_0]}{12} + \sum_{q=1}^{l-1} (-1)^q \binom{2(l-1)}{l-1+q} \frac{\delta[n_0 + q] + \delta[n_0 - q]}{12}. \tag{5.3}$$

Then, the PSD becomes:

$$S_{e_{acc}}(f) = \binom{2(l-1)}{l-1} \frac{1}{12} + 2 \sum_{q=1}^{l-1} (-1)^q \binom{2(l-1)}{l-1+q} \frac{\cos(2\pi q f T_s)}{12}. \tag{5.4}$$

With the use of trigonometric power formulas, (5.4) returns:

$$S_{e_{acc}}(f) = \frac{1}{12} \left(2 \sin(\pi f T_s)\right)^{2(l-1)}. \tag{5.5}$$

This result is matched by simulation, as shown for instance in Fig. 2.3(b).

The presented prediction method intends to extend the evaluation to $S_{e_{acc}^{NL}}(f)$. Once $\mathcal{N}(\cdot)$ is given, e_{acc}^{NL} is known from (2.12). Then, the Wiener–Khinchin theorem can be applied. In fact, it can be proven that, in the case of a memoryless nonlinearity which is bounded[2], if e_{acc} is WSS, then e_{acc}^{NL} is also WSS [64]. Therefore, we obtain the PSD of the nonlinearity-induced noise by calculating $S_{e_{acc}^{NL}}(f)$ as the discrete-time Fourier transform of the autocorrelation function of e_{acc}^{NL}, that is:

$$R_{e_{acc}^{NL}}[n_0] = E\left[\mathcal{N}\left(e_{acc}[n] + \tau_{os}\right) \mathcal{N}\left(e_{acc}[n - n_0] + \tau_{os}\right)\right]. \tag{5.6}$$

For the sake of completeness, we note that this method has been applied and will shortly be proven for the cases where $NTF(z)/(1-z^{-1})$ leads to a finite impulsive

---

[2] This is necessary for e_{acc}^{NL} to fulfil the WSS conditions. However, it is also true that $\mathcal{N}(\cdot)$ does not have vertical asymptotes in practice.

response (FIR). In fact, this condition simplifies the calculations described above as the resulting $e_{acc}[n]$ is a linear combination of a *finite* number of delayed versions of $e[n]$. It is worth noting that MASH modulators, as well as EFMs, satisfy this condition.

5.3 Analysis and Simulations

In this section we analyse the noise generated in the synthesizer by different types of nonlinearities. The respective folded noises are predicted using the proposed prediction method. The analysis is accompanied by behavioral simulations of the PLL in order to compare the predicted noise floors with the simulated outcomes.

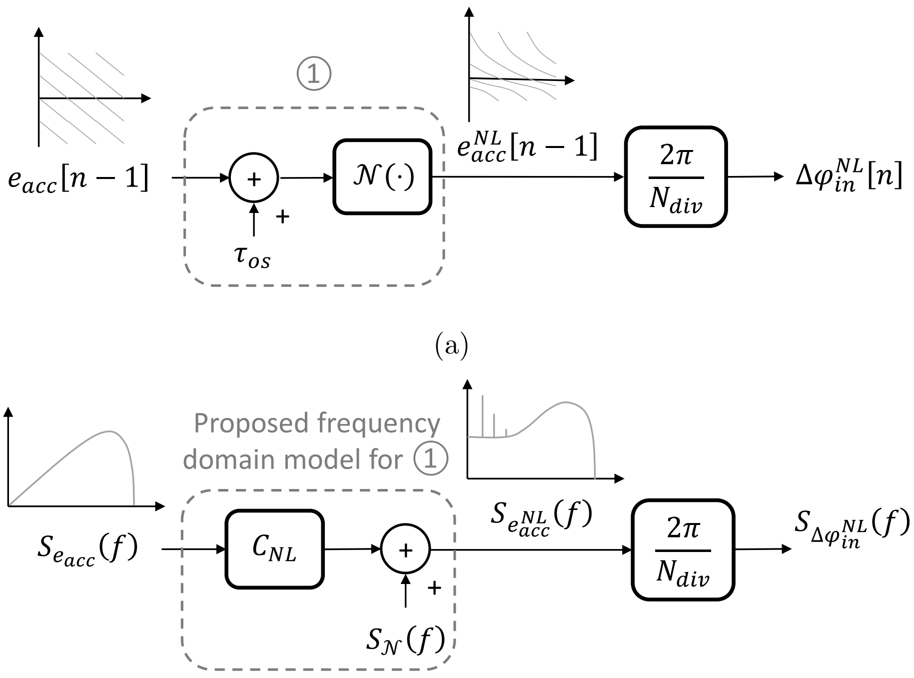

(a)

(b)

Figure 5.2: Block diagram of (a) the time domain model of the nonlinear function $\mathcal{N}(\cdot)$ and (b) the proposed linearized model in the frequency domain.

Once the nonlinear function $\mathcal{N}(\cdot)$ is given, one can obtain $e_{acc}^{NL}[n]$ and evaluate $S_{e_{acc}^{NL}}(f)$ as described in the previous section. At this point, we need to understand how $S_{e_{acc}^{NL}}(f)$ contributes to the total output phase noise of the PLL. In order to do that, let us consider the time domain model presented in Fig. 5.2(a). This illustrates the relationship between $\Delta\phi_{in}^{NL}$ and e_{acc} through the function $\mathcal{N}(\cdot)$, as expressed in (2.11) and depicted in Fig. 2.4. The nonlinear function distorts the accumulated quantization error e_{acc}. It may also introduce a non-zero amplitude offset τ_{os}.

Passing to the frequency domain, a linearized model is needed to express the relationship between $S_{e_{acc}^{NL}}(f)$ and $S_{e_{acc}}(f)$. This is fundamental for estimating the transfer function of the nonlinear system. We propose a linearized model for the nonlinear function in Fig. 5.2(b). It considers that the PSD of $e_{acc}^{NL}[n]$ is equal to the sum of a scaled version of $S_{e_{acc}}(f)$ and an additional noise term, denoted as $S_{\mathcal{N}}(f)$. That said, $S_{e_{acc}^{NL}}(f)$ can be expressed as:

$$S_{e_{acc}^{NL}}(f) = C_{NL}^2 S_{e_{acc}}(f) + S_{\mathcal{N}}(f). \tag{5.7}$$

In particular, the term $S_{\mathcal{N}}(f)$ includes the components of noise generated by the nonlinearity, such as folded noise and spurious tones. The coefficient C_{NL} takes into account the equivalent gain variation with respect to the linear case when the nonlinearity is present. Substituting the concept expressed in Fig. 5.2 into the schematic of the synthesizer, we obtain the frequency domain model for the nonlinear PLL shown in Fig. 5.3. It is worth noticing that we decided to add the noise component $S_{\mathcal{N}}(f)$ directly at the input of the loop, after being scaled accordingly. This allows one to evaluate its contribution to the output phase noise by simply filtering it with the closed-loop transfer function. The latter has been altered by the nonlinearity, as indicated by the presence of the C_{NL} block in Fig. 5.3. Therefore, we will refer to the closed-loop transfer function of the nonlinear system as $G_{NL}(f)$. This differs from the linear closed loop transfer

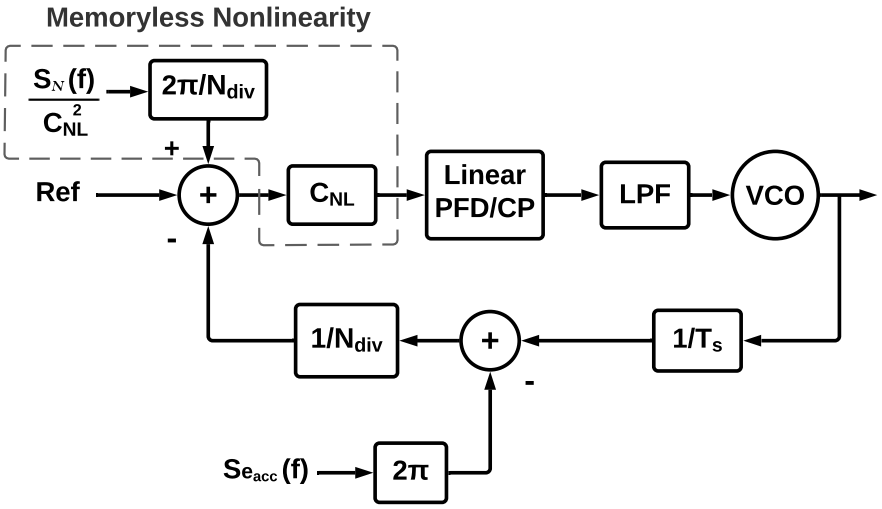

Figure 5.3: Block diagram of a linearized frequency domain model of a nonlinear PLL (adapted from [20]).

function, denoted by $G(f)$, only in terms of the positions of its poles. In fact, the presence of C_{NL} affects only the feed-forward transfer function; hence, the zero remains unchanged. Moreover, since the feed-forward transfer function has a pair of poles at zero, the DC gain does not change. More details are given in Appendix D.

It is important to note that the prediction obtained through the aforementioned method provides only an approximation of the actual folded noise. In fact, the assumption that e is i.i.d. does not reflect reality. If the signal e were a truly independent random process, the nonlinearity-induced noise would not exhibit spurious tones. However, it is well known that fractional spurs are often present at the output of fractional-N frequency synthesizers.

In this section we analyse the cases of quadratic, cubic and piecewise linear (PWL) nonlinearities[3]. For all three nonlinearities we will consider a null zeroth-

---

[3] While a PWL nonlinearity models a CP current mismatch quite well, a polynomial nonlinear-

order term and a unity coefficient for the first-order one. Whilst the latter is a mere choice of normalization, the zeroth-order term can be neglected, since it would be accounted for by the value of τ_{os}. The analysis and respective simulations are performed for the cases of DDSMs with $NTF(z)$ as in (2.5) and orders l equal to 3 and 4.

5.3.1 Quadratic Nonlinearity

Let us consider a quadratic nonlinearity $\mathcal{N}(\cdot)$, such as:

$$\mathcal{N}(x) = x + a_2 x^2. \tag{5.8}$$

This expression can be substituted into (5.6) to evaluate the autocorrelation of the distorted quantization error. According to the order of the modulator, $e_{acc}[n]$ and τ_{os} are also defined. Therefore, according to the hypotheses mentioned in Section 5.2, the PSD of $e_{acc}^{NL}[n]$ can be evaluated as the discrete-time Fourier transform of $R_{e_{acc}^{NL}}[n_0]$. This has been done for the cases of third and fourth-order modulators, whose results are given in (5.9)[4].

For the sake of brevity we do not go through all the calculations. However, we provide a detailed example in Appendix E. These expressions show that the PSD of e_{acc}^{NL} scales with the parameter a_2. It is helpful to consider the resulting $S_{e_{acc}^{NL}}$ as consisting of two distinct parts, as shown in (5.7). In particular, $S_{e_{acc}^{NL}}$ is composed of a term that is related to $S_{e_{acc}}$ by the coefficient C_{NL}^2, added to other

---

ity can be used to approximate a wider range of nonlinearities. Such polynomial approximations have been used in [33], [45]. For this reason, we analyze the cases of quadratic and cubic nonlinearities in order to demonstrate the relative accuracy of the prediction for simple polynomial nonlinearities. In fact, similarly to what is shown in the following, the method can be applied to any generic polynomial nonlinearity.

[4] These calculations, as well as the ones for the following cases, have been performed with the aid of Wolfram Mathematica [65].

components of noise which represents the term $S_{\mathcal{N}}(f)$, as shown in (5.9). The latter includes a constant term that returns the level of the folded noise at low frequencies.

Simulations have also been performed for the cases of MASH 1-1-1 and MASH 1-1-1-1 DDSMs with a quadratic nonlinearity. The resulting phase noises are shown in Figs. 5.4 and 5.5, which also display the predictions defined by (5.9).

In these figures, as well as the following ones, the calculated output VCO noise component is also plotted. This is obtained from the VCO noise described in Table 2.1, which is then filtered by the respective transfer function [20], while considering the model in Fig. 5.3. More details are provided in Appendix D. The trace of the calculated output VCO noise helps the reader to understand the behavior of the simulated phase noise at high frequencies, where the VCO noise component is dominant over the one given by the folded noise. It is worth noting that the results in Figs. 5.4 and 5.5 do not show fractional spurs. In fact, in the previous chapter we proved that MASH modulators with order equal to three and four are immune from spurs in the case of polynomial nonlinearities up to second and third-order respectively [14]. In summary, both figures show a good match between the simulated in-band phase noise and the folded noise predicted by $S_{e_{acc}^{NL}}$ in (5.9).

5.3.2 Cubic Nonlinearity

We consider next the case of a cubic nonlinearity:

$$\mathcal{N}(x) = x + a_3 x^3. \tag{5.11}$$

From the expression for $\mathcal{N}(\cdot)$ and the hypotheses made for e, one can derive the power spectral density of the nonlinearity-induced noise as the Fourier transform of (5.6), where e_{acc} is defined by the modulator and τ_{os} is zero. Doing so, the

Quadratic nonlinearity

$$S_{e_{acc}^{NL}}(f) = \begin{cases} S_{e_{acc}}(f)\ \overbrace{\left(1 - \frac{29}{15}a_2^2\right)}^{C_{NL}^2}\ + \overbrace{\left(-\frac{8}{45}a_2^2\left(2\sin\left(\pi f T_s\right)\right)^2 + \frac{121}{180}a_2^2\right)}^{S_{\mathcal{N}}(f)} & l = 3 \\ S_{e_{acc}}(f)\left(1 - \frac{101}{15}a_2^2\right) + \left(\frac{23}{60}a_2^2\left(2\sin\left(\pi f T_s\right)\right)^4 - \frac{15}{4}a_2^2\left(2\sin\left(\pi f T_s\right)\right)^2 + \frac{19}{2}a_2^2\right) & l = 4 \end{cases} \tag{5.9}$$

Cubic nonlinearity

$$S_{e_{acc}^{NL}}(f) = \begin{cases} S_{e_{acc}}(f)\ \overbrace{\left(1 + \frac{14}{5}a_3 + \frac{55}{28}a_3^2\right)}^{C_{NL}^2}\ + \overbrace{\left(-\frac{42+29a_3}{420}a_3\left(2\sin\left(\pi f T_s\right)\right)^2 + \frac{47}{280}a_3^2\right)}^{S_{\mathcal{N}}(f)} & l = 3 \\ S_{e_{acc}}(f)\left(1 + \frac{49}{5}a_3 + \frac{1681}{70}a_3^2\right) + \left(-\frac{112+481a_3}{280}a_3\left(2\sin\left(\pi f T_s\right)\right)^4 + \frac{2463}{560}a_3^2\left(2\sin\left(\pi f T_s\right)\right)^2 + \frac{307}{120}a_3^2\right) & l = 4 \end{cases} \tag{5.10}$$

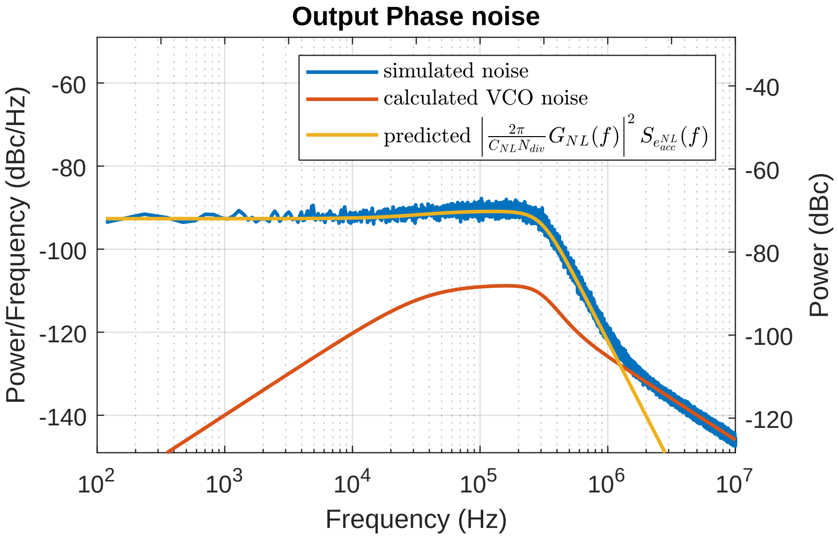

Figure 5.4: Simulated output phase noise and predicted folded noise in the case of a MASH 1-1-1 DDSM and quadratic nonlinearity with $a_2 = 0.05$, $X = 17$ and $M = 2^{20}$.

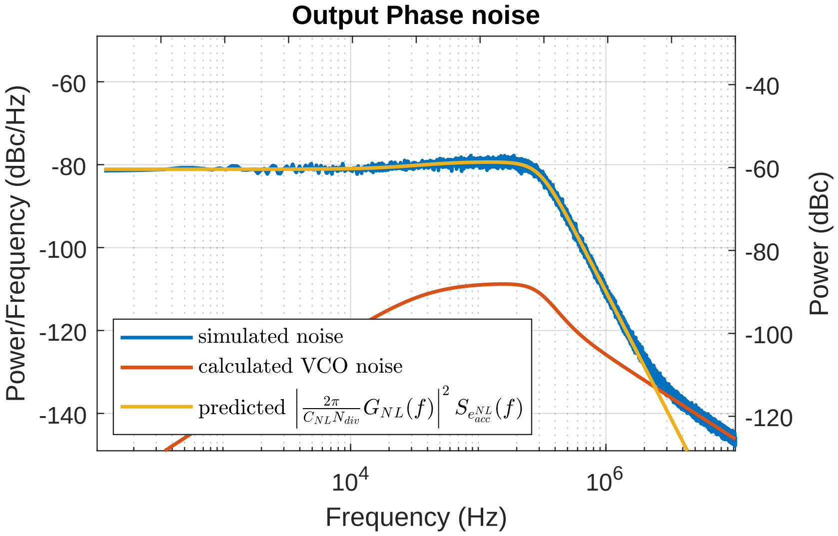

Figure 5.5: Simulated output phase noise and predicted folded noise in the case of a MASH 1-1-1-1 DDSM and quadratic nonlinearity with $a_2 = 0.05$, $X = 17$ and $M = 2^{20}$.

expressions in (5.10) are obtained. As before, for each value of l, $S_{e_{acc}^{NL}}$ has a constant term that gives the folded noise level and a term that is proportional to $S_{e_{acc}}$ which is scaled by a coefficient that we denoted as C_{NL}^2. The value of C_{NL}^2 depends on a_3 and its expression is different for each l. Differently from the case of (5.9), C_{NL}^2 is not an even function of a_3; this means that different results will be experienced depending on the sign of a_3. Moreover, because of the presence of a linear term in each expression for C_{NL}^2, and because of the fact that a_3 (as well as a_2) typically has an absolute value that is much smaller than unity, the value of C_{NL}^2 is more likely to deviate from unity when there is a cubic nonlinearity. In particular, this is accentuated as the order l increases; in fact, the dependency of C_{NL}^2 on a_3 and a_3^2 get stronger. This is reflected in an alteration of the closed loop transfer function of the synthesizer.

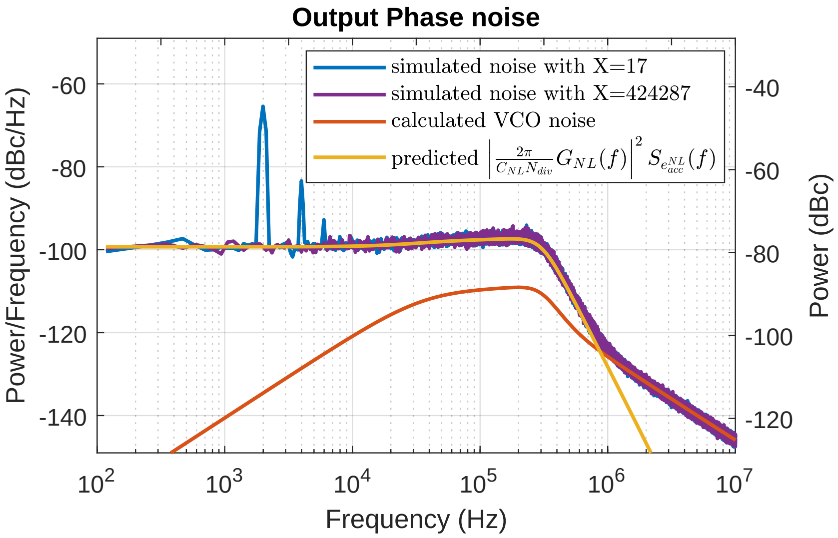

Figure 5.6: Simulated output phase noise and predicted folded noise in the case of a MASH 1-1-1 DDSM, cubic nonlinearity with $a_3 = 0.05$, X equal to 17 and 424287, and $M = 2^{20}$.

Simulations have been performed in the cases of third and fourth-order MASH

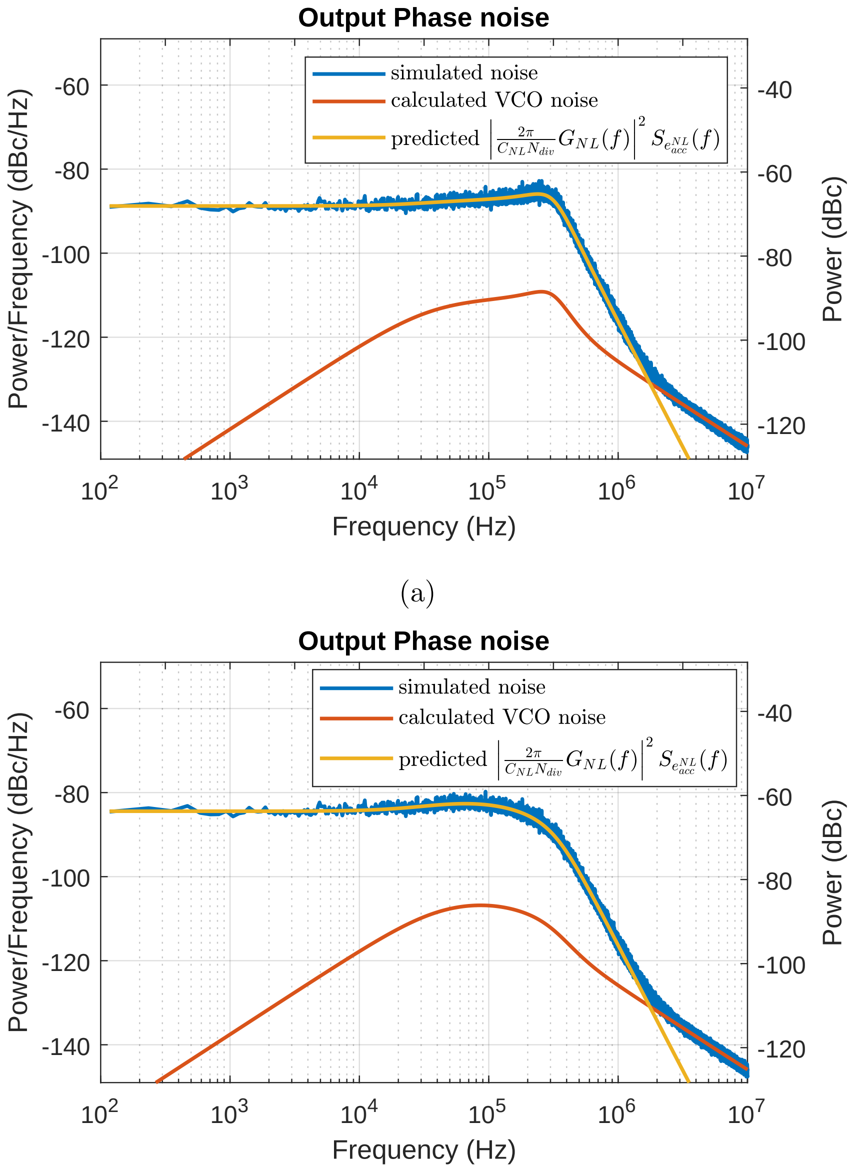

(a)

(b)

Figure 5.7: Simulated output phase noise and predicted folded noise in the case of a MASH 1-1-1-1 DDSM, $X = 17$, $M = 2^{20}$ and cubic nonlinearity with (a) $a_3 = 0.05$, (b) $a_3 = -0.05$.

modulators with a cubic nonlinearity. The results are shown in Figs. 5.6 and 5.7 respectively. The MASH 1-1-1 DDSM experiences spurs. Therefore, the examples of both near-to-integer and far-from-integer conditions are shown in Fig. 5.6[5]. It is worth noting that the simulated folded noise remains the same independently of the value of X. In fact, the simulated phase noises for near-to-integer and far-from-integer conditions overlap in Fig. 5.6, except for the integer boundary spurs.

As expected, the spectral profile of the folded noise depends on the sign of a_3. This is illustrated in Fig. 5.7, where values of ± 0.05 are considered for the coefficient a_3. From the plots, one can notice that the in-band noise floor is almost 5 dB higher in the case of negative a_3 compared to the case of the positive one. Furthermore, the different sign for the value of a_3 is also reflected in the shape of the closed loop transfer function. In fact, when C_{NL} changes, so does the nonlinear closed-loop transfer function $H_{NL}(f)$, as follows from Fig. 5.3. That being said, the predictions in (5.10) provide a good match overall with the simulated folded noise.

5.3.3 Piece-Wise Linear Nonlinearity

The case of a piecewise linear nonlinearity represents a more complex and yet interesting case. It is often used to model the nonlinearity induced in a CP block by mismatch between the *up* and *down* currents [28], [53]. Many authors have discussed the folded noise generated by a PWL nonlinearity; they have taken different approaches which yield different predictions [28], [56]. We will compare these with our method in the following. The nonlinear function $\mathcal{N}(\cdot)$ is expressed

---

[5] The near-to-integer condition is when the fractional division ratio α is close to 0 or 1. When spurs are generated, this condition results in what are called “integer boundary spurs”. Equivalently, one can refer to the far-from-integer condition when α is far from an integer value.

as:

$$\mathcal{N}(x) = x + \frac{e_{CP}}{2}|x|, \tag{5.12}$$

where e_{CP} represents the fractional CP current mismatch.

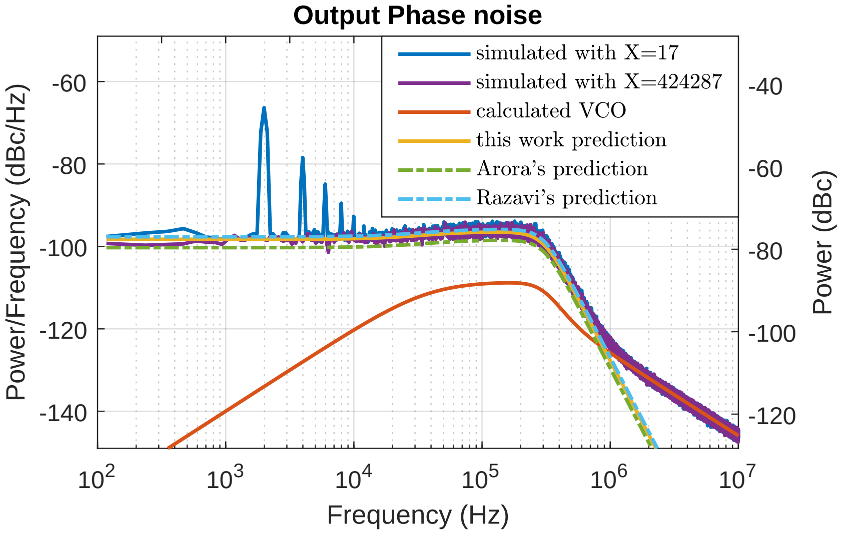

Figure 5.8: Simulated output phase noise and predicted folded noise in the case of a MASH 1-1-1 DDSM, PWL nonlinearity with $e_{cp} = 0.08$, X equal to 17 and 424287, and $M = 2^{20}$.

According to the assumptions made in Section 5.2, we aim to predict the in-band noise level by evaluating the autocorrelation of e_{acc}^{NL}. This is obtained by substituting into (5.6) the expression for $\mathcal{N}(\cdot)$ given in (5.12). In order to calculate $R_{e_{acc}^{NL}}$ and, consequently, $S_{e_{acc}^{NL}}$, it is also necessary to evaluate τ_{os}. As discussed before, τ_{os} must be valued such that e_{acc}^{NL} has zero mean. However, the peculiarity of the PWL nonlinear function (it is not differentiable at zero) makes the evaluation of τ_{os}, parametrically as a function of e_{CP}, hard to compute. This would reflect even more on the complexity of the calculation of $S_{e_{acc}^{NL}}$. That being said, the mismatch error e_{CP} is typically much smaller than unity and so is the offset τ_{os}. For these reasons, we neglect τ_{os} while calculating $S_{e_{acc}^{NL}}$ in the case of

Piece-wise linear nonlinearity

$$S_{e_{acc}^{NL}}(f) = \begin{cases} S_{e_{acc}}(f)\overbrace{\left(1+\frac{e_{CP}^2}{240}\right)}^{C_{NL}^2} + \overbrace{\left(-\frac{149}{8640}e_{CP}^2\left(2\sin\left(\pi f T_s\right)\right)^2+\frac{125}{1728}e_{CP}^2\right)}^{S_{\mathcal{N}}(f)} & l=3 \\ S_{e_{acc}}(f)\left(1-\frac{9283}{6123600}e_{CP}^2\right)+\left(\frac{50509}{5248800}e_{CP}^2\left(2\sin\left(\pi f T_s\right)\right)^4-\frac{7628477}{73483200}e_{CP}^2\left(2\sin\left(\pi f T_s\right)\right)^2+\frac{3582091}{12247200}e_{CP}^2\right) & l=4 \end{cases} \tag{5.13}$$

a PWL nonlinearity[6]. As will be shown shortly, this approximation still allows one to obtain good predictions for the folded noise.

The approximated predicted PSDs for e_{acc}^{NL} in the cases of MASH modulators of order $l = \{3, 4\}$ are given in (5.13)[7]. Simulations have also been performed when those modulators are employed and the PFD/CP block has a PWL nonlinearity with $e_{CP} = 0.08$. The results are shown in Figs. 5.8 and 5.9. For these two cases, both near-to-integer and far-from-integer conditions have been simulated, as a PWL nonlinearity generates spurs for the considered modulators. The results of the simulations confirm a good match with the predictions provided in (5.13), even though we approximated $\tau_{os} \approx 0$. Moreover, Figs. 5.8 and 5.9 also show the predictions obtained from previous works [28], [56]. It is noticeable that the different predictions are similar but slightly divergent, especially for the case of a MASH 1-1-1-1.

5.4 Comparison with State-of-the-Art Predictions

The analysis and the results of the prediction method we have introduced in this work have been provided in the previous section for different test cases. In this section we compare the predictions of our method with the prior art. As mentioned at the beginning of this chapter, other authors have proposed ways to predict the folded noise generated by nonlinearities. Even though their methods follow different approaches, they share the assumption that e_{acc} is characterized

---

[6] In the event that the reader would like to evaluate $S_{e_{acc}^{NL}}$ without neglecting the contribute given by τ_{os}, we suggest calculating τ_{os} numerically once the value of e_{CP} is given.

[7] The neglect of τ_{os} inevitably leads to DC components in $S_{e_{acc}^{NL}}$. However, since the condition of null τ_{os} is only an approximation and the DC terms for $S_{e_{acc}^{NL}}$ are not of interest to the resulting in-band noise levels, they are not reported in (5.13).

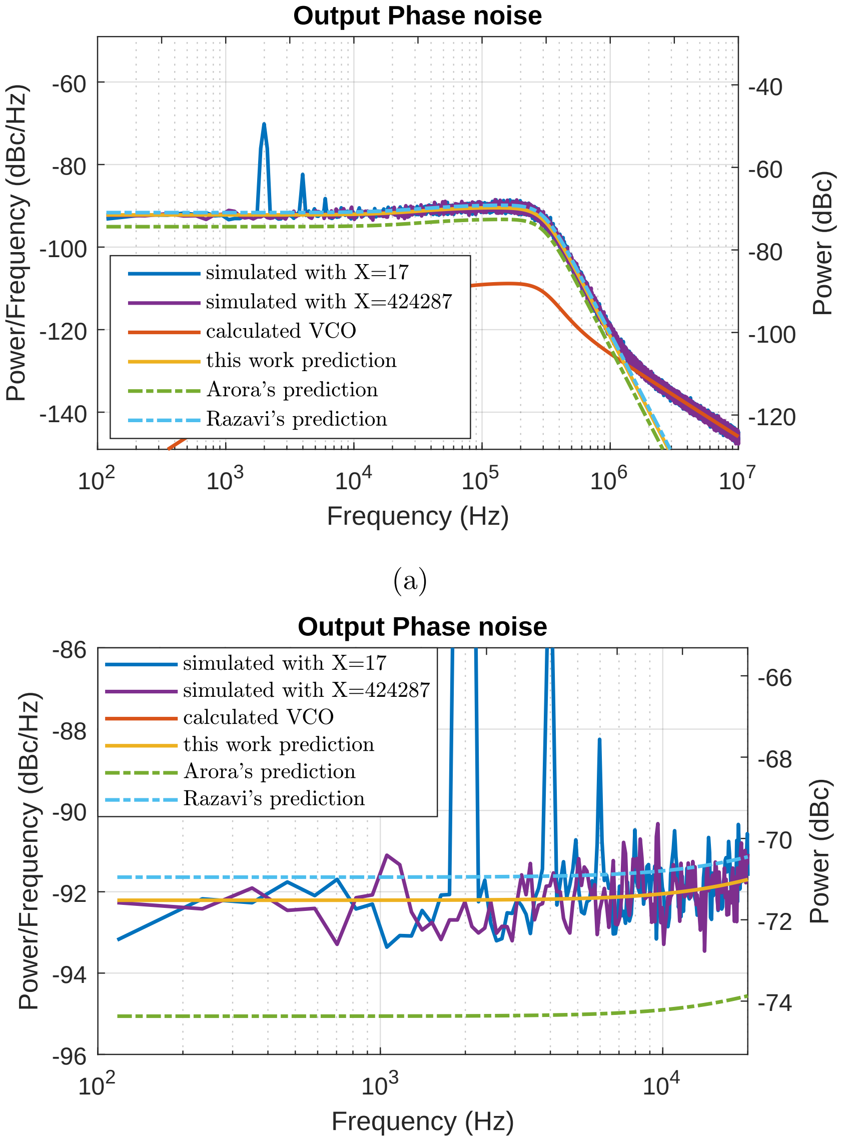

(a)

(b)

Figure 5.9: (a) Far-out and (b) close-up of the simulated output phase noise and predicted folded noise in the case of a MASH 1-1-1-1 DDSM, PWL nonlinearity with $e_{cp} = 0.08$, X equal to 17 and 424287, and $M = 2^{20}$.

by a Gaussian distribution. However, the results in Sec. 5.2 showed that this assumption can be quite far from reality.

The following comparisons between state of the art prediction methods are also accompanied by simulated evaluations of the folded noise levels. These are obtained while considering some particular conditions. For the sake of clarity, the system is simulated with all other (physical) sources of noise switched off. Moreover, the fractional division ratio is chosen far from integers ($X = 424287$) so that no spurs appear in band. Then, the simulated output noise is divided by $\left(\frac{2\pi}{N_{div}}\right)^2 |G_{NL}(f)|^2$. In fact, according to the model in Fig. 5.3, this returns $S_{e_{acc}^{NL}}(f)/C_{NL}^2$. Finally, the average is computed for $f \ll f_{ref}$.

In the work of Hosseini *et al.* [55], the authors have proposed a prediction for the folded noise induced by a polynomial nonlinearity applied to the quantization error e_q of a MASH 1-1-1 DDSM. According to equations (2.3), (2.5) and (2.8), one can realize that the signal e_{acc} of an l-th order MASH modulator is identical to the e_q of a MASH DDSM with order $(l-1)$. This allows one to apply the prediction provided in [55] to the e_{acc} of a MASH 1-1-1-1. That being said, we have compared our predictions to the one provided in [55] for the cases of quadratic and cubic nonlinearities. In particular, the constant term of the predicted noise, $S_{e_{acc}^{NL}}(0)$, is divided by C_{NL}^2 and compared with the prediction given in [55, eq. (24)]. The results are shown in Figs 5.10 and 5.11.

One can notice that the two predictions are very close in the case of Fig. 5.10 (≈ 1.4 dB apart), with the simulated values matching our prediction. Something qualitatively different is shown in Fig. 5.11. Predictions for $S_{e_{acc}^{NL}}(0)/C_{NL}^2$ are provided for both positive and negative a_3, since C_{NL} is not an even function of a_3. These results are closely matched by the simulated results, which establishes not only the accuracy of our prediction method but also the validity of the proposed linearized model. In fact, it takes into account the effect of the nonlinearity on the system's transfer function and the folded noise level. The prediction in [55], by contrast, does not take into account the effect of C_{NL}. However, even if C_{NL}

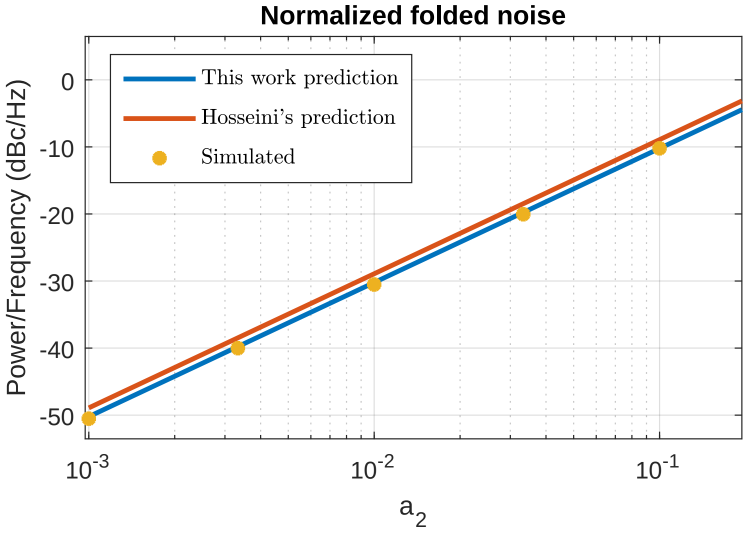

Figure 5.10: Comparison of the predicted folded noise with a state-of-the-art prediction [55] and simulated results in the case of a MASH 1-1-1-1 with a quadratic nonlinearity.

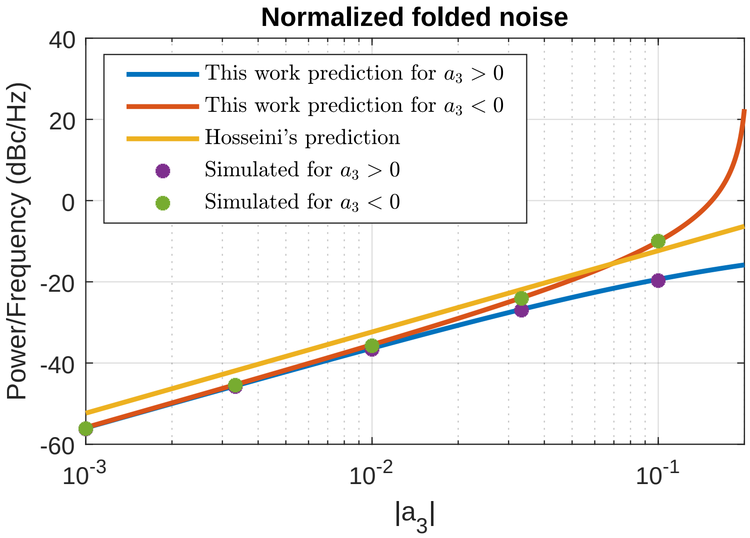

Figure 5.11: Comparison of the predicted folded noise with a state-of-the-art prediction [55] and simulated results in the case of a MASH 1-1-1-1 with a cubic nonlinearity.

is neglected, [55, eq. (24)] returns a result that is ≈ 4 dB higher than $S_{e_{acc}^{NL}}(0)$.

Other authors have proposed predictions for the folded noise generated by a PWL nonlinearity [28], [56]. In the work of Arora *et al.* [28], the authors have provided a prediction given in [28, eq. (20)], that is obtained by assuming that e_{acc} (denoted δ_k in [28]) is Gaussian. This is extended to other types of modulators once the variance of e_{acc} is known. On the other hand, Razavi [56] presented a different approach, also for a PWL nonlinearity, which led to the prediction of the gap between the peak of $S_{e_{acc}}$ and the folded noise as:

$$K = \frac{e_{CP}}{4}, \tag{5.14}$$

given in [56, eq. (6)][8]. These predictions have been compared for the cases of

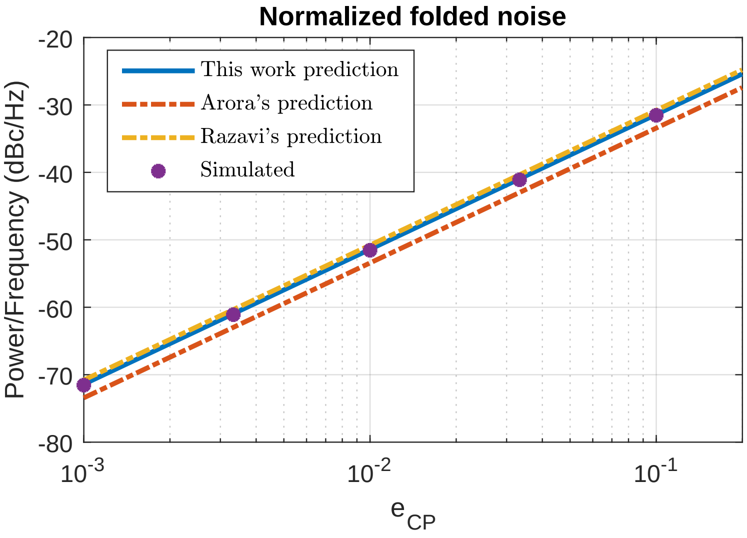

Figure 5.12: Comparison of the predicted folded noise with the state-of-the-art predictions and simulated results in the case of MASH 1-1-1 with PWL nonlinearity.

---

[8] It is worth remarking that the author in [56] uses a different nomenclature. In particular, one should notice that the fraction $\Delta I/I_P$ in [56], represents the fractional CP current mismatch, denoted here as e_{CP}.

MASH modulators with orders equal to 3 and 4, in Figs. 5.12 and 5.13 respectively. One may notice that all the predictions are similar. Arora's prediction deviates slightly (≈ 2–3 dB) from the simulated folded noise for the cases of Figs. 5.12 and 5.13, while the prediction presented in [56] provides quite accurate results in both cases.

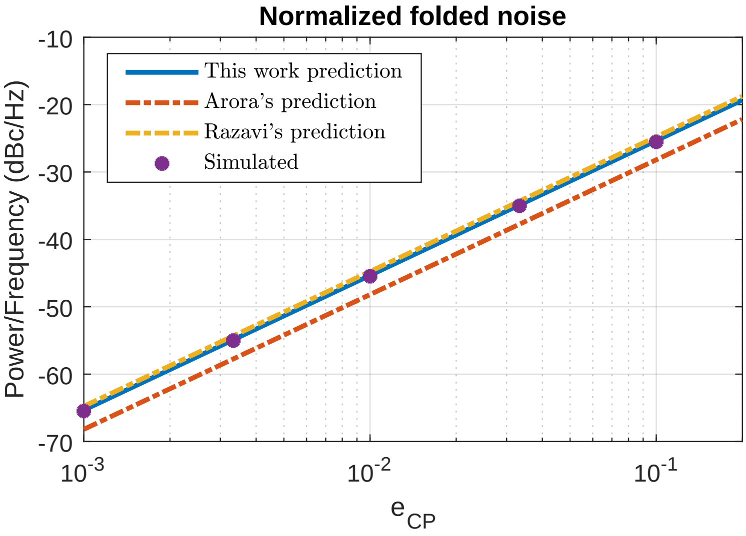

Figure 5.13: Comparison of the predicted folded noise with the state-of-the-art predictions and simulated results in the case of MASH 1-1-1-1 with PWL nonlinearity.

Regarding the complexity of these prediction methods, the one proposed in this work requires the greatest number of calculations. Similar complexity is also encountered when using Hosseini's method. Then, there is Arora's method which requires similar calculations to the one proposed here but with lower complexity. Lastly, Razavi's prediction is the simplest, even though it is applicable only to a PWL nonlinearity[9].

---

[9] It is worth specifying that the analysis presented in [56] approximates a PWL nonlinearity by a quadratic. Even though the resulting prediction works well for PWL nonlinearities, it does not predict accurately the folded noise generated by a quadratic nonlinearity. Moreover, the

Table 5.1: Comparison of MAPEs between the proposed method and prior art predictions

DDSM	$\mathcal{N}(\cdot)$	Hosseini [55]	Arora [28]	Razavi [56]	This method
MASH 1-1-1	PWL (5.12)	N/A	35.17%	18.94%	3.25%
MASH 1-1-1-1	Quadratic (5.8)	42.14%	N/A	N/A	5.35%
	Cubic (5.11) with $a_3 > 0$	225.7%	N/A	N/A	6.12%
	Cubic (5.11) with $a_3 < 0$	99%	N/A	N/A	4.37%
	PWL (5.12)	N/A	46.38%	17.82%	3.38%

The results collected for the comparisons in Figs. 5.10–5.13 are summarized in Table 5.1. In particular, the mean absolute percentage error (MAPE)[10] has been evaluated and compared for the prediction methods listed before. The results show that the prediction method presented in this chapter outperforms the prior art predictions in all the cases considered. It is more accurate and works for both

---

entire approach is based on the downconversion of spectral components near $f_{ref}/2$ when the system experiences an even-order nonlinearity; therefore, it is not directly applicable in the case of odd nonlinearities.

[10] Mean absolute percentage error is a measure of prediction accuracy of a forecasting method. It is defined by the formula: $MAPE = \frac{100}{n}\sum_{t=1}^{n}\left|\frac{A_t-F_t}{A_t}\right|$, where A_t is the actual value and F_t is the forecast one.

polynomial and PWL nonlinearities. The results also confirm that the assumption of a Gaussian distribution for the modulation phase error leads to lower accuracy when predicting the folded noise level.

5.5 Summary

In this chapter, we have analyzed mathematically the output phase noise generated by the interaction between quantization noise and a static nonlinearity in a fractional-N frequency synthesizer. This has led to the formulation of a method that allows one to predict the nonlinearity-induced folded noise for different DDSMs. The prediction method has been analyzed and tested in simulation for different nonlinearities and MASH modulators. The results have confirmed the accuracy of the method. A comparison with state-of-the-art predictions has been performed. It has shown that the presented method produces predictions that are superior to those in the literature. Compared to existing techniques, the presented method delivers greater accuracy for various types of nonlinearities.

Chapter 6

Enhanced Nonlinearity-induced nOise Performance (ENOP) DDSMs

Different types and configurations of DDSMs have been presented in the past which have distinctive characteristics in terms of spectral shaping of the quantization errors, spur immunity and implementation cost. In this chapter we present a novel family of $\Delta\Sigma$ modulators that have high spur immunity and low folded noise when used in fractional-N frequency synthesizers.

6.1 Introduction

As discussed previously, the interaction of the DDSM-related phase error with nonlinearities that are present in the loop leads to the generation of spurious tones and an elevated low-frequency noise floor in a nonlinear fractional-N frequency synthesizer [26], [28], [29]. Many techniques have been developed to linearize the system [39], [40], [41], [44]. While these attenuate the spurs and the folded noise, they do not eliminate them completely because a residual nonlinearity is inevitably present.

A different approach to improving the fractional spur-performance has been pursued by using the Successive Requantizer (SR) [45] and the Probability Mass Redistributor (PMR) [46], [66]; these exploit the statistical properties of the DDSM signal. In the case of the SR, it has been proven that this architecture has an output that is provably spur free when it is distorted by a specific polynomial nonlinearity. Similarly, in Chapter 4, we have proven that MASH modulators also provide spur immunity for certain polynomial nonlinearities because of the statistical properties of the accumulated quantization error [14]. In particular, the higher the order of the MASH modulator, the higher is the order of the polynomial nonlinearity up to which the modulator is immune from spurs. However, as shown in Chapter 5, as the order of the MASH DDSM increases, so does the level of folded noise [15].

In this chapter, we present a novel family of DDSMs, called Enhanced Nonlinearity-induced nOise Performance digital $\Delta\Sigma$ modulators (ENOP-DDSMs) which, like the SR, can achieve immunity to spurs for polynomial nonlinearities of up to a certain order. The flexibility of the ENOP-DDSM architecture, underpinned by an analytical evaluation of its spurious behavior [32] and folded noise generation [15], allows one to design an ENOP-DDSM that achieves the level of spur immunity that can be achieved by the best SRs and PMRs, but with lower folded noise.

6.2 ENOP-DDSMs

6.2.1 Example

ENOP-DDSMs are characterized by being able to achieve high spur immunity while simultaneously minimizing the folded noise resulting from nonlinear distortion. An example is given in Fig. 6.1, where the simulated phase noise performance of a nonlinear fractional frequency synthesizer is compared for four different divider controller architectures, namely a MASH 1-1-1, a MASH 1-1-1-1, a second order Successive Requantizer (SR2) and an ENOP-DDSM, in the presence of a cubic nonlinearity. Note that the MASH 1-1-1 (shown in red) has a folded noise

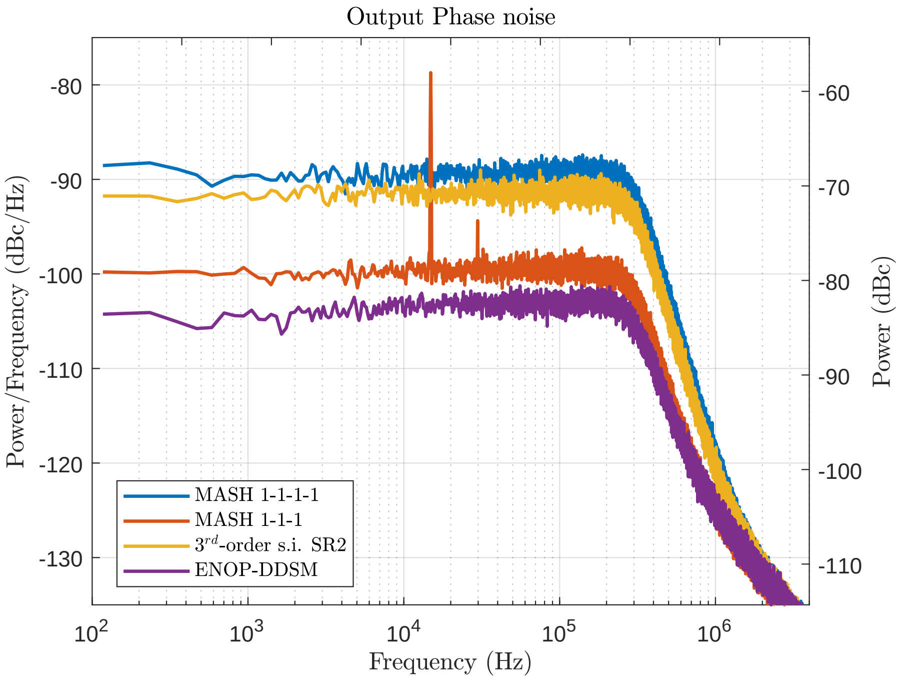

Figure 6.1: Comparison of the simulated phase noise of a fractional-N PLL for different DDSMs: MASH 1-1-1-1, 3^{rd}-order spur immune (s.i.) SR2 [43], MASH 1-1-1 and an ENOP-DDSM (P1 of Table 6.1) in the case of a third-order nonlinearity $\mathcal{N}(x) = x + 0.02x^2 + 0.01x^3$.

floor at −100 dBc/Hz and exhibits a strong fractional spur at ≈ 14.9 kHz. Many commercial fractional-N synthesizers use MASH 1-1-1 divider controllers and, therefore, exhibit spurs of this type.

The MASH 1-1-1-1 (in blue) is provably spur free for this nonlinearity and therefore does not exhibit a spur [14]. However, its folded noise floor is at −90 dBc/Hz. The SR2[1] (in yellow) is also provably spur free but it too has an elevated noise floor [43]. The ENOP-DDSM (in purple) is also provably spur free, as we will show, and its folded noise contribution at −103 dBc/Hz is the best of the four architectures.

In this example, we have shown that the ENOP-DDSM has the best noise and spur performance of the architectures considered. We will show in the following sections that an ENOP-DDSM can be designed so as to prioritize spur-immunity, to minimize folded noise or to provide a compromise between the two. This is possible because the DDSM-related noise generated by the nonlinearity can be predicted in advance once information about $e_{acc}[n]$ is known.

6.2.2 Architecture

The ENOP-DDSM can be implemented with an EFM structure, as shown in Fig. 2.1. The governing equation is

$$Y(z) = STF(z) \cdot \alpha + NTF(z) \cdot E(z), \tag{6.1}$$

where the $STF(z)$ has an absolute value equal to unity. The $NTF(z)$ of an l^{th} order ENOP-DDSM has the form:

$$NTF(z) = \left(1 - z^{-1}\right) \left(1 + \sum_{i=1}^{l-1} c_i z^{-i}\right), \tag{6.2}$$

---

[1] SR2 denotes a second order Successive Requantizer. The SR2 of this example is the one described in [43, Fig. 6 and eq. (31)].

where l represents the order of the ENOP-DDSM. According to (2.4), the desired $NTF(z)$ in (6.2) can be obtained by choosing:

$$H(z) = z^{-1} - \left(1 - z^{-1}\right) \sum_{i=1}^{l-1} c_i z^{-i}. \tag{6.3}$$

With this transfer function, the modulator will produce an accumulated quantization error whose Z-transform is equal to:

$$E_{acc}(z) = E(z) \left(1 + \sum_{i=1}^{l-1} c_i z^{-i}\right), \tag{6.4}$$

where $E(z)$ is the Z-transform of the error $e[n]$, generated by the quantizer. One can express $e_{acc}[n]$ as:

$$e_{acc}[n] = e[n] + \sum_{i=1}^{l-1} c_i e[n-i]. \tag{6.5}$$

At this point, we list the key parameters that determine the performance of an ENOP-DDSM. These are as follows:

- l: the order of the modulator.
- k: the order of low-frequency high-pass shaping of the accumulated quantization error.
- r: the half width of the range of the accumulated quantization error.
- p: the order of polynomial nonlinearities up to which the modulator is immune from spurs.
- $\sigma^2_{e_{acc}}$: the variance of the accumulated quantization error.

Some of these parameters (k, r, $\sigma^2_{e_{acc}}$) are illustrated schematically in Fig. 6.2. For the remainder of this work we will assume that every coefficient c_i in (6.2) is integer valued[2].

---

[2] This assumption is led by empirical observations which showed that integer c_i allows one to achieve optimum condition for spur immunity.

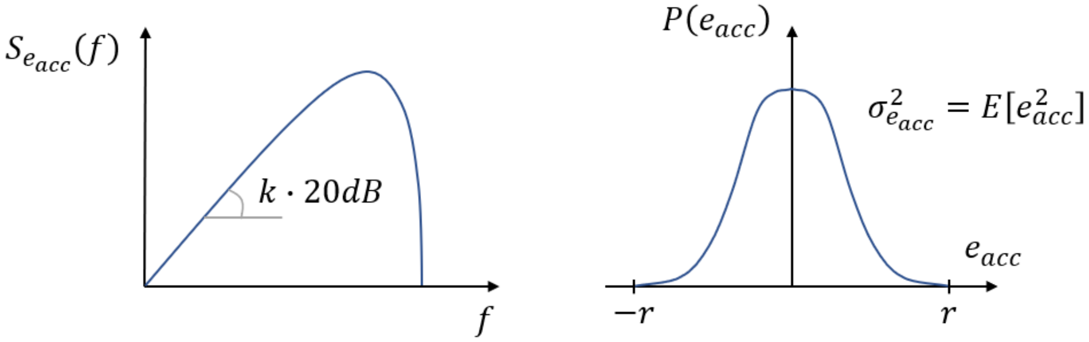

Figure 6.2: Example of PSD and pdf of e_{acc} showing the parameters k, r and $\sigma^2_{e_{acc}}$, where $E[e_{acc}] = 0$.

The order of the modulator, l, sets the number of coefficients c_i which, in turn, determine the signal e_{acc} generated by the modulator. Therefore, the value of l determines the number of degrees of freedom available when designing the ENOP-DDSM which is, in principle, $(l-1)$. The larger is l the greater is the number of delay elements (registers) that are needed to implement the block $H(z)$ in (6.3). Consequently, a larger l comes with a higher hardware cost.

As pointed out previously, it is important to high-pass shape the PSD of e_{acc} so that the low-frequency component of the modulation-related phase noise is suppressed. The order of high-pass shaping at low frequencies, k, is determined by the number of solutions of $E_{acc}(z) = 0$ at $z = 1$. As a consequence, the value of k sets constraints on the values that can be assumed by c_i. In other words, the number of degrees of freedom for designing the modulator decreases to $(l-1-k)$. This means that, for a given l, the greater is k the less room will be left for designing the modulator so that other performance characteristics can be met.

In the frequency synthesizer application, the value of k has to be greater than or equal to one. When more aggressive high-pass shaping is demanded, for example when a wide synthesizer bandwidth is required and/or a low reference frequency is employed, the choice of $k = 2$ is suitable. Higher values for k would require a more aggressive roll-off of the loop filter in the synthesizer to suppress the resulting high-frequency noise component.

6.2.3 Spur Immunity

One of the most important parameters of the ENOP-DDSM is p; this determines the level of spur immunity of the modulator. Since the modulator has to be designed such that $k \geq 1$, the coefficients c_i are chosen so that:

$$1 + \sum_{i=1}^{l-1} c_i = 0 \tag{6.6}$$

Therefore, the signal e_{acc} has a range that is symmetric about zero. In particular, we introduce the parameter r, which is the smallest positive integer such that:

$$-r < e_{acc} < r \tag{6.7}$$

Moreover, since $e[n] \in (-1, 0]^3$, from (A.4), (6.6) and the definition of r, one can show that:

$$r = \frac{1 + \sum_{i=1}^{l-1} |c_i|}{2}. \tag{6.8}$$

Familier and Galton have proven that the maximum attainable order p of spurious tone immunity for polynomial nonlinearities is $(2r - 1)$ and that there exist quantizers which are immune to spurs up to order $(2r - 1)$ [42], [67]^4. This implies that the optimal property with respect to spur immunity in the presence of a polynomial nonlinearity is given by:

$$p_{opt} = 2r - 1 \tag{6.9}$$

---

[3] This is easy to prove as $e[n]$ is the truncation error generated by the quantizer in Fig. 2.1

[4] It is worth remarking that we use a different nomenclature compared to [42], [67]. The accumulated quantization error e_{acc}, its single-sided range r and the order of spur immunity p are denoted in those works by, respectively, $t[n]$, N_t and h_t. Therefore, in that paper, the maximum value of h_t for a given N_t is expressed as $(2N_t - 1)$.

It is interesting to note that the optimal condition for spur immunity can be obtained only for *odd* values of p.

6.2.4 Folded Noise

The result in (6.9) suggests that e_{acc} must have a larger dynamic range in order to achieve spur immunity to higher order polynomial nonlinearities. However, a wider dynamic range for the accumulated quantization error would lead to stronger interaction with the nonlinearity and, qualitatively, a higher level of folded noise. The level of the noise floor can be predicted using methods such as those presented in [15], [28], [51]. For the sake of simplicity, in this chapter we consider how the severity of the generated folded noise scales with $\sigma^2_{e_{acc}}$, the variance of the accumulated quantization error. In fact, it has previously been reported that the level of the in-band folded noise floor scales qualitatively with $\sigma^2_{e_{acc}}$ [28][5]. Therefore, the value of $\sigma^2_{e_{acc}}$ provides an indication of the folded noise performance of a modulator.

If we assume that e is a uniform, independent and identically distributed (i.i.d.) stochastic process then, considering (A.4) and (6.6), the variance of e_{acc} becomes:

$$\sigma^2_{e_{acc}} = \frac{1}{12}\left(1 + \sum_{i=1}^{l-1} c_i^2\right). \tag{6.10}$$

This assumption about e is only an approximation; however, it allows one to obtain an accurate estimate of the statistical properties of e_{acc} [15]. As done also in the previous chapters, we will use this assumption when evaluating the probability distribution of e_{acc}.

Equations (6.6), (6.8) and (6.10) show that, in order to minimize the variance of e_{acc}, each non-zero integer coefficient c_i has to have an absolute value equal to

---

[5] It is important to remark that the folded noise level is not a bijective function of $\sigma^2_{e_{acc}}$. The former depends also on the spectrum of e_{acc}.

unity. This, according to the expressions (6.8) and (6.10), gives:

$$\sigma^2_{e_{acc},min} = \frac{r}{6} \tag{6.11}$$

In summary, for a given value of r, the maximum achievable order of spur immunity is equal to $(2r - 1)$. Moreover, once r is fixed, the minimum value of $\sigma^2_{e_{acc}}$ with integer coefficients is equal to $r/6$ and this is obtained when all the non-zero coefficients c_i have magnitudes equal to one. We empirically noticed that the latter condition also allows one to achieve the optimum condition for spur immunity. We do not have a rigorous proof of that yet, nor do we know if it is a necessary requirement.

Table 6.1 shows simulation results for seven sample ENOP-DDSMs[6] with $r = 2$, 3, 4 and 5. The corresponding values of $\sigma^2_{e_{acc}}$ are 1/3, 1/2, 2/3 and 5/6, respectively. We will next show that these architectures are also optimal in the sense that they achieve $p = p_{opt}$.

6.3 Analysis of spur immunity via symbolic calculation of PNN

In this section we analyze the spur immunity of the ENOP-DDSMs proposed in Table 6.1 by using the PNN. Then, we confirm the properties of spur immunity through behavioral simulations of the nonlinear frequency synthesizer. As previously presented, the PNN represents a valuable tool to determine the immunity from spurs of a given modulator. In fact, if the PNN is constant and equal to zero, the system does not experience spurs [14]. From the work presented in [32], the

---

[6] For the sake of clarity, we want to specify that we have chosen these examples of ENOP modulators empirically while assuming all non-zero coefficients c_i have magnitudes equal to one.

Table 6.1: Examples of relevant configurations of ENOP $\Delta\Sigma$ modulators

Architecture	l	k	r	p_{opt}	$NTF(z)$	$\sigma^{2*}_{e_{acc}}$	p
P1	5	1	2	3	$(1-z^{-1})\,(1-z^{-1}-z^{-2}+z^{-4})$	≈ 0.333	3
P2	6	1	3	5	$(1-z^{-1})\,(1-z^{-1}-z^{-2}+z^{-3}-z^{-4}+z^{-5})$	≈ 0.5	5
P3	7	2	3	5	$(1-z^{-1})\,(1-z^{-1}+z^{-2}-z^{-3}-z^{-4}+z^{-6})$	≈ 0.5	5
P4	8	1	4	7	$(1-z^{-1})\,(1-z^{-1}-z^{-2}+z^{-3}-z^{-4}+z^{-5}-z^{-6}+z^{-7})$	≈ 0.667	7
P5	9	2	4	7	$(1-z^{-1})\,(1-z^{-1}-z^{-2}+z^{-3}-z^{-4}+z^{-5}+z^{-7}-z^{-8})$	≈ 0.667	7
P6	10	1	5	9	$(1-z^{-1})\,(1-z^{-1}-z^{-2}+z^{-3}-z^{-4}+z^{-5}-z^{-6}+z^{-7}-z^{-8}+z^{-9})$	≈ 0.833	9
P7	11	2	5	9	$(1-z^{-1})\,(1-z^{-1}-z^{-2}+z^{-3}-z^{-4}+z^{-5}-z^{-6}+z^{-7}+z^{-8}-z^{-10})$	≈ 0.833	9

* The $\sigma^2_{e_{acc}}$ has been evaluated numerically through simulations.

PNN (defined by (2.16)) can be evaluated for a given modulator and nonlinearity once the probability distribution function of e_{acc}, denoted by $P(\cdot)$, is known. The latter can be predicted if we make the assumption that e is a uniform and i.i.d. stochastic process [68], [69] as shown in Appendix A.

We know that the hypothesis made about e is not strictly true; nevertheless, under typical conditions it leads to accurate predictions for $P(\cdot)$. For example, let us consider the case of a P1 ENOP-DDSM. Following the procedure presented in Appendix A, one can evaluate the probability distribution function of e_{acc} using (A.6), to obtain:

$$P(x) = \begin{cases} \frac{1}{6}\left(4 - 6x^2 + 3|x|^3\right) & \text{if } 0 \le |x| \le 1 \\ \frac{1}{6}\left(2 - |x|\right)^3 & \text{if } 1 \le |x| \le 2 \\ 0 & \text{elsewhere} \end{cases} \tag{6.12}$$

The predicted probability distribution is compared to simulation results in Fig. 6.3. Notice that the simulated distribution $P(e_{acc})$ closely matches the analytical prediction. This confirms the validity of the approximation made about e_{acc}. The predictions of $P(e_{acc})$ for the other architectures of ENOP-DDSMs presented in Table 6.1 are provided in Appendix F.

Equation (6.12) allows one to evaluate the PNN for the P1 architecture once the nonlinearity is specified. In particular, let us consider the case of P1 interacting with a generic third order polynomial nonlinearity, expressed as $\mathcal{N}(x) = \sum_{i=0}^{3} a_i x^i$. From the definitions in (2.14)–(2.16), (4.4) and considering the expression of the predicted $P(\cdot)$ (6.12), one can show that:

$$PNN[n] = a_0 + a_1\tau_{os} + a_2\left(\frac{1}{3} + \tau_{os}^2\right) + a_3\left(\tau_{os} + \tau_{os}^3\right), \tag{6.13}$$

which is independent of n and is therefore constant. Moreover, because of the locking condition of a type-II PLL, τ_{os} is valued so that $E\left[PNN\left[n\right]\right] = 0$.

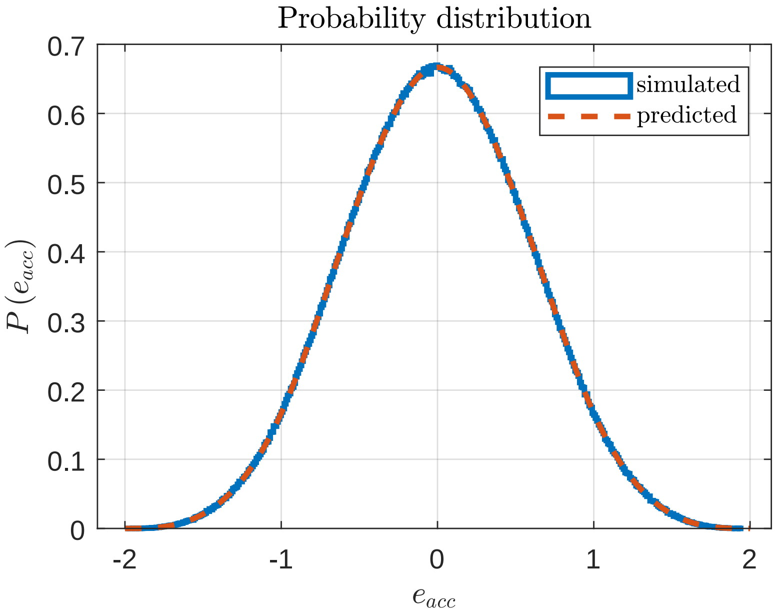

Figure 6.3: Predicted and simulated probability distribution of e_{acc} in the case of P1 ENOP-DDSM; $r = 2$.

Therefore, the PNN expressed in (6.13) is equal to zero, which means that the system does not experience fractional spurs in the case of polynomial nonlinearities up to the third order[7] when a P1 ENOP-DDSM is used. This confirms that the level of spur immunity p for the P1 ENOP-DDSM equals the optimal value $p_{opt} = 5$ shown in Table 6.1. Repeating a similar PNN analysis for the other proposed architectures yields the characteristics of spur immunity listed in Table 6.1, as shown in Appendix F. In each case, the P1–P7 ENOP-DDSMs achieve a level of spur immunity equal to p_{opt} and are optimal in the sense of Familier and Galton [67].

---

[7] Eq. (6.13) shows that the P1 ENOP-DDSM is immune from spurs in the case of third order nonlinearity. However, it is easy to notice that, in the case of polynomial nonlinearities with order lower than three, one or more coefficients a_i in (6.13) would be equal to zero, leading to a PNN which is still independent of n. Therefore, we can say that the immunity holds *up to* third order.

Concluding, the architectures listed in Table 6.1 match the condition of best spur immunity and the lowest folded noise. In fact, they are both p-optimal and exhibit minimal $\sigma^2_{e_{acc}}$.

6.4 Validation by behavioral simulation of PLL

In this section we validate the performance of representative ENOP-DDSMs in the frequency synthesizer application through behavioral simulations of a nonlinear charge pump (CP) PLL where the divider controller is implemented with the NTFs listed in Table 6.1. The simulations were performed using the closed-loop phase domain model described in section 2.4. The parameters of the simulated system are listed in Table 2.1. First-order shaped LSB dither is applied to the modulator to ensure that the quantization error is sufficiently randomized [25], while an odd value for the input X is chosen to mitigate against possible horn spurs [13][8].

6.4.1 Third-order Polynomial

We first consider the case where the synthesizer exhibits a third-order polynomial nonlinearity. The results of the simulations are shown in Fig. 6.4. With a MASH 1-1-1 DDSM, a fixed integer boundary spur would be expected at $\frac{X}{M} f_{ref} \approx 14.9$ kHz. From Table 6.1, all ENOP-DDSMs are expected to provide spur immunity in the presence of third-order nonlinearities. This is confirmed by the simulations. Note that no spurs are present in any of the ENOP-DDSMs.

It is worth noticing also that the level of folded noise increases from P1 to P7. This is to be expected, since $\sigma^2_{e_{acc}}$ increases as well. In fact, as discussed in

---

[8] Together, the odd input and shaped LSB dither are sufficient to make e_{acc} approximately uniform and i.i.d..

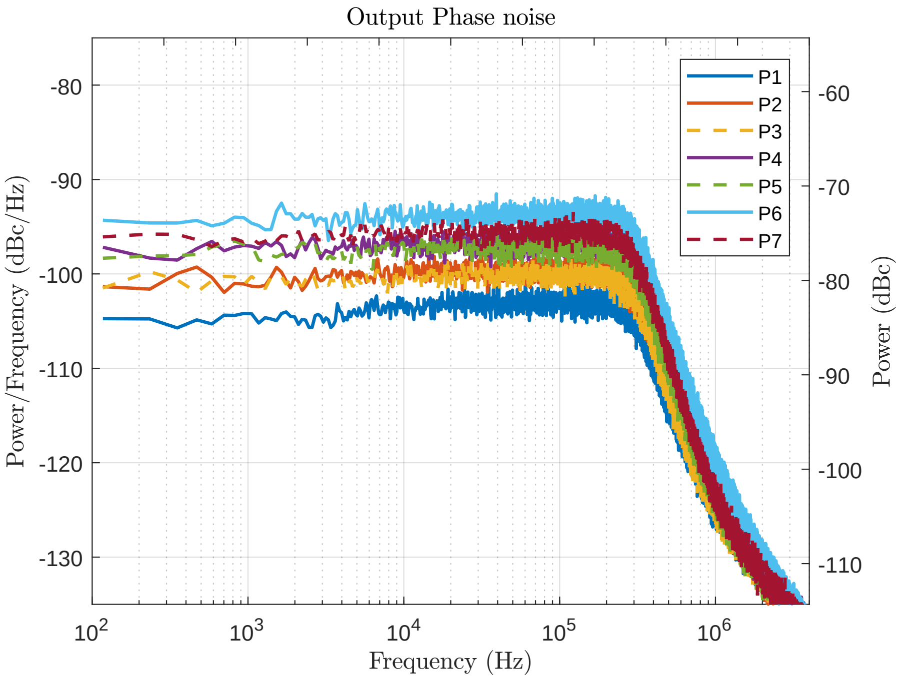

Figure 6.4: Simulated phase noise in the case of cubic nonlinearity ($\mathcal{N}(x) = x + 0.02x^2 + 0.01x^3$) for the different ENOP-DDSMs.

Section 6.2, the folded noise floor scales with $\sigma^2_{e_{acc}}$. Therefore, we expect that two different modulators that share the same value of $\sigma^2_{e_{acc}}$ should generate similar levels of folded noise. Moreover, the latter increases as $\sigma^2_{e_{acc}}$ gets bigger. This is confirmed in Fig. 6.4, where P1, which has $\sigma^2_{e_{acc}} = 1/3$, contributes the lowest excess noise, while P6 and P7, which have $\sigma^2_{e_{acc}} = 5/6$, have the highest.

6.4.2 Fifth-order Polynomial

Next, we consider the case where the nonlinearity is a fifth-order polynomial. From the analysis in Section 6.2, we predict spurious tones for the P1 ENOP-DDSM and spur immunity in the other cases. This is confirmed by the simulation results in Fig. 6.5. In particular, note the integer boundary spur at ≈ 14.9 kHz in Fig. 6.5. Similar considerations to the previous case can be made for the folded noise: P1 is the best while P6 and P7 are the worst.

6.4.3 Ninth-order Polynomial

Lastly, we consider the case of a ninth-order polynomial nonlinearity. This example confirms that P6 and P7 ENOP-DDSMs are spur immune up to ninth-order polynomial nonlinearities. This is shown in Fig. 6.6. Notice that the cases of P1, P2 and P3 exhibit spurs since their p is less than 9. Note also that the level of the folded noise grows as the variance of e_{acc} increases.

It should be clear at this point that the ENOP-DDSMs can provide different trade-offs between the order of spur rejection and the in-band noise floor, depending on the choice of NTF. Empirically, the higher is the level of the spur immunity, the larger will be the folded noise. It follows that, depending on the performance one wishes to prioritize, one NTF might suit an application better than the others.

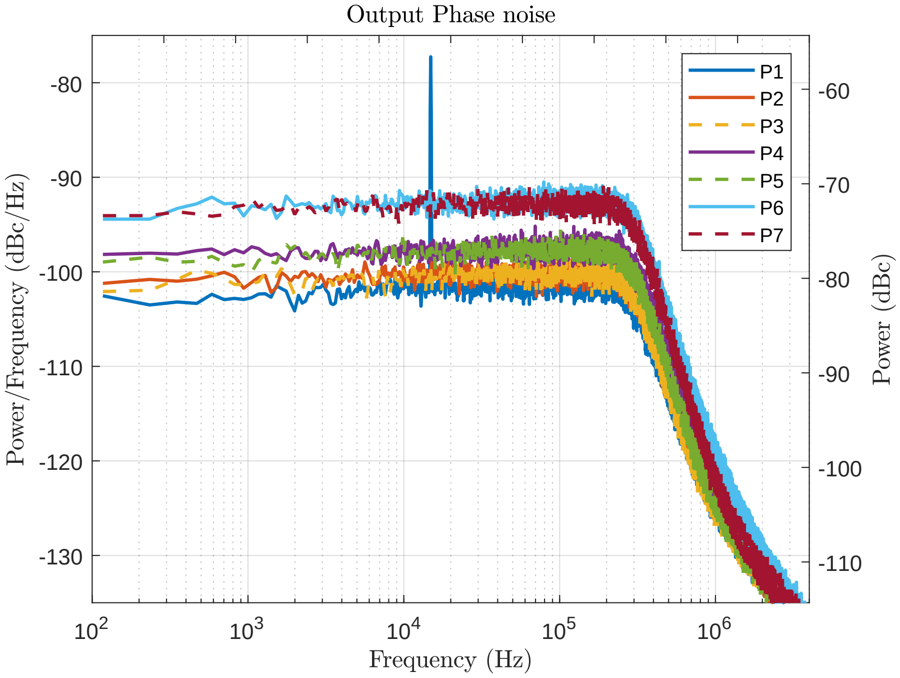

Figure 6.5: Simulated phase noise in the case of third-order nonlinearity ($\mathcal{N}(x) = x + 0.04x^2 + 0.03x^3 - 0.01x^4 - 0.005x^5$) for the different ENOP-DDSMs.

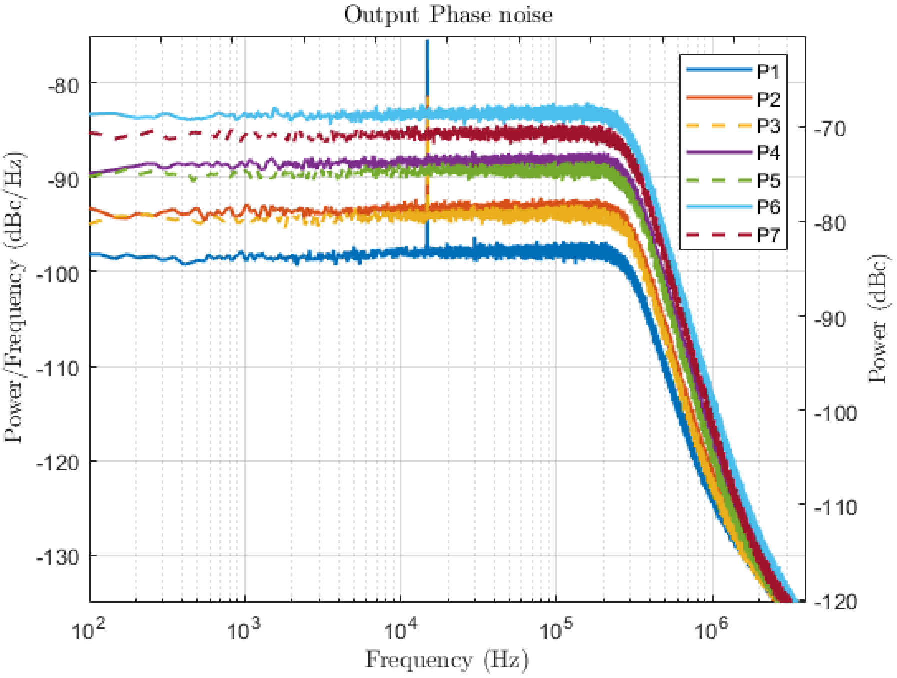

Figure 6.6: Simulated phase noise in the case of ninth-order nonlinearity ($\mathcal{N}(x) = x + 0.04x^2 + 0.03x^3 - 0.003x^4 - 0.002x^5 + 0.002x^6 - 0.001x^7 - 10^{-4}x^8 + 4 \cdot 10^{-5}x^9$) for the different ENOP-DDSMs.

6.5 Wandering and Horn Spurs performance

In the previous sections we have discussed the performance of ENOP DDSMs regarding fractional spurs. In particular, we have shown that ENOP DDSMs are capable of achieving immunity from fractional spurs in the case of high-order polynomial nonlinearities with a low level of folded noise [16]. However, as have mentioned in Chapter 1, in addition to fractional spurs, wandering spurs and horn spurs are also worthy of mention. The former consists of sets of spurs that change their positions in frequency periodically with time. Horn spurs, by contrast, are fixed spurs, whose positions can be sub-fractional ($< \alpha \cdot f_{ref}$) i.e. they can fall *inside* the PLL bandwidth even if α is far from an integer value. These two phenomena have been discussed extensively in the case where the divider controller is implemented by a conventional MASH 1-1-1 [9], [10], [11], [13]. In this section, we will assess the behavior of ENOP-DDSMs regarding both wandering and horn spurs.

We compare simulation results for a type-II charge pump (CP) PLL as described in Section 2.4 with different modulators as the divider controller. The simulations are performed in MATLAB with a closed loop phase domain model [20]. The simulation parameters of the loop are listed in Table 2.1, except for the value of f_{ref} which is considered here to be 20 MHz[9]. We consider the idealized case where the CP exhibits a mismatch, e_{CP}, between the up and down currents. Therefore, the system experiences a piece-wise linear (PWL) nonlinearity in the PFD/CP block. In order to study the effects of the nonlinearity on the output phase noise in isolation, we do not consider any source of reference/detector noise in the simulated model.

In the following simulations we compare the resulting PLL output phase noise

---

[9] This value for f_{ref} is assumed in order to make the following simulation results easier to compare with the ones in [9] and [10].

when considering a conventional MASH 1-1-1 and an ENOP P1 as the divider controller. The latter can be implemented with an EFM structure with the NTF provided in Table 6.1. Further details on the possible implementations of ENOP DDSMs will be given in the next chapter.

In [9] and [10], the authors have distinguished three cases of wandering spurs according to the value of the input, X with respect to the modulus, M, of the modulator. In particular, in order to discern the different cases of wandering spurs, it is useful to write the input X as:

$$X = \frac{cM + g}{D} = \frac{cM}{D} + X', \tag{6.14}$$

where c, D and g are integers and c and D are both non-negative and coprime. We investigate each case of wandering spurs separately. Then, the horn spurs will also be evaluated.

6.5.1 Wandering Spurs in Case I

According to the analysis in [9], the first case of wandering spurs is experienced when $c = 0$, i.e. the input X has a small value. In particular, we refer to the case of $X = 3$ considered in [9, Fig. 9]. The results for both a MASH 1-1-1 and an ENOP P1 are shown in Fig. 6.7. The initial conditions of the two modulators, namely $s_i[0]$, are set equal to zero[10]. One should notice that, while wandering spurs are generated in the case of a MASH 1-1-1, these are not exhibited by the synthesizer when an ENOP P1 is used to implement the divider controller.

---

[10] For the sake of completeness, the initial condition represents the value of the signal $s[n]$ shown in Fig. 2.1, for $n = 0$.

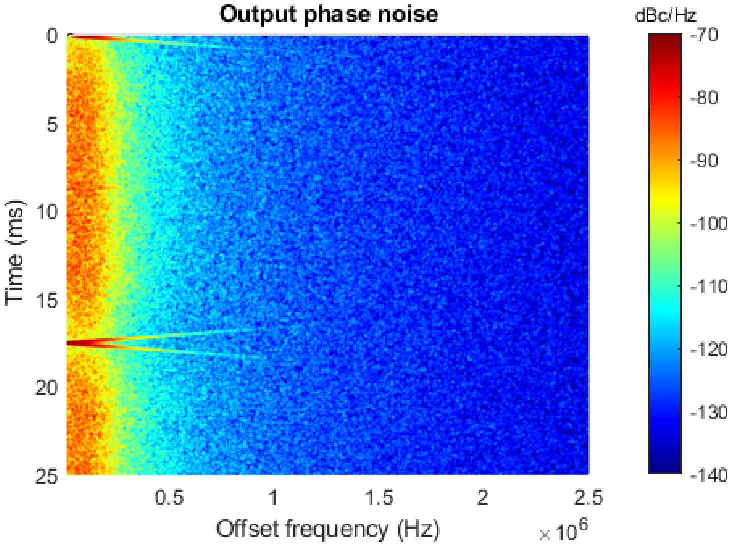

(a)

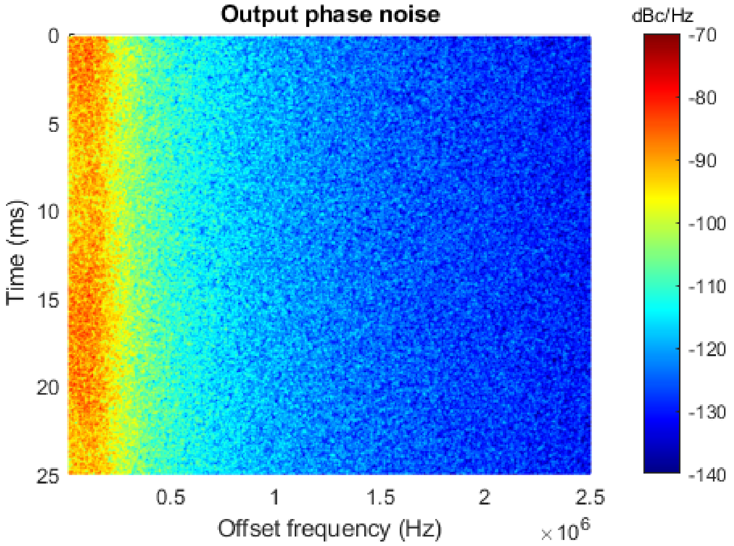

(b)

Figure 6.7: Simulated output phase noise spectrograms in the cases of (a) a MASH 1-1-1 and (b) an ENOP P1 for wandering spurs in case I: $X = 3$, $M = 2^{20}$, $s_1[0] = 0$. First-order shaped LSB dither is applied to each case.

6.5.2 Wandering Spurs in Case II

The second case of wandering spurs analyzed in [9], occurs when $c > 0$ and $g \neq 0$, which means that X is close to but not equal to a big fraction of M. As an example of case II wandering spurs, we consider the example presented in [9, Fig. 13], where X is chosen to be equal to $\lfloor M/6 + 1 \rceil$. The same condition has been reproduced in Fig. 6.8. Similarly to the previous case, the ENOP P1 does not exhibit wandering spurs, while the MASH 1-1-1 does.

6.5.3 Wandering Spurs in Case III

The last case of wandering spurs is experienced when $c > 0$ and $g = 0$ [9]. This has been further analyzed in [10], where it is shown that the properties of the third type of wandering spurs depend on the value of the modulator's initial condition, $s_1[0]$. Let us consider the case shown in [10, Fig. 5], where $X = M/4$ and $s_1[0] = \lfloor M/3 + 1 \rceil$. Under these conditions, the resulting spectrograms for both a MASH 1-1-1 and an ENOP P1 are given in Fig. 6.9. It is clear from the figures that the ENOP P1 does not exhibit wandering spurs in this case either. It is worth noticing that, in addition to the wandering spurs, Fig. 6.9(a) also shows a fixed spur at ≈ 0.83 MHz. This latter can be shown to be a horn spur by following the analysis in Chapter 3. The absence of such a spur in Fig. 6.9(b) anticipates the result that is given in the next subsection.

6.5.4 Horn Spurs

According to the analysis in Chapter 3 and referring to the expression in (6.14), horn spurs are experienced under the same conditions of Sec. 6.5.3, i.e. for $c > 0$ and $g = 0$. These spurs are fixed in frequency and their positions depend on $s_1[0]$ but not on c. This means that horn spurs can appear at low frequencies, even

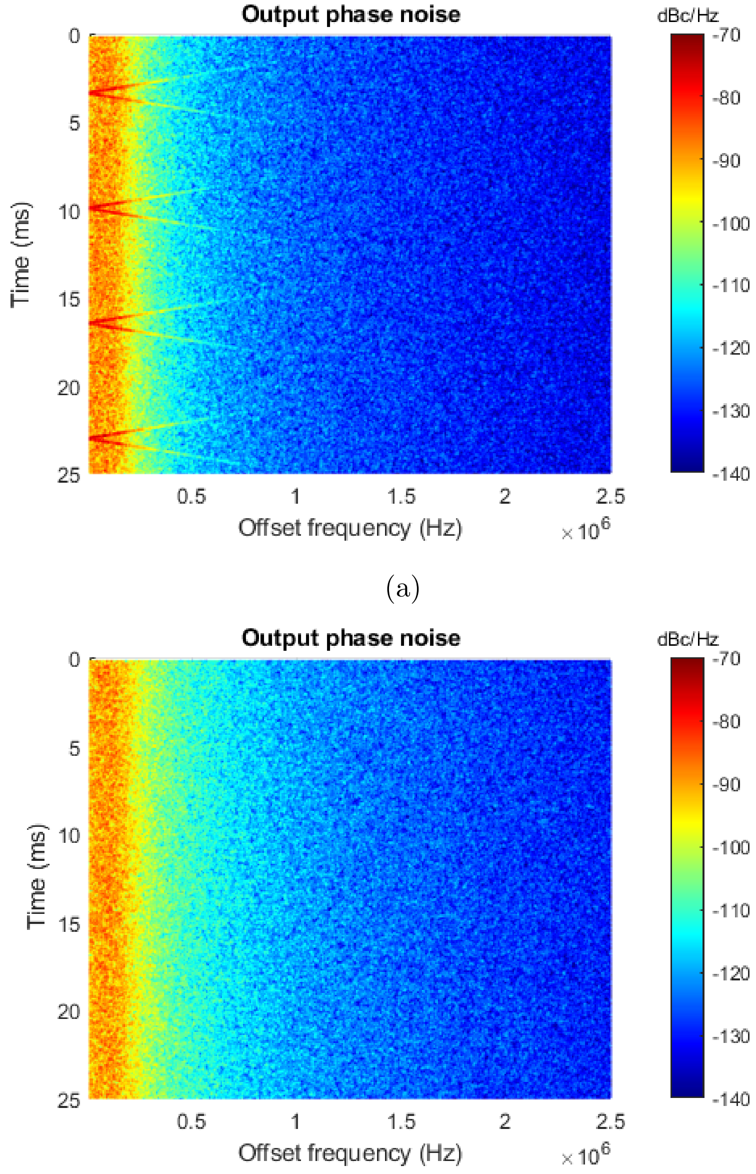

(a)

(b)

Figure 6.8: Simulated output phase noise spectrograms in the cases of (a) a MASH 1-1-1 and (b) an ENOP P1 for wandering spurs in case II: $X = \lfloor M/6+1 \rceil$, $M = 2^{20}$, $s_1[0] = 0$. First-order shaped LSB dither is applied to each case.

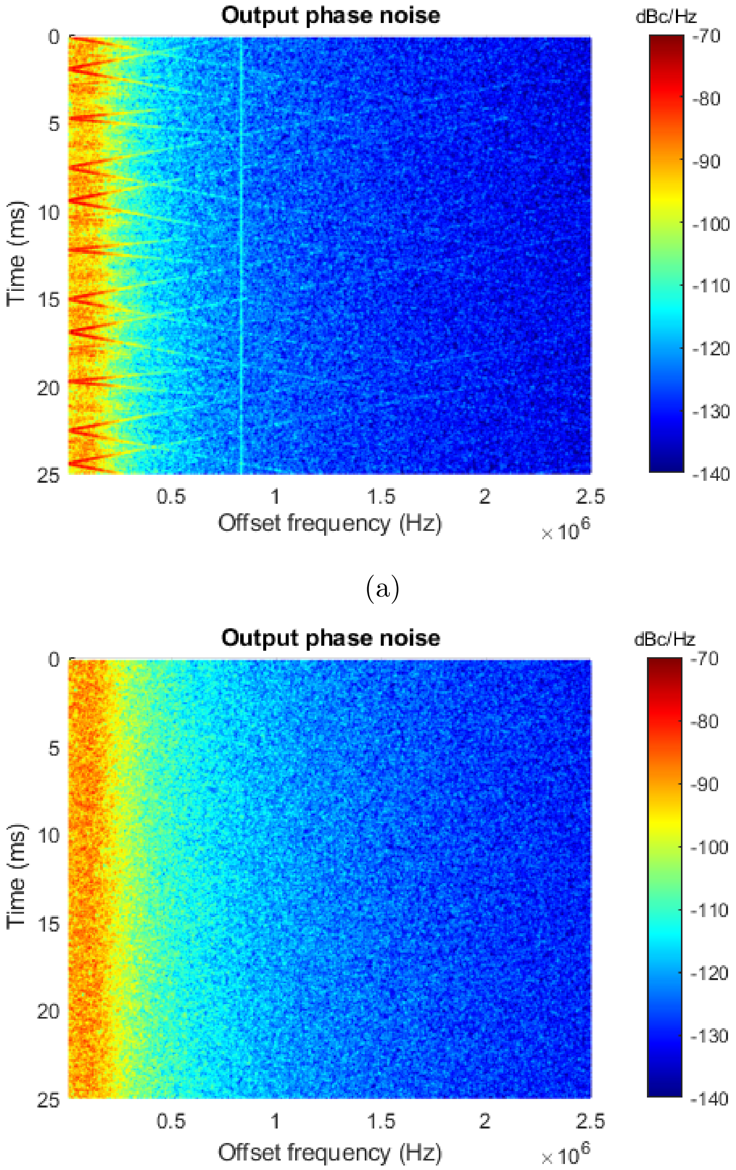

(a)

(b)

Figure 6.9: Simulated output phase noise spectrograms in the cases of (a) a MASH 1-1-1 and (b) an ENOP P1 for wandering spurs in case III: $X = M/4$, $M = 2^{20}$, $s_1[0] = \lfloor M/3 + 1 \rceil$. First-order shaped LSB dither is applied to each case.

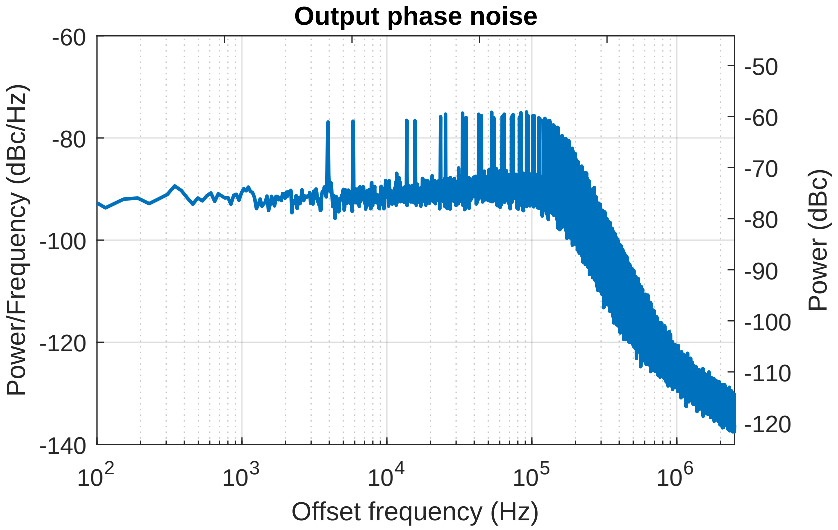

(a)

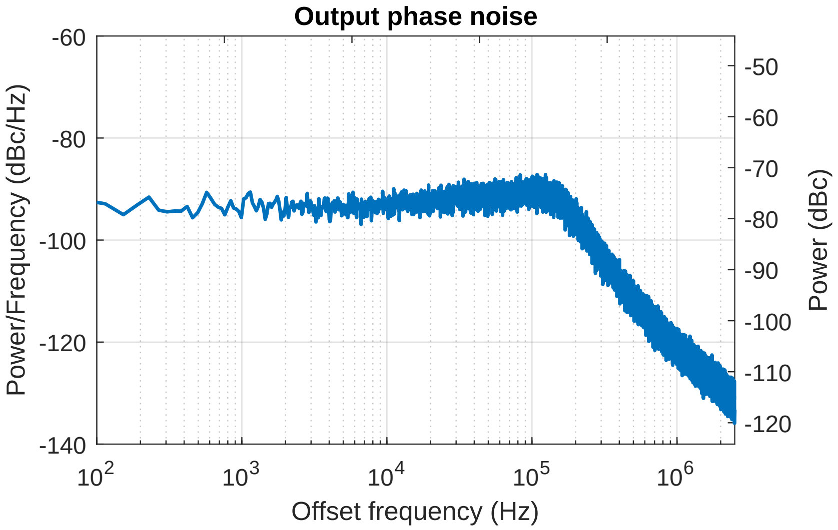

(b)

Figure 6.10: Simulated output phase noise in the case of (a) a MASH 1-1-1 and (b) an ENOP P1. Input $X = 321M/2^{11}$, $M = 2^{20}$ and $s_1[0] = 50$. First-order shaped LSB dither is applied to each case.

though c is large and α is far from an integer. This is the case of the example shown in Fig. 6.10, where $X = 321M/2^{11}$. For this value of X, the fractional spur at αf_{ref} is far outside the PLL bandwidth, while many pairs of horn spurs populate the phase noise plot in Fig. 6.10(a). Under the same conditions, these tones are absent in Fig. 6.10(b), confirming that the ENOP P1 does not exhibit horn spurs. The spur performance of the MASH 1-1-1 and the ENOP P1 are summarized in Table 6.2, which shows that the ENOP solution provides better performance for all three types of spurs. For the sake of brevity, we will not go through the same analysis for the other architectures of ENOP DDSMs listed in Table 6.1. However, if one does it, similar results will be obtained.

Table 6.2: Performance Summary

DDSM	MASH 1-1-1	ENOP P1
Fractional Spurs	Immune to quadratic nonlinearity [14]	Immune to cubic nonlinearity [16]
Wandering Spurs	Y	N
Horn Spurs	Y	N

Even though we do not have a rigorous explanation for the mitigation of wandering and horn spurs in ENOP DDSMs, this outcome can be explained qualitatively. Let us remember that both wandering and horn spurs have been noticed to be generated by the excitement of inner periodicities inside the modulator [9], [10], [13]. Then, the generic governing equation (6.2), and the practical solutions of NTFs listed in Table 6.1 suggest that the truncation error $e[n]$ and the related e_{acc} are sufficiently well randomized not to experience the periodic behaviors that lead to the generation of wandering and horn spurs.

6.6 Comparison with previous art

In this chapter we have presented a new architecture of DDSMs that aims to improve the performance of frac-N PLLs in terms of nonlinearity-induced noise, with particular emphasis on fractional spurs. At the beginning of this dissertation we have cited and referred to previous authors' work on this subject. In this regard, it is necessary to spend a few words on a more detailed comparison with the prior art in [33] and [67].

In these works, the authors have presented an architecture of quantizers, called Successive Requantizers, that have a similar purpose to that of ENOP modulators. Both aim to improve the spur performance of frac-N PLLs by making the modulator's error immune to spurious tones up to a certain order of polynomial nonlinearities. Even though the two architectures share the same target, the approaches are quite different. The properties of Successive Requantizers are based on the design of quantization stages whose functioning is defined by pairs of transition matrices which can be proven mathematically to provide a quantization error that has a moment of a certain order which is independent of the quantizer's input[11]. The latter allows one to obtain spur immunity in the case of polynomial nonlinearities up to that order.

On the other hand, the ENOP DDSMs only provide empirical observations of the aforementioned spur immunity performance. A pseudo-analytical approach has been used to provide an intuitive explanation of the properties of spur immunity for the ENOP modulators. In particular, the PNN is used which is analyzed with the probability distribution of e_{acc} that is predicted while making the assumption of uniform i.i.d. distribution for $e[n]$. As remarked multiple times

---

[11] For the sake of brevity, we will not dwell on the details of the theory behind the Successive Requantizers. The reader who is interested in learning more about it is referred to the works [33], [42], [43], [45] and [67].

in this thesis, the latter is only an approximation. As a consequence, the spur immunity performance of ENOP modulators are not rigorously proven, unlike in the case of Successive Requantizers. This represents the first substantial difference between the two architectures.

In terms of performance, the SRs and ENOP DDSMs show comparable results for spur immunity. Both architectures experience nonlinearity-induced folded noise. We cannot draw a line on which one performs better in terms of folded noise. However, we experienced that ENOP modulators tend to show lower noise as in the case of the example presented in Fig. 6.1. For the sake of completeness, Successive Requantizers are characterized by a fairly intricate functioning which requires complicated combinatorial logic blocks and makes these solutions quite expensive in terms of design effort and hardware cost. On the other hand, the governing equation of ENOP modulators is easier to implement and results in lower hardware complexity. This will be explored further in the next chapter.

6.7 Comments on linear noise contribution

Throughout this chapter, we have analyzed and praised the outstanding performance of ENOP DDSMs towards the nonlinearity-induced noise in the form of either spurious toned or elevated in-band folded noise. However, for the sake of completeness, a few words need to be spent on the linear noise contribution of these modulators.

In fact, whether the synthesizer is linear or nonlinear, the modulation of the division ratio introduces an error in the loop which is proportional to e_{acc}. As discussed in Section 2.2, we want the PSD of e_{acc}, denoted by $S_{e_{acc}}(f)$, to be high pass shaped. The latter can be considered as the linear noise contribution of the modulator. In fact, it represents the modulator-induced noise if the system were linear. Even though the PSD $S_{e_{acc}}(f)$ of an ENOP DDSM is high-pass shaped, it has a different spectral profile than a conventional MASH. In particular, differently from MASH modulators, one can notice that the NTFs listed in Table 6.1 do not have all the zeroes equal to 1. As a consequence, an ENOP DDSM with the same order, k, of low-frequency high-pass shaping of e_{acc} as a MASH DDSM, will have a worse linear noise contribution in general. An example is shown in Fig. 6.11, where the PSD of e_{acc} is compared for the cases of ENOPs P3, P5 and a conventional MASH 1-1-1. One can notice that, even though the three

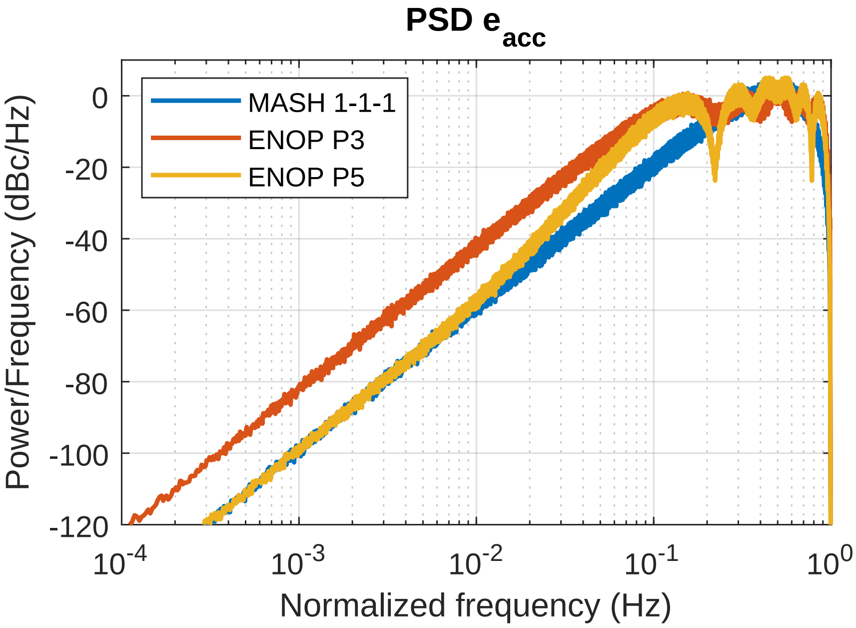

Figure 6.11: Comparison of the simulated PSD of e_{acc} in the case of a MASH 1-1-1, an ENOP P3 and an ENOP P5 modulators.

modulators have the same low-frequency shaping order for e_{acc} ($k = 2$), they have different linear noise components that will contribute differently to the overall output phase noise of the synthesizer. It is clear that the MASH 1-1-1 provides the best (lowest) linear noise contribution among the three, while the noise of the ENOP P3 is the worst.

Depending on the value of f_{ref}, the bandwidth of the synthesizer and the other sources of noise of the system, the linear noise component of the modulator can be dominant and degrade the overall jitter performance of the PLL. For this reason, even though the ENOP DDSMs provide provably improved nonlinearity-induced noise performances, one should pay attention to the spectrum of the resulting accumulated quantization error.

6.8 Summary

In this chapter, we have presented a family of $\Delta\Sigma$ modulators that can be designed to be optimal in the sense of Familier and Galton in terms of spurious tone immunity for polynomial nonlinearities, while minimizing the folded noise. The level of spur immunity has been predicted analytically and confirmed by simulation. The results show the potential of ENOP-DDSMs to match the state of the art performance in terms of spur immunity. Moreover, with the same level of spur immunity, ENOP DDSMs outperform the prior-art in terms of folded noise. The behavior of ENOP DDSMs has been also tested in the case of wandering and horn spurs, showing a strong rejection of both.

Chapter 7

Implementation of ENOP and Hybrid Nested ENOP DDSMs

In the previous chapter we presented a novel family of DDSMs which allow one to obtain Enhanced Nonlinearity-induced nOise Performance (ENOP). We have shown that the characteristics of each architecture of ENOP modulator are defined by its NTF. However, the same NTF can be implemented in more than one way. For this reason, in this chapter we discuss hardware implementations of ENOP DDSMs. Furthermore, we also present hybrid ENOP configurations and implementations thereof.

7.1 Implementation of ENOP-DDSMs

The ENOP-DDSMs presented and analyzed in Chapter 6 are characterized and distinguished merely by their NTFs. Indeed, their properties hold independently of how the modulator is implemented in hardware, as long as the resulting NTF remains the same. This means that ENOP-DDSMs can be implemented in a variety of ways. In this section, we focus on three possible architectures, namely: single-quantizer (SQ), cascaded and nested cascaded (NC) structures. Moreover, in order to illustrate how an ENOP-DDSM is implemented in a particular architecture, we will focus on the P3 ENOP-DDSM for the remainder of the chapter [70]. Its noise transfer function is:

$$NTF(z) = \left(1 - z^{-1}\right)\left(1 - z^{-1} + z^{-2} - z^{-3} - z^{-4} + z^{-6}\right). \qquad (7.1)$$

7.1.1 Single-Quantizer structure

The first, most intuitive solution is to realize an ENOP-DDSM with a single-quantizer structure, like the one shown in Fig. 2.1. In order to do so, the transfer function $H(z)$ has to be designed such that the resulting NTF is in the form of:

$$NTF(z) = \left(1 - z^{-1}\right)\left(1 + \sum_{i=1}^{l-1} c_i z^{-i}\right). \qquad (7.2)$$

Therefore, from (7.2), one obtains:

$$H(z) = z^{-1} - \left(1 - z^{-1}\right)\sum_{i=1}^{l-1} c_i z^{-i}. \qquad (7.3)$$

In the case of the P3 ENOP-DDSM, $H(z)$ becomes:

$$H(z) = 2z^{-1} - 2z^{-2} + 2z^{-3} - z^{-5} - z^{-6} + z^{-7}. \qquad (7.4)$$

This means that a six-addend adder and seven delay steps (registers) are required to implement $H(z)$ for a P3 ENOP-DDSM using a SQ-DDSM structure. This is shown in Fig. 7.1.

7.1.2 Cascaded MASH structure

An alternative to the SQ implementation is a cascaded MASH structure. In order to understand how this implementation is obtained, we note that k was defined

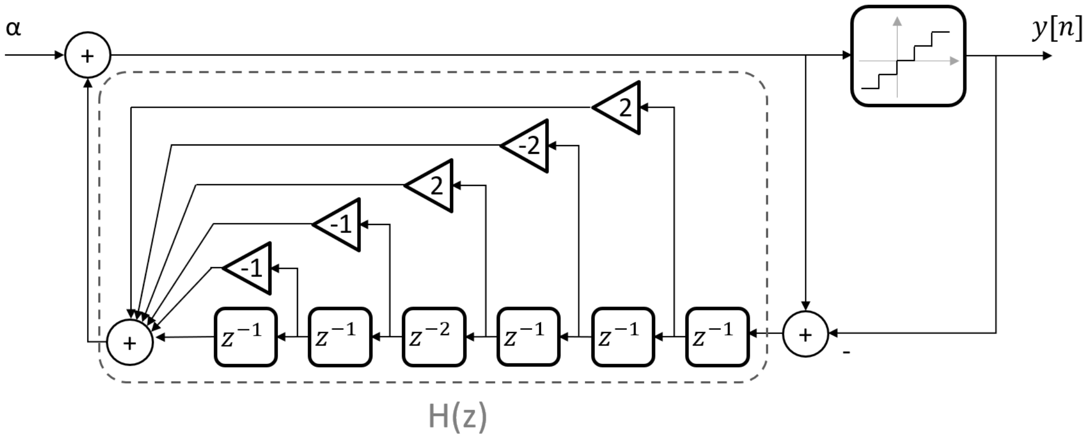

Figure 7.1: Block diagram of the P3 ENOP-DDSM implemented with a SQ structure.

in Section 6.2.2 as the order of low-frequency high-pass shaping of $e_{acc}[n]$. In other words, k is determined by the number of solutions of $E_{acc}(z) = 0$ at $z = 1$. Therefore, the noise transfer function of an ENOP-DDSM has $k + 1$ zeroes at 1. This means that the NTF can be expressed as:

$$NTF(z) = \left(1 - z^{-1}\right)^{(k+1)} \left(1 + \sum_{i=1}^{l-k-1} \hat{c}_i z^{-i}\right). \tag{7.5}$$

It can be shown that the noise transfer function in (7.5) can be realized with a cascaded structure, similar to that of a MASH DDSM. In this case, the ENOP-DDSM is implemented by a set of j cascaded EFM1s[1] followed by an appropriately designed $(l - j)$th order EFM, where $j \in [1, k + 1]$. Similarly to a conventional MASH modulator, the output of each stage is fed to an error cancellation network that generates the output $y[n]$. This architecture is depicted in Fig. 7.2. It is worth mentioning that the cascaded structure has an advantage for randomizing the modulation error by mean of dithering. In particular, high-pass shaped

---

[1] With EFM1 we mean a first-order error feedback modulator (EFM) like the one in Fig. 2.1, where $H(z) = z^{-1}$.

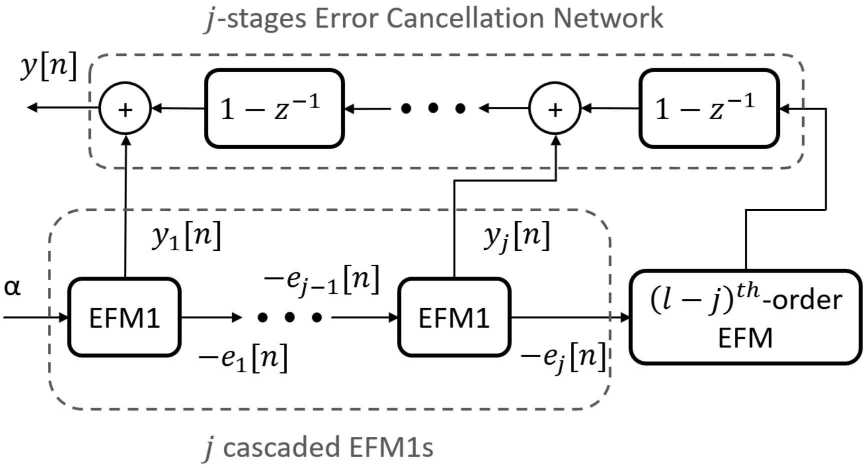

Figure 7.2: Block diagram of an ENOP-DDSM implemented with a cascaded structure.

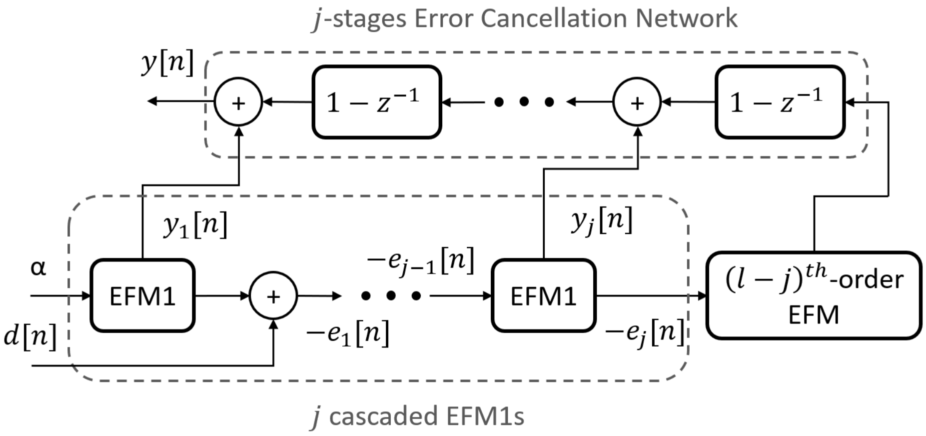

Figure 7.3: Block diagram of the ENOP cascaded implementation of Fig. 7.2 with additional first-order filtered LSB dither.

dithers are typically preferred since their accumulation will not introduce a DC offset or degrade the low frequency phase noise performance of the system [25]. That being said, first order shaped dither is easily implemented in a cascaded structured ENOP modulator by adding the unfiltered LSB dither signal to the input of the second stage, as shown in Fig. 7.3.

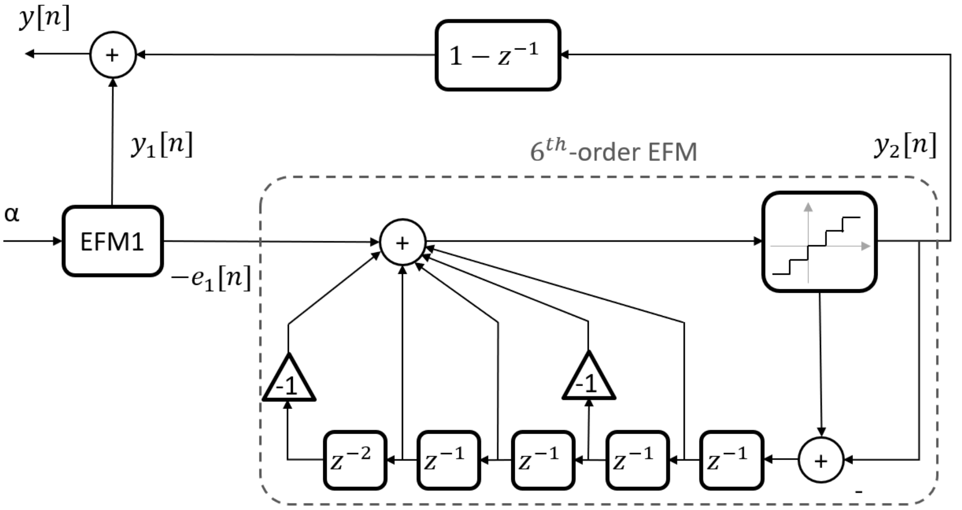

Figure 7.4: Block diagrams of the P3 ENOP-DDSM implemented with a cascaded structure and $j = 1$.

One should notice that, according to the cascaded structure described above, the last stage must have a noise transfer function equal to:

$$NTF_{(j+1)}(z) = \frac{NTF(z)}{(1 - z^{-1})^j}, \tag{7.6}$$

which, because of (7.5), simplifies into a linear combination of powers of z, and hence it can also be realized as an EFM.

In the case of a P3 ENOP-DDSM, k is equal to 2 [70]. Therefore, there are three possible cascaded configurations, respectively, for j equal to 1, 2 and 3. For $j = 1$, the modulator is implemented with two stages. The first one is an EFM1, while the second stage must have a noise transfer function equal to $(1 - z^{-1} + z^{-2} - z^{-3} - z^{-4} + z^{-6})$, as determined by (7.1). Then, the latter can be designed as the EFM in Fig. 2.1, with $H(z) = z^{-1} - z^{-2} + z^{-3} + z^{-4} - z^{-6}$. This configuration is shown in Fig. 7.4. In order to explain the other two configurations, note that the NTF of a P3 ENOP-DDSM, given in (7.1), can be equivalently written as:

$$NTF(z) = \left(1 - z^{-1}\right)^2 \left(1 + z^{-2} - z^{-4} - z^{-5}\right) \tag{7.7}$$

$$= \left(1 - z^{-1}\right)^3 \left(1 + z^{-1} + 2z^{-2} + 2z^{-3} + z^{-4}\right). \tag{7.8}$$

Therefore, a P3 ENOP-DDSM could be either implemented with the cascade of two EFM1s and an EFM with $H(z) = -z^{-2} + z^{-4} + z^{-5}$, or three EFM1s followed by an EFM with $H(z) = -z^{-1} - 2z^{-2} - 2z^{-3} - z^{-4}$. These two variants are depicted in Figs. 7.5(a) and 7.5(b). Of the different implementations of a P3 ENOP-DDSM presented so far, the cascaded one with $j = 2$ provides the lowest hardware cost, as shown in Table 7.1. Moreover, this choice also relaxes the timing constraints in the modulator, as the last stage has to deal with a less complex addition.

Table 7.1: Hardware cost of the different variants of an N-bit P3 ENOP-DDSM implemented with a cascaded structure.

Variants	Hardware cost of the EFM1(s)	Hardware cost of the last stage*	Total hardware cost**
$j = 1$ (Fig. 7.4)	1 N-bit adder	$\approx$ 5 N-bit adders	$\approx$ 6 N-bit adders
	1 N-bit register	6 N-bit registers	$\approx$ 7 N-bit registers
$j = 2$ (Fig. 7.5(a))	2 N-bit adder	$\approx$ 3 N-bit adders	$\approx$ 5 N-bit adders
	2 N-bit register	5 N-bit registers	$\approx$ 7 N-bit registers
$j = 3$ (Fig. 7.5(b))	3 N-bit adder	$\approx$ 4 N-bit adders	$\approx$ 7 N-bit adders
	3 N-bit register	4 N-bit registers	$\approx$ 7 N-bit registers

*We neglect that some of the adders would need more than N bits to not overflow.

**We neglect the hardware cost of the error cancellation network since it is quite small compared to that of the overall modulator.

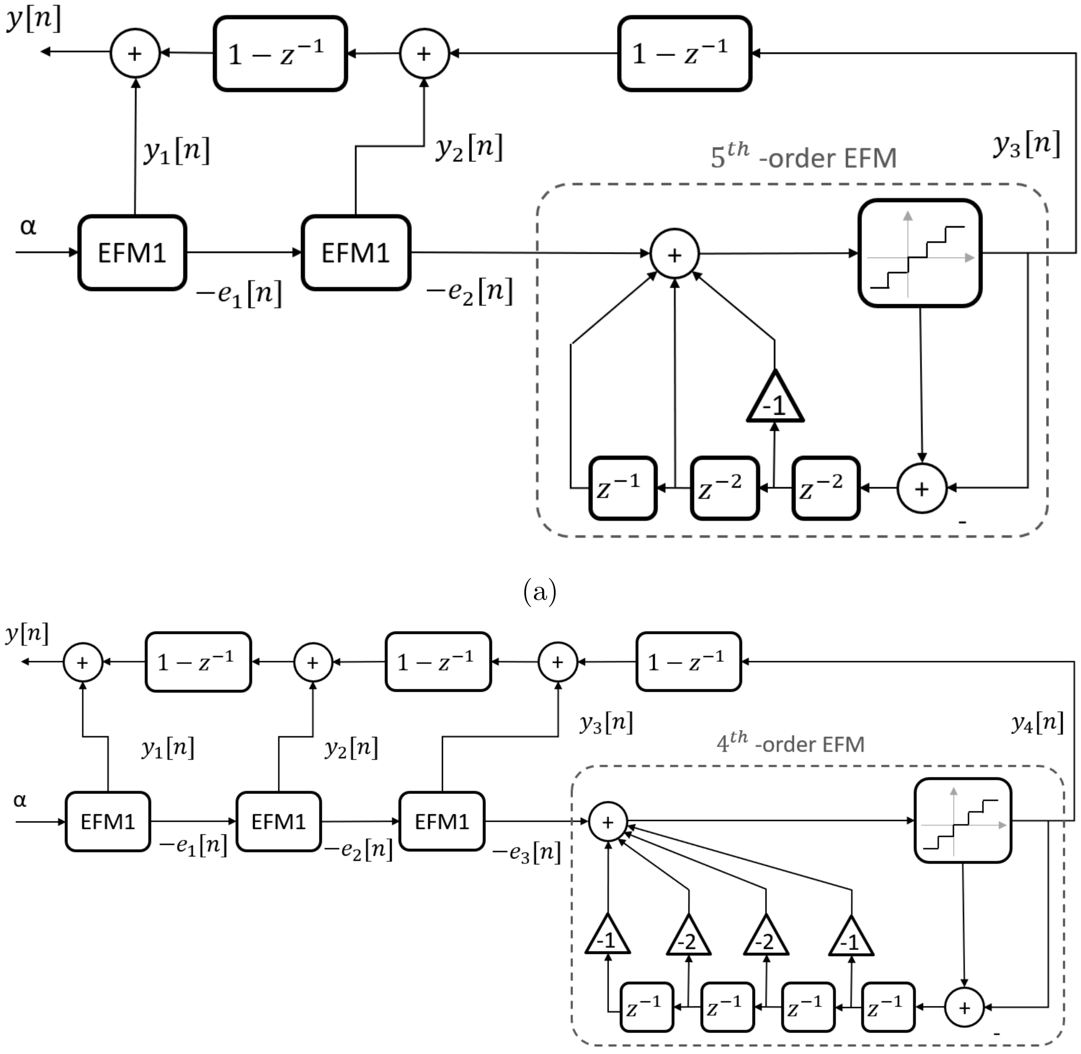

Figure 7.5: Block diagrams of the P3 ENOP-DDSM implemented with a cascaded structure and (a) $j = 2$, (b) $j = 3$.

7.1.3 Nested Cascaded structure

The concept of nested cascaded digital $\Delta\Sigma$ modulators has been used for implementing high-speed MASH modulators [71]. In the previous subsection we showed that, similarly to MASH modulators, ENOP-DDSMs are also suitable for cascaded implementation. Consequently, ENOP-DDSMs can also be implemented with a nested cascaded structure. For the sake of simplicity, let us consider the two-level structure shown in Fig. 7.6. The input word α, represented by N bits, is split into α_A and α_B which are, respectively, the N_A MSBs and the N_B LSBs of α. These two signals are fed to two sets of j cascaded EFM1 stages, each one followed by an $(l-j)$th order EFM, which is designed as discussed in the previous subsection. Every EFM in the two levels is characterized by having moduli M_A and M_B that are equal to, respectively, 2^{N_A} and 2^{N_B}. Moreover, the output of each second-level i-th stage, $y_{B,i}[n]$, is added to the input of the i-th stage of the first level. Then the outputs of the first-level stages are combined in an error cancellation network to generate the output signal, $y[n]$.

Let us consider the example of a P3 ENOP DDSM implemented with a nested

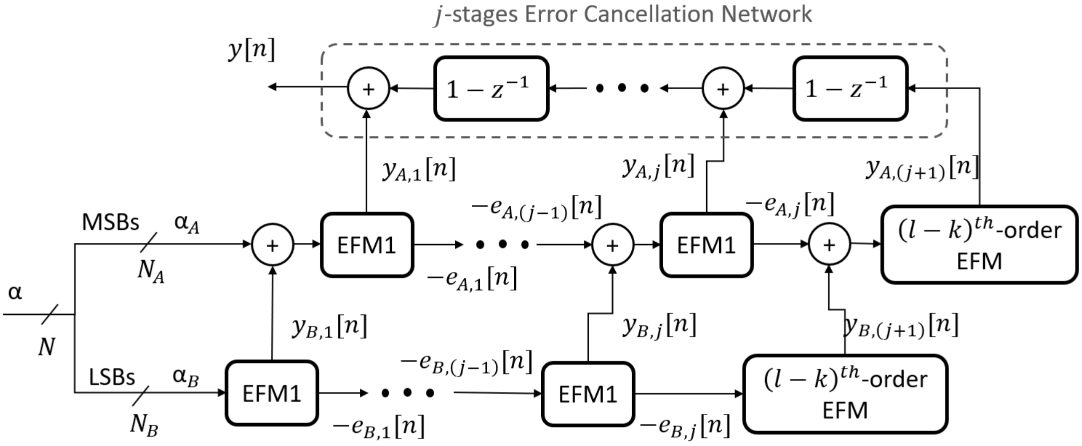

Figure 7.6: Block diagram of an ENOP-DDSM implemented with a nested cascaded two-levels structure.

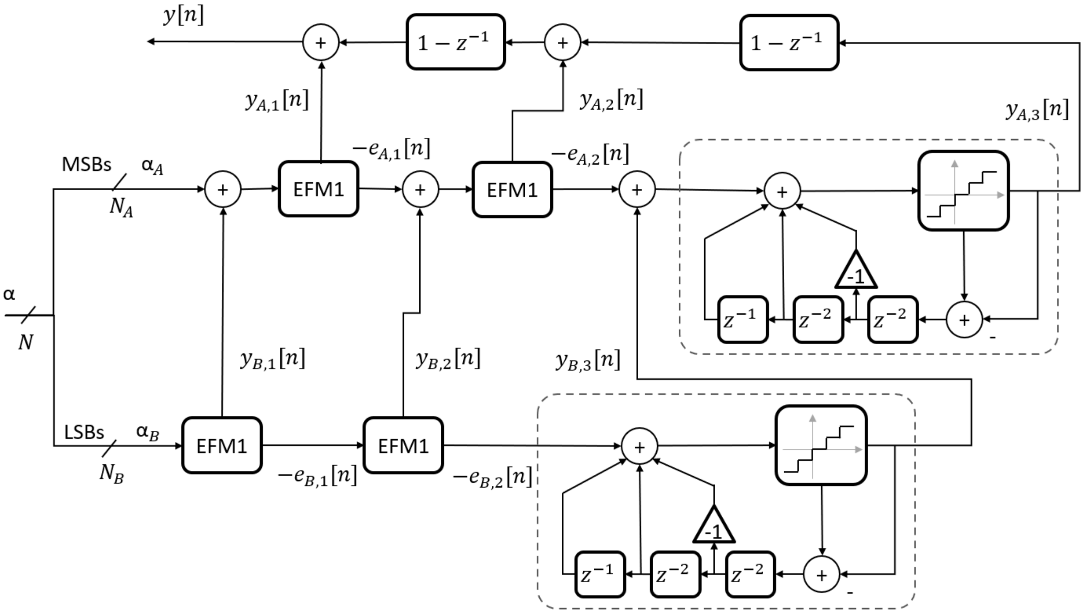

Figure 7.7: Block diagram of the P3 ENOP-DDSM implemented with a two-level nested cascaded structure with $j = 2$.

cascaded structure. At first, one needs to choose the number of cascaded stages. We suggest a three-stage structure ($j = 2$) since, as discussed previously and shown in Table 7.1, as it represents the least expensive solution in terms of hardware. Then, the input word has to be split in order to feed the levels that comprise the NC structure. The diagram of the three-stage P3 ENOP-DDSM implemented with a two-level NC structure is shown in Fig. 7.7. It is worth mentioning that the structure can be extended over more than two levels. In conclusion, NC-ENOP modulators provide the same noise performance as the configurations in Sections 7.1.1 and 7.1.2, while allowing higher-speed operation at the cost of an increased area[2].

---

[2] The estimation on the increase of speed has been obtained from the transposition of the concepts in [71] and the results provided in [71, Fig. 5] to the ENOP modulator with particular emphasis on the last stage. In fact, it should be clear to the reader that the overall speed of the ENOP modulator is limited by the additions that take place in the last stage.

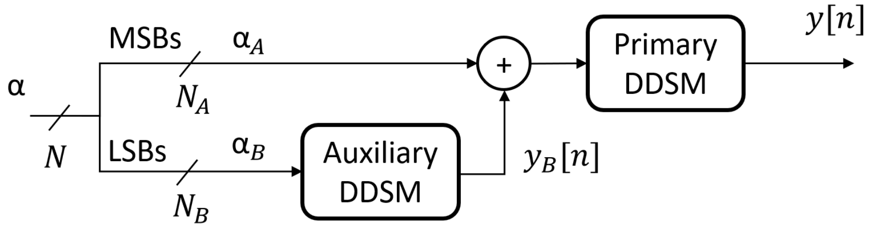

Figure 7.8: Block diagram of a generic hybrid nested DDSM.

7.2 Implementation of Hybrid Nested ENOP-DDSMs

Another possible implementation is a hybrid nested ENOP-DDSM. The concept of hybrid nested structures has already been discussed in previous works [72]. Similarly to what we described in Section 7.1.3, the input to the divider controller, α, is separated into two parts via bus splitting. We denote these by α_A and α_B. The latter is fed to an auxiliary DDSM, which outputs a signal $y_B[n]$ that is added to α_A to produce the input signal of the primary modulator. The latter, in turn, produces the signal $y[n]$ that controls the MMD. The structure of a generic hybrid nested DDSM is shown in Fig. 7.8.

7.2.1 Hybrid Nested structure

In the case of a hybrid nested ENOP-DDSM, we choose an ENOP modulator as the primary one, while the auxiliary can be implemented by a MASH DDSM or other architectures with low hardware cost. In this way, one can have a compromise between the nonlinearity-induced noise performance of an ENOP modulator and a lower area and power consumption compared to the structures presented in Section 7.1. Further details are given in the following. It is worth noting that the expression given in (2.2) is still valid. However, the Z-transform of the quantization error $e_q[n]$ is expressed in this case as[3]:

$$E_q(z) = NTF_A(z)E_A(z) + \frac{NTF_B(z)E_B(z)}{M_A}, \tag{7.9}$$

where $NTF_A(z)$ and $NTF_B(z)$ are the noise transfer functions of the ENOP and auxiliary modulators, respectively; $E_A(z)$ and $E_B(z)$ are the Z-transforms of the errors $e_A[n]$ and $e_B[n]$ introduced by the ENOP and auxiliary modulators, respectively; while M_A is the modulus of the ENOP DDSM. The result in (7.9) shows that the overall quantization error and its related phase noise are functions of the quantization errors of both the ENOP and auxiliary modulators. Moreover, it is desirable that the two DDSMs should be designed so as to achieve error masking [73], [74]. This means that the noise term associated with the auxiliary modulator should not exceed that of the primary modulator. In order to achieve this, $NTF_B(z)$ is chosen to have low-frequency high-pass shaping with order equal to that of $NTF_A(z)$. In other words, $NTF_A(z)$ and $NTF_B(z)$ should have the same number of zeroes at $z = 1$.

7.2.2 Hybrid Nested Cascaded structure

In Sections 7.1.2 and 7.1.3, we have shown that ENOP-DDSMs map in a straightforward way to cascaded and nested cascaded structures, as well as MASH modulators [71]. That being so, it is possible to implement a hybrid nested MASH-ENOP modulator that is configured in a cascaded structure. The idea is to use a structure similar to that in Fig. 7.6, where the first level is associated with a primary ENOP modulator, while the second level is related to an auxiliary MASH DDSM. In this case, the primary and auxiliary modulators share the error cancellation network. Moreover, because of the error masking considerations,

---

[3] We are assuming that both the primary and auxiliary modulators have envelopes of their signal transfer functions (STFs) that are equal to 1.

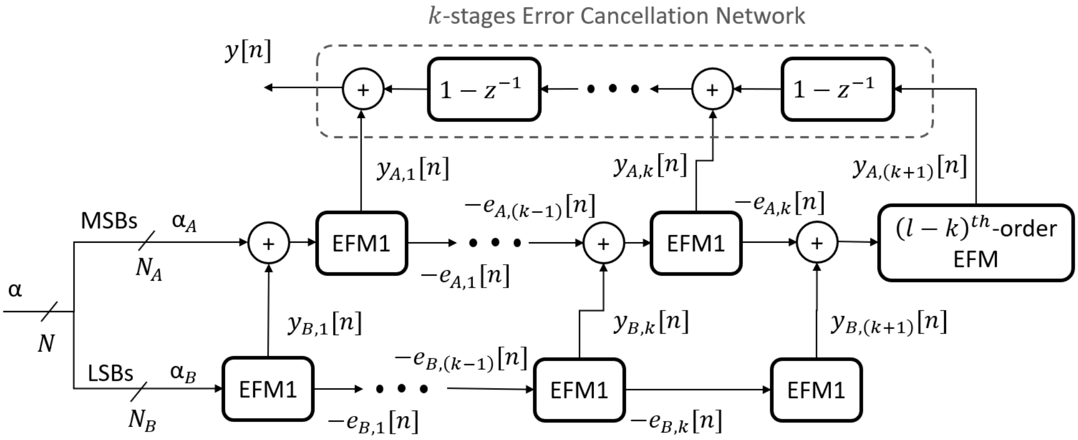

Figure 7.9: Block diagram of a hybrid nested cascaded MASH-ENOP DDSM.

we choose that both $NTF_A(z)$ and $NTF_B(z)$ have $(k+1)$ zeroes for $z = 1$. Therefore, a suitable auxiliary MASH-DDSM has $NTF_B(z) = (1-z^{-1})^{(k+1)}$. The aforementioned requirements are satisfied by choosing a second level composed of $(k+1)$ cascaded EFM1s, while the first level is a cascade of k EFM1s followed by an EFM with the noise transfer function equal to $NTF_A(z)/(1-z^{-1})^k$. This structure is shown in Fig. 7.9. As mentioned in Section 7.1.3, the choice of an NC structure allows one to improve the operating speed but with a greater hardware cost. Obviously, this structure can be further refined by implementing either or both primary and auxiliary modulators on more than one level.

7.2.3 Example of Hybrid Nested ENOP-DDSM

Let us consider the case of a hybrid nested modulator based on the P3 ENOP-DDSM. This means that the primary noise transfer function $NTF_A(z)$ is equal to (7.1) and has three zeroes for $z = 1$. In this case, the MASH 1-1-1 is a suitable choice for the auxiliary modulator in terms of error masking. Independently of the selection of a nested or nested cascaded structure, a hybrid ENOP-DDSM requires bus splitting. Therefore, the partition of N_{int} in the values of N_A and N_B has to be selected. This will determine the noise performance of the hybrid modulator. In fact, the larger is the number of bits assigned to the primary ENOP modulator the better is the resistance of the hybrid DDSM to polynomial nonlinearity-induced spurs[4]. However, increasing N_A and, consequently, decreasing N_B leads to a higher hardware cost.

Consider the distorted accumulated quantization error in the case of a fifth-order polynomial nonlinearity:

$$\mathcal{N}(x) = x + 0.04x^2 + 0.03x^3 - 0.01x^4 - 0.005x^5, \tag{7.10}$$

for different modulators, regular and hybrid nested cascaded. In particular, we focus on the hybrid (MASH 1-1-1)-(P3 ENOP) DDSM and compare it with both the standard MASH 1-1-1 and P3 ENOP modulators[5]. The results of the simulated PSDs are shown in Fig. 7.10. Note that the 20-bit MASH 1-1-1 suffers from a low-frequency noise floor and strong fractional spurs. Selecting a hybrid MASH-ENOP with only 1 bit for the primary modulator makes a big difference in terms of spur performance compared to a MASH 1-1-1. Moreover, the hybrid modulator provides lower folded noise but a higher linear noise, $S_{e_{acc}}(f)$, at high frequencies. The latter is typically not a problem, since the modulation noise is low-pass filtered by the system's transfer function. That being said, a small spur is still visible in the case of the hybrid modulator with $N_A = 1$. Therefore, we move to the case of $N_A = 2$ which does not show any visible spur. Moreover, as highlighted in Fig. 7.10, the hybrid MASH-ENOP with $N_A = 2$ provides no visible difference in noise performance when compared to a P3 ENOP.

In the previous chapter, it has been shown that the properties of spur rejection of ENOP DDSMs are determined by the probability distribution of e_{acc}, denoted

---

[4] Up to fifth-order polynomials for the case of the P3 ENOP configuration [70].

[5] When it comes to the noise performance, it does not matter how the regular P3 ENOP DDSM is implemented.

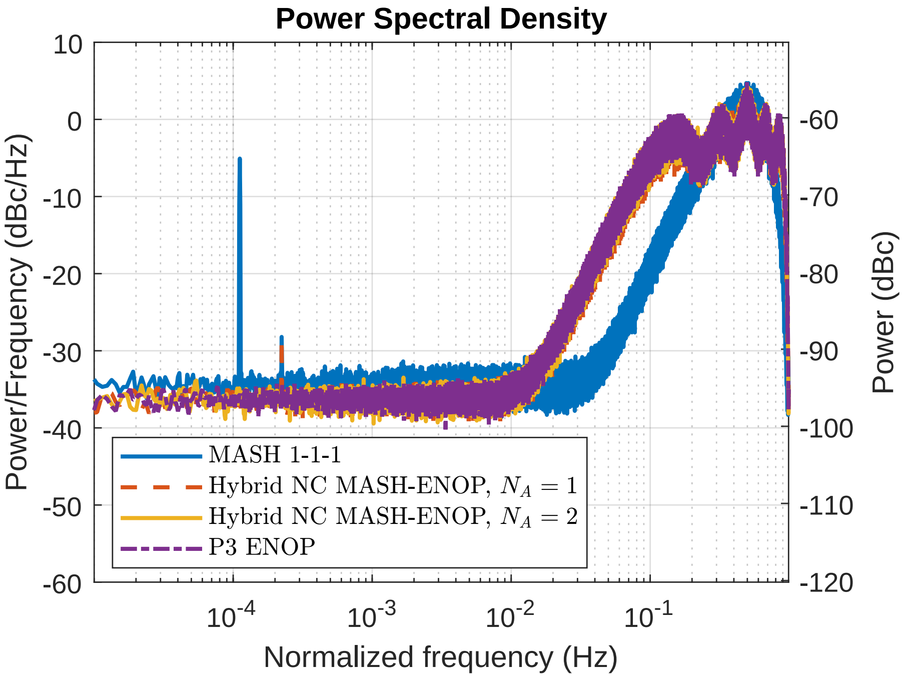

Figure 7.10: Simulated PSD of the nonlinear accumulated quantization error distorted by the fifth order polynomial nonlinearity in (7.10), for different DDSMs with $\alpha = 117/2^{20}$ and $N = 20$.

by $P(e_{acc})$ [70]. Then, the behavior of $P(e_{acc})$ in hybrid ENOP modulators can explain the good spur performance experienced in Fig. 7.10. In fact, looking at

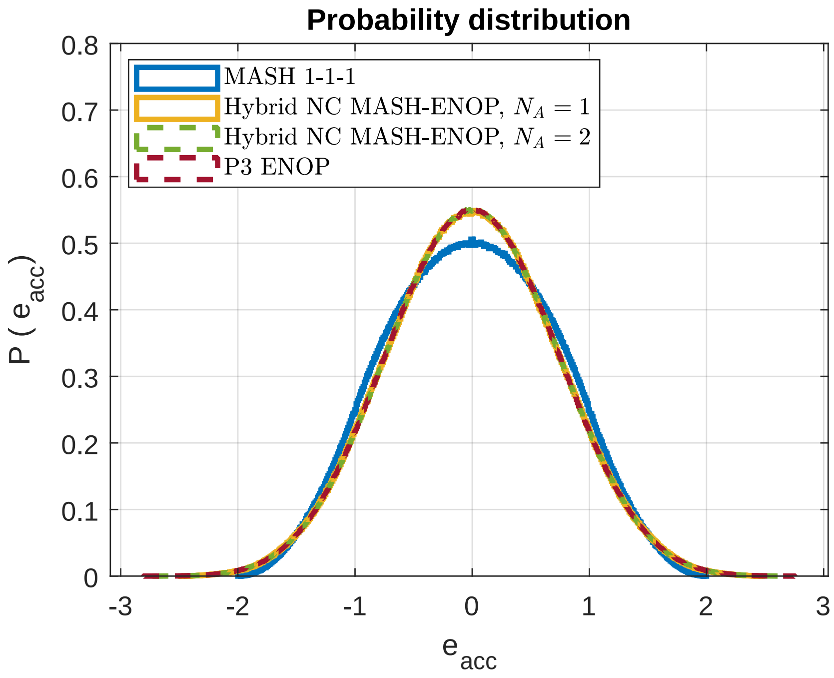

Figure 7.11: Simulated probability distribution function (pdf) of the linear accumulated quantization error for different DDSMs with $\alpha = 117/2^{20}$ and $N = 20$.

the simulated results shown in Fig. 7.11, notice that the hybrid ENOP modulators provide a $P(e_{acc})$ that approximates very closely that of the P3 ENOP-DDSM. This result suggests that hybrid nested ENOP-DDSMs may represent appealing solutions since they provide almost identical noise performance to an ENOP modulator, but at a significantly lower hardware cost. More details will be given in the following section.

7.3 Performance Comparison

In the previous sections we have discussed several solutions for implementing both an ENOP DDSM and a hybrid nested version. The pros and cons of each structure have been analyzed qualitatively. In this section, we provide a quantitative performance comparison of the most relevant modulator architectures presented so far. In particular, we focus on the solutions obtained while implementing the P3 ENOP DDSM with different structures. The comparison considers hardware cost and operating speed. These parameters are compared to those of a standard MASH 1-1-1. Moreover, the performance analysis is carried out setting the number of bits $N = 20$. Details on the calculation of these parameters are provided in Appendix G. The results of the comparison are listed in Table 7.2.

As it was clear from the beginning, the P3 ENOP DDSM comes with a quite complex NTF compared to that of a MASH 1-1-1. Therefore, the hardware cost of a P3 ENOP modulator is expected to be greater than that of a standard MASH 1-1-1. This is outlined in Table 7.2, where the three non-hybrid solutions require approximately twice the hardware of a MASH 1-1-1. In detail, the SQ solution represents the simplest and most intuitive implementation. However, it strongly affects the operating speed which decreases to almost a third of that of a MASH 1-1-1. This is due to the fact that the single loop has to accommodate all the combinatorial logic which, in turn, leads to a higher delay. Better performance is obtained by using a cascaded implementation with $j = 2$, previously seen in Fig. 7.5(a). As anticipated in Section 7.1.2, this solution saves some hardware in terms of adders. More interestingly, the cascaded solution allows the modulator to redistribute the combinational effort over more than one stage. This improves the operating speed that slightly exceeds a half that of the MASH 1-1-1. In order to push the operating speed even higher, the nested cascaded solution can be chosen. In particular, we have analyzed the case of an NC P3 ENOP DDSM

Table 7.2: Hardware cost and operating speed normalized to that of a MASH 1-1-1 DDSM with $N = 20$.

DDSM	Hardware cost		Operating speed
	Flip-flops	Adders	
MASH 1-1-1	100%	100%	100%
SQ P3 ENOP	222%	195%	34%
Cascaded P3 ENOP ($j = 2$)	232%	166%	53%
Two-level NC P3 ENOP ($j = 2$, $N_A = 10$)	233%	180%	73%
Hybrid two-level NC MASH-ENOP ($N_A = 2$)	119%	112%	109%

with only 2 levels and splitting α into two equally long words. This latter choice allows one to optimize the speed improvement [71]. Then, the operating speed increases to 73% that of the MASH 1-1-1, at a cost of a slightly higher use of hardware when compared to the cascaded solution.

A different scenario is represented by the choice of a hybrid nested implementation. In fact, hybrid solutions offer a tradeoff between the noise performance, speed and hardware cost. In particular, this compromise is weighted by the choice of how many bits are allocated to the primary and the auxiliary modulator. As discussed in Section 7.2.3, because of the properties of the P3 ENOP DDSM, we proposed a hybrid NC (MASH 1-1-1)-(P3 ENOP) modulator. Moreover, it has been shown that the choice of $N_A = 2$ returns a noise performance that does not show visible differences to that of a non-hybrid P3 ENOP DDSM in the case of a fifth order polynomial nonlinearity (7.10). This does not mean that the hybrid version has the same spur immunity performance as the non-hybrid ENOP, but it still provides spur rejection. Furthermore, compared to the previous solutions, the hardware cost and operating speed are markedly improved. In particular, the hardware requirement is only 12–19% greater than that of the MASH 1-1-1, while the operating speed is even faster than that of the MASH 1-1-1.

7.4 Summary

In this chapter, we have presented different hardware implementations for the family of ENOP DDSMs. The advantages and tradeoffs of each structure have been analyzed. The possibility of hybrid nested configurations has also been investigated. Moreover, a practical example of how to implement either an ENOP or hybrid MASH-ENOP modulator has been provided.

Chapter 8

DDSMs with Immunity from Nonlinearity-Induced Spurs (INIS)

In this chapter we present another family of novel DDSMs that, similarly to the ENOP modulators, does not produce spurs when distorted by a polynomial nonlinearity. In particular, these new modulators generate a quantization error that is immune to spurs independently of the static nonlinearity that is encountered by the modulator's output.

8.1 Introduction

Digital $\Delta\Sigma$ modulators (DDSM) are commonly used in modern systems such as DCOs and audio/video processing blocks for implementing the operation of *requantization.* This involves the reduction of the word length of digital data. It is typically required in order to meet some circuit specification or constraint. Let us think of a DDSM application in a digitally controlled oscillator (DCO). The

DCO generates a signal with a frequency that can be discretely tuned by means of a digitally switched capacitor array. The resolution of the tuning frequency is determined by the finest capacitance among the capacitors. This, in turn, is limited by the CMOS technology. In order to push the granularity of the synthesizable frequency beyond the resolution set by the capacitors, a DDSM can be employed to control the DCO [75], [76].

The operation of requantization allows one to reduce the number of quantization levels of a digital signal without a significant loss of information. However, a quantization error, e_q, is generated and effectively added to the output signal. Similarly to what has been discussed on e_{acc} in Sec. 2.2, a proper design of the modulator requires e_q to be adequately randomized and spectrally shaped. Unfortunately, nonlinearities in the signal chain after the DDSM will interact with the quantization error and typically generate additional spurious tones and folded noise.

In previous works, a class of modulators, called Successive Requantizers (SRs), has been presented [33]. They were demonstrated to achieve high rejection of nonlinearity-induced spurs at the cost of a greater hardware complexity compared to a traditional DDSM [42], [67]. In others, techniques such as dynamic element matching (DEM) have been developed for mitigating the noise effect induced by the nonlinearity [75], [76]. In this chapter, we present a novel family of DDSMs that provides immunity from nonlinearity-induced spurs (INIS-DDSMs) independently of the static nonlinearity.

8.2 Background

Much information on DDSMs was is already given in Section 2.2. In this chapter we discuss the case where the DDSM is used in applications other than as a divider controller. Therefore, we need to build upon what was already presented in Section 2.2 with further details.

Let us consider having a generic input signal, denoted by $x[n]$. According to (2.2), we have that:

$$y[n] = x[n] + e_q[n], \tag{8.1}$$

where $e_q[n]$ is the quantization error introduced by the modulator. As previously discussed, the statistical and spectral properties of the quantization error depend on the noise transfer function of the modulator. The noise transfer function needs to be high-pass filtered in order to move the quantization error out of the signal band. For this reason, the $NTF(z)$ of a conventional DDSM is typically designed to be equal to $(1 - z^{-1})^l$ as anticipated in (2.5), where l represents the order of the modulator [50]. In this case, according to (2.3), the quantization error is given by:

$$e_q[n] = \sum_{i=1}^{l} (-1)^i \binom{l}{i} e[n-i], \tag{8.2}$$

where $e[n]$ is the truncation error added by the quantizer, as shown in Fig. 2.1. That being so, we have that:

$$e[n] \in (-1, 0]. \tag{8.3}$$

This result, combined with (8.1) and (8.2), while assuming that:

$$x[n] \in [0, 1), \tag{8.4}$$

gives that the output $y[n]$ can assume values in the range:

$$-2^{l-1} + 1 \leq y[n] \leq 2^{l-1}. \tag{8.5}$$

The range of the DDSM output provides valuable information when evaluating the interaction of $y[n]$ with a nonlinearity. In fact, as the range increases, the

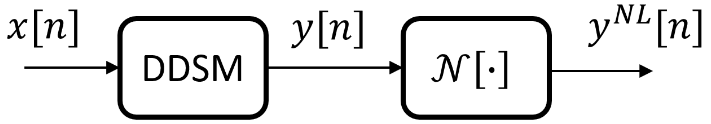

Figure 8.1: Block diagram of the signal chain through the requantization and the nonlinear distortion.

signal is potentially exposed to a wider and more complex nonlinearity. This will be exemplified in the following.

As mentioned before, even though the modulator is designed so that the quantization error has well-defined noise characteristics, the presence of and the interaction with a nonlinearity lead to the generation of excess noise. Let us consider that the output of the DDSM encounters a nonlinearity which distorts $y[n]$ into a signal:

$$y^{NL}[n] = \mathcal{N}\left[y\left[n\right]\right], \tag{8.6}$$

where $\mathcal{N}\left[\cdot\right]$ denotes the discrete nonlinear function. This is also shown schematically in Fig. 8.1. An example is provided in Fig. 8.2, where an LSB dithered MASH 1-1 modulator is considered. In this example, $l = 2$ and equations (8.2) and (8.5) apply. It is worth noticing that the output signal of the MASH 1-1 can only assume discrete values in $\{-1, 0, 1, 2\}$. For this reason, the nonlinearity can be expressed as a discrete function defined over the domain $[-1, 2]$, as shown in Fig. 8.2(a). Fig. 8.2(b) shows that the interaction with the nonlinearity leads to the formation of a set of spurious tones and an elevated low-frequency noise floor, commonly referred to as folded noise [28], [75].

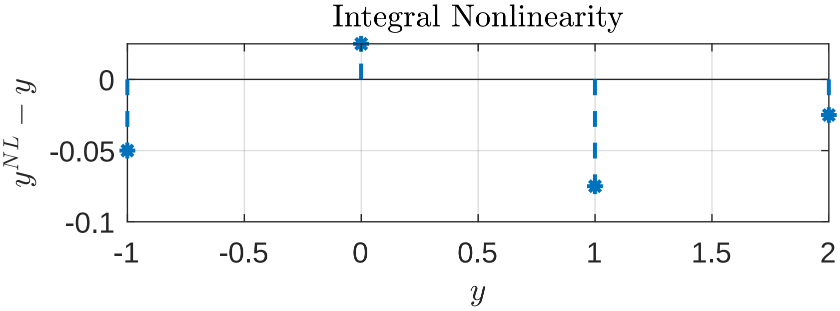

(a)

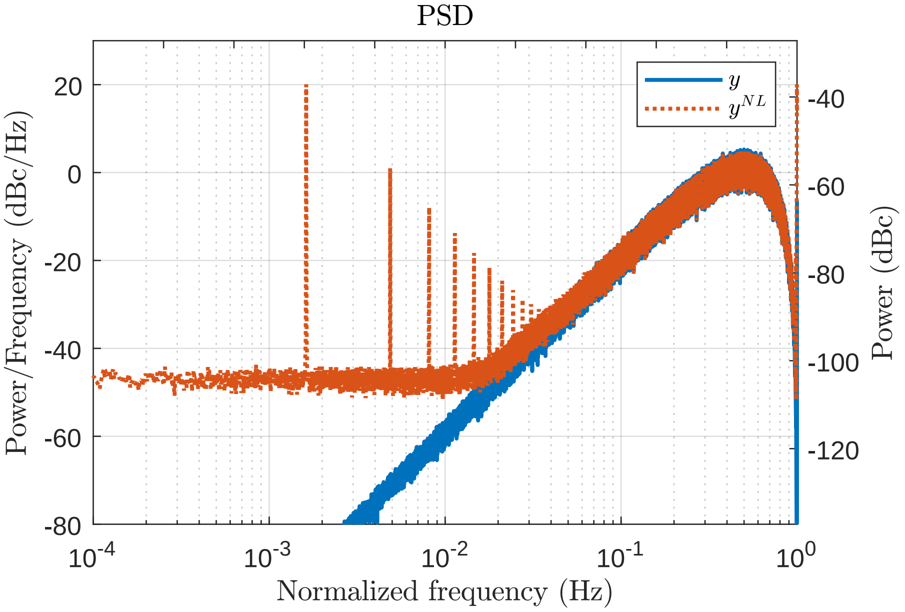

(b)

Figure 8.2: (a) Example of a nonlinearity and (b) a comparison of the simulated PSDs of the DDSM output $y[n]$ and its distortion y^{NL}, in the case of a conventional MASH 1-1 modulator with a constant input $x = 1701/2^{20}$.

8.3 INIS-DDSMs

8.3.1 Architecture

INIS-DDSMs are designed to achieve spur immunity in the case of a static nonlinearity with moderate additional hardware cost compared to a conventional MASH DDSM. Each INIS-DDSM can be implemented with an EFM structure, as shown in Fig. 2.1. The governing equation is

$$Y(z) = STF(z)X(z) + NTF(z)E(z), \tag{8.7}$$

where the magnitude of the $STF(z)$ is equal to unity. The $NTF(z)$ of an l^{th} order INIS-DDSM has the form:

$$NTF(z) = 1 + \sum_{i=1}^{l} d_i z^{-i}. \tag{8.8}$$

Moreover, according to (2.4), the $NTF(z)$ is obtained by choosing:

$$H(z) = 1 - NTF(z) = -\sum_{i=1}^{l} d_i z^{-i}. \tag{8.9}$$

According to the expressions in (2.3), the Z-transform of the quantization error of an INIS-DDSM is given by:

$$E_q(z) = E(z)NTF(z) = E(z)\left(1 + \sum_{i=1}^{l} d_i z^{-i}\right). \tag{8.10}$$

The quantization error is expressed in the time domain as:

$$e_q[n] = e[n] + \sum_{i=1}^{l} d_i e[n-i]. \tag{8.11}$$

At this point, we list the key parameters that determine the performance of an INIS-DDSM. These are as follows:

- l: the order of the modulator.

- h: the order of low-frequency high-pass shaping of the quantization error.
- w: the width of the range of the DDSM output.
- u: the order of polynomial nonlinearities up to which the quantization error is immune from spurs.

8.3.2 Order of the modulator

The order of the modulator, l, sets the number of coefficients d_i in (8.8) which, in turn, determines the signal e_q generated by the modulator. Therefore, the value of l determines the number of degrees of freedom when designing the INIS-DDSM. Moreover, the value of l also affects the hardware cost. In fact, the larger is l the greater is the number of delay elements (registers) that are needed to implement the transfer function $H(z)$ in (8.9).

8.3.3 Order of high-pass shaping of $e_q[n]$

As mentioned previously, it is important to high-pass shape the PSD of $e_q[n]$. In this way, the low-frequency component of the modulation-related noise is suppressed. Therefore, the order of high-pass shaping at low frequencies, h, has to be chosen greater than or equal to one. In particular, the value of h is given by the number of solutions of $E_q(z) = 0$ at $z = 1$. This means that the $NTF(z)$ of an INIS-DDSM must have at least one zero at $z = 1$. In other words, the coefficients d_i in (8.8) need to satisfy:

$$1 + \sum_{i=1}^{l} d_i = 0. \tag{8.12}$$

It is worth noticing that the value of h affects the number of degrees of freedom available for designing the modulator. In fact, the value of h put constraints on the values that can be assumed by d_i. Furthermore, the number of degrees of freedom given by l is decreased to $(l - h)$.

8.3.4 Range of the DDSM output

We mentioned in the previous section that the spread of the DDSM output signal $y[n]$ is an important parameter. In fact, it defines the extent of the exposure of $y[n]$ to the nonlinear function. In the case of an INIS-DDSM, according to (2.2), (8.3), (8.4) and (8.11), and choosing each coefficient d_i to have an integer value, one can obtain that:

$$y[n] \in \left[-\sum_{d_i>0} d_i, -\sum_{d_i<0} d_i \right]. \tag{8.13}$$

Therefore, the spread of $y[n]$ is given by:

$$w = \sum_{i=1}^{l} |d_i|. \tag{8.14}$$

For the sake of completeness, considering also the condition (8.12) and the definition (8.14), the range of $y[n]$ can be rewritten as $\left[\frac{1-w}{2}, \frac{w+1}{2}\right]$[1].

8.3.5 Order of spur immunity

The last and most important parameter to discuss is u. It represents the order of polynomial nonlinearity up to which the quantization error is immune from spurs. In practice, the nonlinear function encountered by $y[n]$ and, therefore $e_q[n]$, is a discrete function defined on a set of $(w + 1)$ points. This means that a generic nonlinearity $\mathcal{N}[\cdot]$, limited to the range of $y[n]$, can always be expressed as a polynomial function with order w. Therefore, in order to achieve spur immunity independently of the nonlinearity, each INIS-DDSM needs to provide an order of

---

[1] This is given by the fact that the range limits of $y[n]$ in (8.13) are such that their difference is equal to -1 because of (8.12), while their sum is equal to w because of (8.14).

immunity, u, that is greater than or equal to w. In particular, each INIS-DDSM aims to satisfy:

$$u = w. \tag{8.15}$$

Further details are given in the following section.

The condition (8.15) suggests that it is desirable to minimize the value of w. In fact, the smaller is the spread of $y[n]$ the smaller is the value of u that is required. However, in order to decrease the value of w, the number and values of non-zero coefficients among d_i should be minimized. This condition forces tighter constraints on the choice of the values of d_i that, in turn, obstruct the selection of greater values of h for a given l. The latter should not be chosen arbitrarily large since it would require a higher hardware cost. In conclusion, assuming a level of spur immunity u, the condition in (8.15) forces tradeoffs while designing the INIS-DDSM in terms of noise shaping (h) and hardware cost (l).

8.4 Analysis of Spur Immunity

In order to demonstrate the level of spur immunity of INIS-DDSMs, we will first assume that the *classical model of quantization* (CMQ) applies [77], [78]. This assumes that the error generated by the quantizer, e, can be modelled as an independent and identically distributed (i.i.d.) random process that is also independent of the system input. Moreover, the CMQ also postulates that the error is uniformly distributed. As pointed out several times throughout this thesis, the conditions assumed by the CMQ are not strictly valid but only an approximation. However, as we will see in the following, the results obtained from such assumptions are empirically confirmed.

The CMQ allows us to prove the spur immunity of INIS-DDSMs by applying the theory of nonsubtractive dither [80], [79]. An example of a nonsubtractively

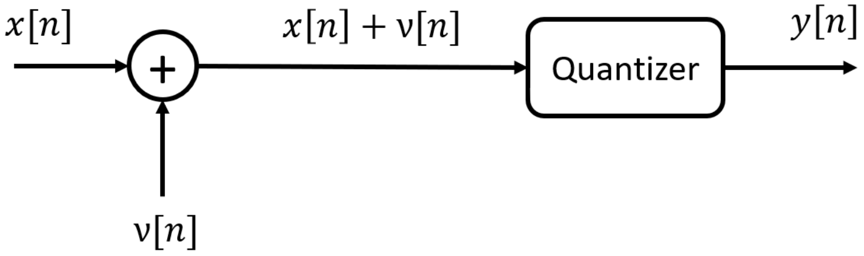

(a)

Figure 8.3: Block diagrams of a nonsubtractively dithered (NSD) quantizing system [79].

dithered (NSD) quantizing system is given in Fig. 8.3. Here, a dither signal, denoted by $\nu[n]$, is added to the input $x[n]$ and the sum is fed to the quantizer which provides the output $y[n]$. As discussed before, the quantizer introduces an error $e[n]$ such that:

$$y[n] = x[n] + \nu[n] + e[n]. \tag{8.16}$$

Notice that, according to the result in (8.1), also in a DDSM we can interpret the output as equal to the input plus the error from the quantizer $e[n]$, plus a dithering signal:

$$\nu[n] = e_q[n] - e[n]. \tag{8.17}$$

In particular, in the case of an INIS-DDSM, because of the result in (8.11), the dither signal is given by:

$$\nu[n] = \sum_{i=1}^{l} d_i e[n-i]. \tag{8.18}$$

At this point we need to recall [79, Theorem 6] which states that[2]:

> A nonsubtractive dither signal $\nu[n]$ generated by the summation of m statistically independent uniformly distributed random processes with peak-to-peak

---

[2] It is worth remarking that we used a different nomenclature compared to [79]. The total quantization error $e_q[n]$ is denoted in that work as ϵ.

amplitudes equal to integer multiples of quantizer's LSBs, renders $E\left[e_q^i[n]\right]$ independent of the system input distribution for $i = 0, 1, ..., m$.

The condition implied by this theorem is equivalent to saying that the quantization error generated by the system is immune from spurs in the case of polynomial distortion up to order m. In fact, let us consider the evaluation of the PSD of the quantization error distorted by a polynomial nonlinearity, namely e_q^{NL}. Because of the properties assumed by the theorem, $e_q[n]$ is a wide-sense stationary process, as is e_q^{NL}, and the Wiener–Khintchine theorem can be applied. Therefore, the PSD of e_q^{NL} is obtained as the discrete-time Fourier transform of the autocorrelation of e_q^{NL}. Then, if the polynomial nonlinearity does not exceed order m, the autocorrelation of e_q^{NL} will not retain any dependency or periodicity from the input signal and, therefore, the spectrum will be spur-free.

According to the CMQ assumption, the error e is a uniform and i.i.d. stochastic process. Moreover, the peak-to-peak value of $e[n]$ is equal to unity, as shown in (8.3), which is equal to one LSB of the quantizer considered so far. Therefore, under the approximation of CMQ and according to (8.18) and [79, Theorem 6], the i-th moment of the quantization error, $E\left[e_q^i[n]\right]$, is independent of the system's input distribution up to an order u equal to the number of non-zero integer coefficients d_i. This is true if the CMQ assumption is valid. Unfortunately, the CMQ is only an approximation. In fact, we empirically observed that the order of spur immunity u manifested by an INIS modulator is often limited to a value that is lower than the number of the non-zero integer coefficients d_i. This can be explained by the theory presented by the authors who invented the Successive Requantizers. They not only analyzed the theoretical limit of the order of spur immunity for the accumulated quantization error (see Sec. 6.2.3), but also the one for the quantization error of the modulator [42], [67][3]. In particular, the

---

[3] It is worth remarking that we use a different nomenclature compared to [42] and [67].

authors stated that, given a modulator with an accumulated quantization error that has a range width of $2r$, not only is the maximum order of spur immunity of e_{acc} equal to $2r - 1$, but also the maximum order of spur immunity of e_q is equal to:

$$u_{opt} = 4r - 3, \tag{8.19}$$

as described in [67]. In fact, we empirically observed that the order of spur immunity u is given by the number of integer non-zero coefficients d_i as long as this number does not exceed $4r - 3$.

That being said, because of the definition of w in (8.14), the condition of inherent spur immunity ($u \geq w$) can be satisfied only for $u = w$, as anticipated in (8.15), when the number of the non-zero coefficients d_i is smaller or equal to $4r - 3$ and each of them is either -1 or $+1$. Therefore, we require that for an INIS-DDSM to exhibit inherent spur immunity it is necessary that:

$$\begin{cases} d_i \in \{-1, 0, 1\} & \forall \; i \in [1, l] \\ \sum_i |d_i| \leq 4r - 3 \end{cases} \tag{8.20}$$

In Table 8.1, we list a few examples of INIS modulators with different orders, noise shaping and range of output, that satisfy the conditions in (8.20).

8.5 Worked Examples

In Section 8.3 we have described the generic architecture and characteristics of INIS-DDSMs. Then, we have analyzed the property of spur immunity in Section 8.4 and translated it into the requirement given in (8.20). Here, we provide two worked examples of INIS DDSMs, one that satisfies the conditions in (8.20) and another that doesn't.

The quantization error $e_q[n]$ and its order of spur immunity u are denoted in those works by, respectively, $s[n]$ and h_s.

Table 8.1: Examples of relevant configurations of INIS $\Delta\Sigma$ modulators

Architecture	l	h	w	r	u_{opt}	$NTF(z)$	u
S1	4	1	3	1.5	3	$(1 - z^{-1} - z^{-2} + z^{-4})$	3
S2	6	1	5	2	5	$(1 - z^{-1} + z^{-2} - z^{-4} - z^{-5} + z^{-6})$	5
S3	6	2	5	2	5	$(1 - z^{-1} + z^{-2} - z^{-3} - z^{-4} + z^{-6})$	5
S4	9	2	7	3	9	$(1 - z^{-1} - z^{-2} + z^{-5} + z^{-6} - z^{-7} + z^{-8} - z^{-9})$	7

8.5.1 Working Example

Let us consider the INIS S3 DDSM given in Table 8.1 with the following noise transfer function:

$$NTF(z) = 1 - z^{-1} + z^{-2} - z^{-3} - z^{-4} + z^{-6}. \tag{8.21}$$

As previously discussed, this modulator can be implemented with an EFM structure as in Fig. 2.1, with the transfer function $H(z)$ equal to:

$$H(z) = z^{-1} - z^{-2} + z^{-3} + z^{-4} - z^{-6}. \tag{8.22}$$

The order l is equal to 6 which is also the number of delay elements required to implement $H(z)$ in (8.22). One can notice that the NTF in (8.21) is such that it has two zeroes at $z = 1$. This means that the PSD of $e_q[n]$ has an order of high-pass shaping $h = 2$. Moreover, according to (8.13) and (8.14), the output $y[n]$ has a spread $w = 5$ and a range $[-2, 3]$. Therefore, each nonlinearity encountered by $y[n]$ can be fitted exactly by a fifth-order polynomial function. Furthermore, one can derive from the definition of r in (6.8) that the accumulated quantization error has an half-range width $r = 2$. Then, according to the analysis conducted in Section 8.4, since (8.20) is fulfilled, the modulator satisfies (8.15), providing an order of spur immunity $u = 5$. Consequently, the modulator is expected to have spur-free operation independently of the static nonlinearity. This is confirmed in Fig. 8.4, where the behavior of this INIS-DDSM is simulated in the case where the modulator's output is distorted by[4]

$$\mathcal{N}[\cdot] = 0.025 + 0.949\,[\cdot] - 0.113\,[\cdot]^2 + 0.0477\,[\cdot]^3 + 0.0256\,[\cdot]^4 - 0.00896\,[\cdot]^5\,, \tag{8.23}$$

---

[4] The argument of the nonlinear function in (8.23) is given into square brackets since $\mathcal{N}[\cdot]$ is a discrete function. In fact, it is applied to the output of the modulator which assumes only a finite number of integer values.

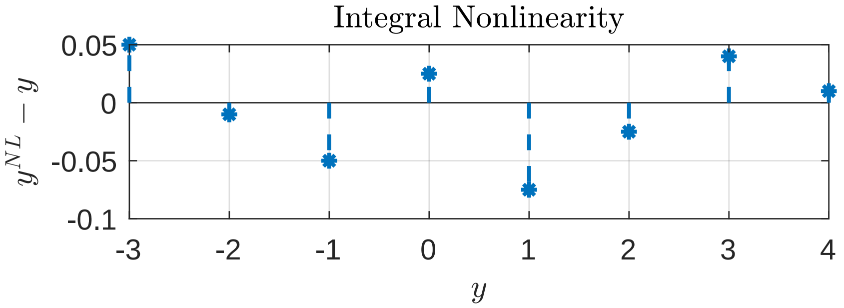

(a)

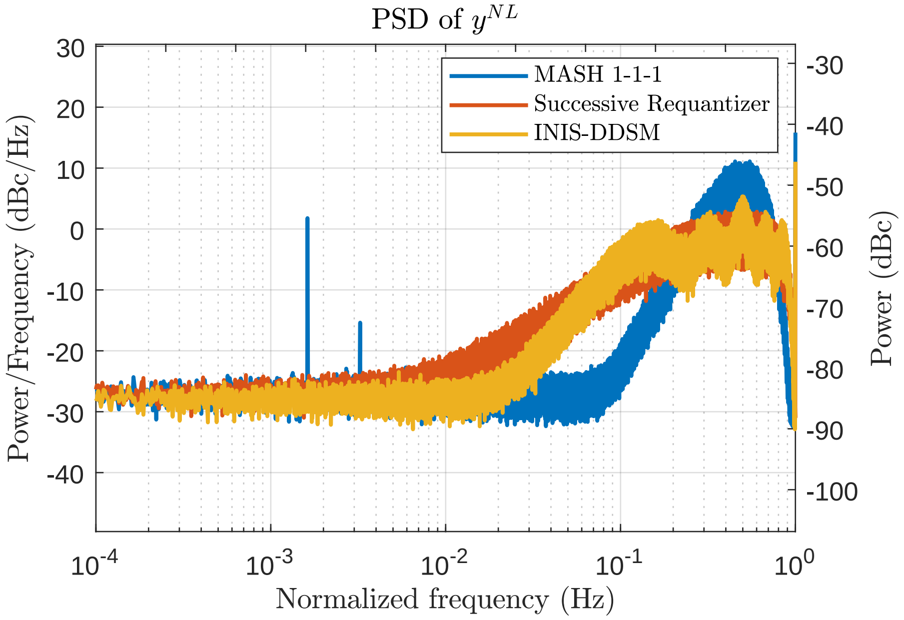

(b)

Figure 8.4: (a) Example of a nonlinearity and (b) a comparison of the simulated PSDs of the distorted DDSM output $y^{NL}[n]$, in the case of a conventional MASH 1-1-1, an SR [67, Fig 4(b)] and the INIS S3 DDSM described in (8.21) with constant input $x = 1701/2^{20}$.

which fits the nonlinear function given in Fig 8.4, over the range $[-2, 3]$. The results are also compared to those of a conventional MASH 1-1-1 and the SR described in [67, Fig 4(b)]. It is worth noticing that the NTF of the MASH 1-1-1, which is equal to $(1 - z^{-1})^3$, has the shape of (8.8) but it does not satisfy (8.20) and therefore does not have the spur property immunity. The SR, instead, is also characterized by having w and u equal to 5, meaning that it is expected to be immune from spurs [42], [67]. The nonlinearity adopted for the simulation is depicted in Fig. 8.4(a). The results in Fig. 8.4(b) confirm the spur-free operation of both the INIS-DDSM and SR, while all three modulators experience similar levels of folded noise. The INIS-DDSM and, especially, the SR introduce more noise than the MASH in the normalized frequency range $[0.01, 0.1]$. This is partially due to the fact that, while the MASH 1-1-1 has a shaping order $h = 3$, h is equal to 2 for the INIS and $h = 1$ for the SR. This instantiation of an INIS-DDSM achieves these performances with a hardware cost that is roughly 80% higher than that of the MASH 1-1-1, but less than one fifth that of the SR [67]. This is summarized in Table 8.2. Therefore, the INIS-DDSM represents a solution with inherent spur immunity but with slightly lower noise than the SR and with a moderate increase in hardware cost compared to the MASH.

8.5.2 Non Working Example

In order to show that both conditions in (8.20) are needed to achieve inherent spur immunity, we now give an example of an INIS modulator that satisfies the first but not the second condition in (8.20).

Let us consider the DDSM with the following NTF:

$$NTF(z) = 1 - z^{-1} + z^{-3} - z^{-4} - z^{-5} + z^{-6}. \tag{8.24}$$

It is an INIS DDSM as its NTF belongs to the generic form given in (8.8). This

Table 8.2: Hardware cost comparison.

DDSM	Hardware cost
MASH 1-1-1	100%
INIS of (8.21)	$\approx 150 - 180\%^*$
SR	$\approx 800\%$

*Similarly to what we discussed for the ENOP modulators in Chapter 7, the hardware cost of an INIS DDSM depends on the particular implementation, such as SQ or cascaded.

INIS has a few similarities with the S3 as both have order $l = 6$, an output $y[n]$ with range $[-2, 3]$ and, therefore a spread $w = 5$. This means that, in order to achieve inherent spur immunity, e_q needs to be immune from spurs in the case of polynomial nonlinearities up to order $u = 5$. As discussed in the previous section, one requirement for (8.15) is that each non-zero coefficient d_i has an absolute value equal to one. The latter is satisfied by the NTF in (8.24). However, this is not enough as the INIS also needs to fulfil the second condition of (8.20) forced by the theoretical limit for u given by previous authors in [42], [67].

Unfortunately, the INIS defined by (8.24) does not satisfy the latter requirement. In fact, one can notice that, from (2.8) and (8.3), the NTF in (8.24) leads to an accumulated quantization error with a half-range width $r = 1.5$. Then, the maximum achievable order of spur immunity is u_{opt} is equal to 3. It is lower than what is required by (8.15). It follows that this example of INIS DDSM does not achieve inherent spur immunity. This is verified by simulation as shown in Fig. 8.5. We considered the fifth order polynomial nonlinearity of the previous example, given in (8.23) and shown in Fig. 8.5(a). The result in Fig. 8.5(b) is self explanatory and confirms that this INIS DDSM is not immune from spurs

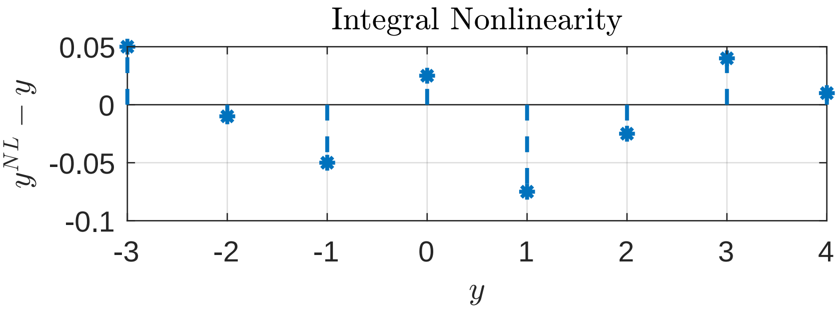

(a)

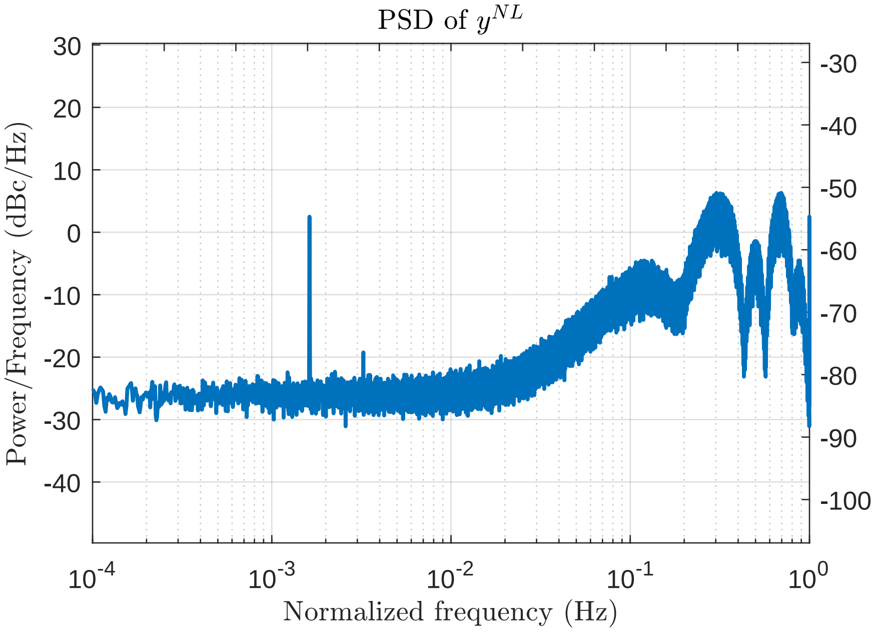

(b)

Figure 8.5: (a) Example of a nonlinearity and (b) the simulated PSD of the distorted DDSM output $y^{NL}[n]$, in the case of the INIS DDSM described in (8.24) with constant input $x = 1701/2^{20}$. This example is not inherently immune to polynomial distortion.

and that both conditions in (8.20) are required in order to achieve inherent spur immunity.

8.6 Comparison with another spur mitigation technique

In previous works, other techniques have been presented for mitigating the spurs generated by the distortion of the modulator's output [75], [76]. In this section we compare the performance of an example of INIS modulator with a conventional MASH 1-1 whose output is randomized through bit rotation [75]. It has been shown in [75] that the rotation of the output bits of a MASH 1-1 with an LSB dither signal works effectively in mitigating the nonlinearity-induced spurs.

For comparison, we consider an INIS S1 DDSM given in Table 8.1 with the following noise transfer function:

$$NTF(z) = 1 - z^{-1} - z^{-2} + z^{-4}. \tag{8.25}$$

Note that this modulator provides an accumulated quantization error with half-range width $r = 1.5$. Then, according to the considerations given in the previous section, this INIS modulator achieves inherent spur immunity and its output y[n] assumes values in $[-1, 2]$. The latter is the same range of the output of a conventional MASH 1-1. Then, let us consider the nonlinearity shown in Fig. 8.6(a). This can also be represented analytically by the following polynomial function:

$$\mathcal{N}[\cdot] = 0.25 + 0.933[\cdot] - 0.0875[\cdot]^2 + 0.0542[\cdot]^3. \tag{8.26}$$

As a confirmation of the expected spur immunity, one should notice that, according to the analysis in Sec. 8.4, the NTF in (8.25) returns a spur immunity up to order $u = 3$, which is also the order of the nonlinearity in (8.26). Simulations

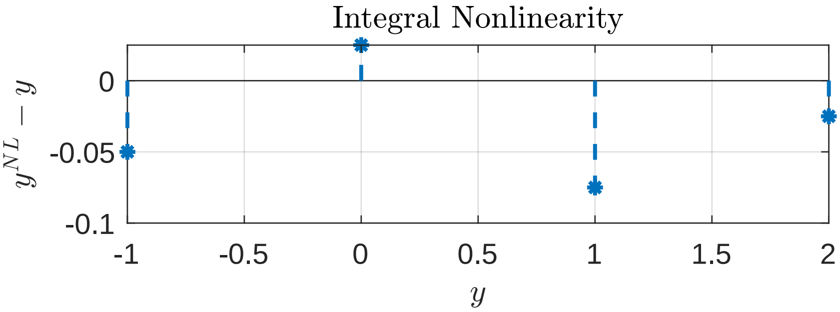

(a)

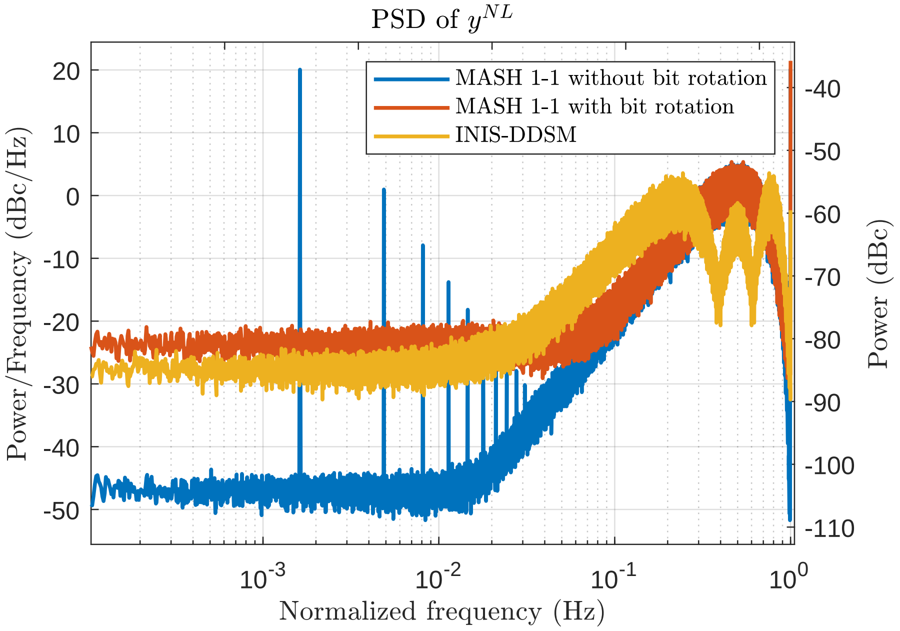

(b)

Figure 8.6: (a) Example of a nonlinearity and (b) a comparison of the simulated PSDs of the distorted DDSM output $y[n]$ in the case of a conventional MASH 1-1 with and without bit rotation, and the INIS S1 DDSM described in (8.25) with constant input $x = 1701/2^{20}$.

have been performed and the results are shown in Fig. 8.6(b). The PSD of the distorted output y^{NL} experiences strong nonlinearity-induced spurs. On the other hand, both the use of bit rotation and the INIS-DDSM effectively mitigate the spurs. This result comes with an increased folded noise floor. In particular, this is approximately 5 dB higher in the case of the MASH 1-1 with bit rotation. The INIS-DDSM provides a better PSD for normalized frequencies up to 0.025, while it is worse than the MASH 1-1 with bit rotation in the range $[0.025, 0.3]$. The worse spectrum at mid-high frequencies is due to the fact that the noise transfer function in (8.25) does not shape the noise as aggressively as the MASH 1-1. However, such high-frequency noise content is typically outside the signal band of interest and can be attenuated by filtering.

8.7 Comparison between INIS, ENOP and SR

In Chapter 6 and in this chapter, we have presented two new families of DDSMs. These aim to optimize the spur performance of the DDSM quantization error and its accumulation in the case of polynomial distortion. The reader might notice that, even though INIS and ENOP DDSMs address different types of problems, the governing equations, as well as their properties, are similar. Let us remark that both families of modulators derive their properties from their noise transfer functions. These are (6.2) and (8.8) for ENOP and INIS DDSMs, respectively. In particular, one should notice that the expressions in (6.2) and (8.8) are such that the NTF of each ENOP modulator can be rewritten in the form of (8.8). Moreover, because of the condition required by (8.12), the NTF of an INIS can also be rewritten like that of an ENOP, given in (6.2). These considerations may lead to the conclusion that the two families are interchangeable. This is not true if we require that the modulators achieve optimal performance, i.e. that equations (6.9) and (8.15) are met for the ENOP and the INIS, respectively.

Let us present a few examples to clarify this concept. Consider the INIS S1 modulator defined by (8.25). Its NTF is equal to that of the ENOP P1 in Table 6.1, except for the term $(1 - z^{-1})$. This is the same difference between the two governing equations (6.2) and (8.8). According to what has been described above, each ENOP is also an INIS. In fact, the NTF of the ENOP P1 can be rewritten as:

$$NTF_{ENOP_{P1}}(z) = 1 - 2z^{-1} + z^{-3} + z^{-4} - z^{-5}. \tag{8.27}$$

It has the form of an INIS as given in (8.8). However, according to the analysis in Section 8.4, the NTF in (8.27) does not meet the condition in (8.20) and, therefore, the ENOP P1 is an INIS but it does not have optimal spur immunity for e_q. On the other hand, because of the satisfaction of (8.12), the INIS S1 is also an ENOP and its NTF, given in (8.25), can be rewritten as:

$$NTF_{INIS_{S1}}(z) = (1 - z^{-1})(1 - z^{-2} - z^{-3}). \tag{8.28}$$

This expression follows the generic form of an ENOP modulator given in (6.2). However, it does not satisfy the condition in (6.6) which is required of an ENOP modulator in order to achieve high-pass shaped e_{acc}. Therefore, the INIS S1 is not suitable for the applications addressed by the ENOP modulators.

Another example is given by the INIS S3 modulator described in (8.21). As done before, we can represent its NTF in the form of an ENOP, as:

$$NTF_{INIS_{S3}} = (1 - z^{-1})(1 + z^{2} - z^{-4} - z^{-5}). \tag{8.29}$$

It is worth noticing that the INIS S3 not only complies with (6.2) but every non-zero coefficient c_i also has absolute value equal to one. As discussed in Section 6.2, the latter condition has been noticed to allow one to achieve the optimal value for the spur immunity p. This is also the case for the INIS S3[5]. Therefore, the INIS S3 represents a case of an ENOP/INIS modulator that achieves both optimal spur immunity conditions (6.9) and (8.15). It is worth noticing that the latter is not necessarily the best condition to pursue at all costs, as it could lead to compromises on other components of noise, such as the linear term discussed in Sec. 6.7, that could be more detrimental in a chosen application.

Summarizing, we can say that, given a modulator from either the ENOP or the INIS family with optimal spur immunity in terms of either e_{acc} or e_q, it could be interpreted as a modulator of the other family; however, it does not necessarily mean that the modulator would achieve optimal performance or suitable characteristics for the applications addressed by the other family of modulators. For this reason we prefer to present the ENOP and INIS modulators as separate architectures.

For the sake of completeness, we will briefly compare the considerations carried out for the ENOP and INIS modulators with the results of Successive Requantizers. In [33], they provided an example of a first order Successive Requantizer (SR1) that achieves both limits of spur immunity of e_q and e_{acc}. However, because of the lack of high-pass shaping, such an SR1 introduces high in-band noise when used as a divider controller in a frac-N PLL. For this reason, the authors decided to move to more aggressively shaped solutions, like the SR2 [43]. They did that at the cost of losing the optimal spur immunity condition on the quantization

---

[5] For the sake of brevity we will not analyze the spur immunity of the modulator described in (8.29). In fact, it follows the same procedure conducted for the ENOP P1 in Section 6.3. We invite the reader to use the approach described in Appendix A to obtain (6.12) as the probability distribution of e_{acc} for the INIS S3. Then, the histogram of e_{acc} can be simulated and shown to match that given by (6.12). Finally, the resulting PNN evaluated in the case of cubic nonlinearity would show that the order of spur immunity is $p = 3$, which is optimal since $r = 2$.

error. In [43], they provide a few examples of successive requantizers with higher than first-order quantization noise shaping; however, these could not ensure an order of spur immunity, u, greater than one.

That being said, we can summarize the performance of the aforementioned examples of ENOP and INIS modulators and compare them with each other and with state-of-the-art SRs in Table 8.3. It is mandatory to remark that, as discussed for the ENOP modulators in Section 6.6, the spur immunity performance of the INIS solutions has also been evaluated empirically and not theoretically, unlike what was done for the Successive Requantizers.

Table 8.3: Spur performance comparison between examples of ENOP, INIS and SR

DDSM	noise shaping order of e_q (h)	half width range of e_{acc} (r)	optimal spur immunity of e_{acc} ($p = 2r - 1$)	optimal spur immunity of e_q ($u = 4r - 3$)
ENOP P1 (8.27)	2	2	✓	×
INIS S3 (8.29)	2	2	✓	✓
SR1 [33, eq. (40)]	1	2	✓	✓
SR2 [43, eq. (23)]	2	3	✓	×

Concluding, the results presented in Table 8.3 show that members of the ENOP/INIS families can achieve spur immunity limits for both e_q and e_{acc}

simultaneously, while not compromising on noise shaping. This makes the INIS S3 superior to both the SR1 and SR2 in terms of noise shaping order and half-width range respectively.

8.8 Summary

In this chapter, we have presented a family of $\Delta\Sigma$ modulators that achieve spur-free operation independently of the static nonlinearity encountered. The architecture and characteristics are described. An analysis has been presented to prove the inherit spur immunity of the INIS-DDSMs. Then, representative examples are given, showing the performance of INIS-DDSMs.

Chapter 9

Conclusions

9.1 This work

In this thesis we have introduced, analyzed, modelled and mitigated diverse detrimental phenomena induced by nonlinearities in fractional-N frequency synthesizers.

In Chapter 3, we have introduced and described the phenomenon of horn spurs in a fractional-N CP-PLL-based frequency synthesizer with a MASH 1-1-1 DDSM. The source of these spurs has been explained. We have presented three techniques that allow one to mitigate the horn spurs with negligible downside. Their successful functioning has been confirmed through simulation. Moreover, one of these techniques has been validated with a commercial frequency synthesizer.

In Chapter 4, we have demonstrated how MASH modulators can theoretically exhibit spur immunity in fractional frequency synthesizers with memoryless polynomial nonlinearities. In particular, we analyzed three modulators: MASH 1-1, MASH 1-1-1 and MASH 1-1-1-1. As the order of the MASH modulator increases so does the order of polynomial nonlinearities up to which the modulator is immune from spurs. However, when the order of the MASH DDSM increases, it exposes the system to a larger quantity of noise that translates into a higher nonlinearity-induced noise floor.

In Chapter 5, we have analyzed mathematically the output phase noise generated by the interaction between quantization noise and a static nonlinearity in a fractional-N frequency synthesizer. This has led to the formulation of a method that allows one to predict the nonlinearity-induced folded noise for different DDSMs. The prediction method has been analyzed and tested in simulation for different nonlinearities and MASH modulators. The results have confirmed the accuracy of the method. A comparison with state-of-the-art predictions has been performed. Compared to existing techniques, the presented method delivers greater accuracy over a range of different types of nonlinearities.

In Chapter 6, we have presented a family of $\Delta\Sigma$ modulators, called ENOP DDSMs, which have potential applications as divider controllers in fractional-N PLLs. They are charachterized by the following noise transfer function:

$$NTF(z) = \left(1 - z^{-1}\right)\left(1 + \sum_{i=1}^{l-1} c_i z^{-i}\right). \tag{9.1}$$

ENOP DDSMs can be designed to be optimal in the sense of Familier and Galton in terms of spurious tone immunity when interacting with polynomial nonlinearities, while minimizing the folded noise. The level of spur immunity has been predicted analytically and confirmed by simulation. The results show the potential of ENOP-DDSMs to match the state of the art performance in terms of spur immunity. Moreover, with the same level of spur immunity, ENOP DDSMs can outperform the prior-art in terms of folded noise. The behavior of ENOP DDSMs has also been tested in the case of wandering and horn spurs, demonstrating mitigation of both.

In Chapter 7, we have presented different hardware implementations for the family of ENOP DDSMs. The advantages and tradeoffs of each structure have been analyzed. The possibility of hybrid nested configurations has also been investigated. Moreover, practical examples of how to implement both ENOP and hybrid MASH-ENOP modulators has been provided.

In Chapter 8, we have presented a family of $\Delta\Sigma$ modulators that can achieve spur-free quantization error independently of the static nonlinearity encountered. These are called INIS DDSMs and they are characterized by the following noise transfer function:

$$NTF(z) = 1 + \sum_{i=1}^{l} d_i z^{-i}. \tag{9.2}$$

INIS DDSMs have potential for use as a DCO controller. The architecture and characteristics are described. An analysis has been presented to prove the inherent spur immunity of INIS-DDSMs. Then, representative examples are given, showing their spectral performance.

9.2 Future works

The study and mitigation of nonlinearity-induced spurs carried out in this thesis focused mainly on the case of CP-based fractional-N frequency synthesizers where the nonlinearity is assumed to be static and can be approximated by a polynomial function. Future work can be done about:

- The analysis and consequent mitigation of noise generated by dynamic as well as static nonlinearities.
- The research of spur mitigation techniques when the nonlinearity has a more generic expression rather than polynomial, and particularly in the presence of hard nonlinearities, such as those found in all digital PLLs.
- The investigation of the prediction and suppression of nonlinearity-induced noise in digitally-intensive fractional-N frequency synthesizers.

Appendices

Appendix A

Prediction of probability density function of e_{acc}

In previous publications [32], [14], it has been shown that the spurious behavior resulting from the interaction between the quantization error and system nonlinearities can be predicted by the PNN. Evaluation of the PNN requires knowledge of the probability distribution function of the accumulated quantization error, denoted by $P(\cdot)$. In this appendix, we provide a method to predict $P(\cdot)$ for a generic MASH or ENOP DDSM, under the assumption that e is an independent and identically uniformly distributed $\mathcal{U}(-1, 0)$ stochastic process. We would like to remark that the hypothesis of e to be an uniform i.i.d. stochastic process is only an approximation. For the fact itself that e is not i.i.d., randomization techniques are used to break the periodicities of the quantization error generated by the modulator. These make the PSD of the quantization error smooth and free from idle tones. Intuitively, one may interpret this result that the quantization error tends to behave as an i.i.d. stochastic process when aided by randomization techniques. But, as anticipated, the i.i.d. condition is only an approximation. In fact, as no randomization technique is applied, it is very clear from the pmf and

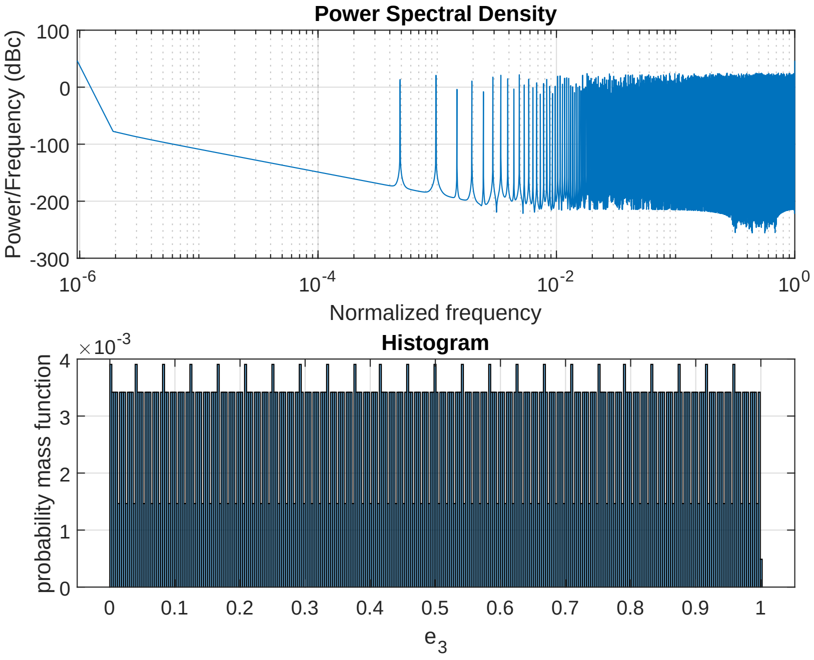

(a)

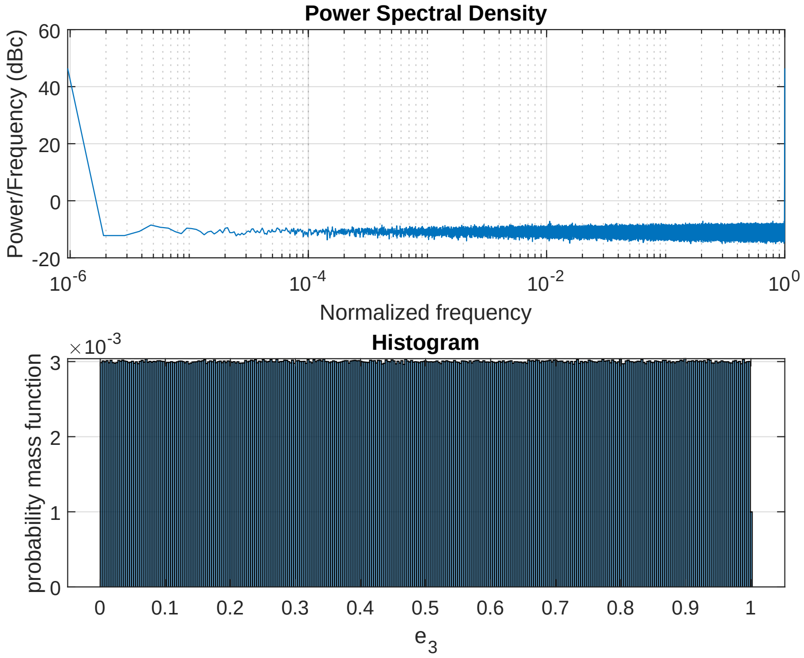

(b)

Figure A.1: Simulated histogram and PSD of the error generated by the third stage of a conventional MASH 1-1-1 with fractional input $X/M = 1024/2^{20}$ and (a) no dither applied, (b) LSB dither applied to the input of the second stage.

PSD of $e[n]$ that it is not an independent and identically distributed stochastic process. This is illustrated in Figs. A.1(a) and (b) in the case of a conventional MASH 1-1-1.

That being said, the distributions evaluated under the assumption of i.i.d. for $e[n]$ have been empirically noticed to be consistent to the simulated ones if the quantization error is randomized through techniques of dithering or limit cycle maximization. Therefore, we make this assumption in order to derive pseudo-analytical expressions for $P(\cdot)$ which are then used to evaluate the PNN and perform analyses in the body of the thesis.

In [68], the author evaluates the probability distribution of a multivariate random function by applying the *variable transformation theorem* [69]. In particular, consider a random variable Y which is a function of k independent random variables with arbitrary probability distributions:

$$Y = g\left(X_1, X_2, ..., X_k\right). \tag{A.1}$$

If we assume that such a function can be expressed explicitly in terms of any of the independent variables (i.e. X_1), so that:

$$X_1 = g_1^{-1}\left(Y, X_2, ..., X_k\right), \tag{A.2}$$

with n_1 possible solutions. Then, the probability density function of Y is [68]:

$$\begin{aligned} f_Y(y) = \int_{x_k=-\infty}^{x_k=\infty} \cdots \int_{x_3=-\infty}^{x_3=\infty} \int_{x_2=-\infty}^{x_2=\infty} \prod_{j=2}^{k} \left(f_{X_j}\left(x_j\right) dx_j\right) \times \\ \sum_{i=1}^{n_1} f_{X_1}\left(g_{1,i}^{-1}\left(y, x_2, x_3, ..., x_k\right)\right) \left| \frac{\partial g_{1,i}^{-1}\left(y, x_2, x_3, ..., x_k\right)}{\partial y} \right| \end{aligned} \tag{A.3}$$

Assuming that e is a uniform and i.i.d. stochastic process, each pair of signals $e[n-u]$, $e[n-v]$ is independent for every $u \neq v$. According to this assumption and the expressions in (4.3), one can notice that the accumulated error e_{acc} of a MASH DDSM is a function of l independent random variables, where l is the order of the modulator. For the sake of simplicity, let us denote each random variable $e[n-v]$ by e_v. Doing so, we can represent e_{acc} as:

$$e_{acc} = e_0 + c_1 e_1 + c_2 e_2 + ... + c_{l-1} e_{l-1}, \tag{A.4}$$

It is clear that the function in (A.4) can be expressed explicitly in terms of any e_v with only one solution. Let us consider for instance e_0:

$$e_0 = e_{acc} - c_1 e_1 - c_2 e_2 + ... - c_{l-1} e_{l-1}. \tag{A.5}$$

Furthermore, let us remember that each e_v is valued only in the range $(-1, 0]$. Then, similarly to (A.3), we can evaluate the probability density function of e_{acc} as:

$$f_{e_{acc}}(y) = \int_{x_{l-1}=-1}^{x_{l-1}=0} ... \int_{x_2=-1}^{x_2=0} \int_{x_1=-1}^{x_1=0} \prod_{v=1}^{l-1} \left(f_{e_v}\left(x_v\right) dx_v \right) \times \\ f_{e_0}\left(y - c_1 x_1 - c_2 x_2 + ... - c_{l-1} x_{l-1}\right) \tag{A.6}$$

This function is also denoted in the thesis by $P(\cdot)$[1].

---

[1] For the prediction of $P(\cdot)$, eq. (A.6) has been evaluated using Mathematica in each case.

Appendix B

Considerations on $\mathcal{N}(\cdot)$

In this thesis we have sometimes considered a polynomial nonlininearity $\mathcal{N}(\cdot)$ which, for the sake of simplicity, was assumed to have a null zeroth-order term and a unity coefficient for the linear one, as represented in (7.10). In this appendix we show that the analysis of spur immunity presented in Chapter 4 does not lose generality when those assumptions for $\mathcal{N}(\cdot)$ are not satisfied. For this purpose, let us denote by $\mathcal{N}_g(\cdot)$ a generic polynomial nonlinearity which is expressed as:

$$\mathcal{N}_g(x) = \sum_i g_i x^i, \tag{B.1}$$

where the coefficients g_i are constant, for any $i \in \mathbb{N}$. Applying the nonlinear function (B.1) in (2.16), the resulting PNN is:

$$PNN_{\mathcal{N}_g}[n] = \sum_k \left(\left(\sum_i g_i (\tau_k(n) + \tau_{os})^i \right) P(\tau_k(n)) \right) \tag{B.2}$$

If the term for $i = 0$ is taken out from the sum in i, and the remaining part is normalized to g_1, the expression becomes:

$$PNN_{\mathcal{N}_g}[n] = g_0 \sum_k P(\tau_k(n)) + \sum_k g_1 \left(\sum_{i \neq 0} \frac{g_i}{g_1} (\tau_k(n) + \tau_{os})^i \right) P(\tau_k(n)), \tag{B.3}$$

where $\sum_k P(\tau_k(n))$ is equal to one for each n, since $e_{acc}[n]$ has to lie on one of the tracks. Moreover, if we denote $\frac{g_i}{g_1}$ by a_i, the sum $\sum_{i\neq 0} \frac{g_i}{g_1}(\tau_k(n)+\tau_{os})^i$ is equivalent to $\mathcal{N}(\hat{\tau}_k(n))$. Therefore, we can write:

$$PNN_{\mathcal{N}_g}[n] = g_0 + g_1 PNN_{\mathcal{N}}[n] \tag{B.4}$$

The result in (B.4) shows that all the analyses about spur immunity carried out in Section 4.3 are valid also in the case of a nonlinearity like (B.1). In fact, $PNN_{\mathcal{N}_g}[n]$ is independent of n if and only if $PNN_{\mathcal{N}}[n]$ is too.

Appendix C

Evaluation of the offset τ_{os}

In Section 4.3 we obtained analytical expressions for the PNN in different cases of polynomial nonlinearities and for different MASH modulators. Those equations are parametrized by the coefficients of the nonlinear terms and the offset τ_{os}.

We have already noted that the value of τ_{os} is such that the mean value of PNN is equal to 0. Here we show how this value is obtained in the different cases we analyzed.

The first case is related to (4.13), where the PNN is not constant. Since the PNN is defined as a discrete-time signal, we should evaluate the sum over the period and find an expression for the value of τ_{os} that zeros the sum. However, the number of points in a period is quite large and the time-step is quite small; therefore we can approximate the function to be time-continuous and evaluate the integral of the expression over one period.

That said, the mean value of (4.13), where n is considered to be continuous, gives:

$$\frac{X}{M}\int_0^{\frac{M}{X}} PNN(n)dn = \frac{a_2}{2}\tau_{os}^2 + \tau_{os} + \frac{a_2}{6}. \tag{C.1}$$

This is zeroed by two values of τ_{os}.

However, with the hypothesis that $|a_2| \ll 1$, i.e. the nonlinearity is not dominant over the linear term, one solution has to be discarded because it returns a huge value for τ_{os} that is in conflict with the assumption of a local representation of the nonlinearity as a truncated power series. Therefore, we are left with (4.14).

In the next two cases of (4.15) and (4.17), the PNN is constant. Therefore, we only need to find the values of τ_{os} that zero those expressions. These are both second-order equations in τ_{os}, but one solution for each pair has to be discarded for the same reason mentioned before. This leaves us with, respectively, (4.16) and (4.18).

In the case of a MASH 1-1 with a cubic nonlinearity, the expression for the PNN is (4.20). As this is a function of n, we evaluate the mean value with an integral over the period. Doing so, we obtain:

$$\frac{X}{M}\int_0^{\frac{M}{X}} PNN(n)dn = a_3\tau_{os}^3 + \frac{1}{2}a_3\tau_{os} + \tau_{os} \tag{C.2}$$

This returns three solutions in τ_{os}, namely $\left\{0, \pm\sqrt{-\frac{a_3+2}{2a_3}}\right\}$. Not all of these are real independently of the value of a_3. Moreover, with the hypothesis that $|a_3| \ll 1$, only the solution at zero is acceptable, for the same reason discussed above. Something similar happens when we move to a MASH 1-1-1. In fact, evaluating the mean value of (4.21), we obtain:

$$\frac{X}{M}\int_0^{\frac{M}{X}} PNN(n)dn = a_3\tau_{os}^3 + \frac{3}{2}a_3\tau_{os} + \tau_{os}, \tag{C.3}$$

where the only valid solution is again $\tau_{os} = 0$. Then there is the case of (4.22) where the PNN is constant. Once again, the equations return three solutions in τ_{os} but only $\tau_{os} = 0$ is acceptable.

Lastly, we have the case of a generic third-order polynomial nonlinearity. The expressions for the PNN are given by (4.26), (4.27) and (4.28). The first two have to be integrated, while the third is constant. Evaluation of the solution for τ_{os} becomes harder because of the presence of both parameters a_2 and a_3. Therefore, we determine the value of τ_{os} numerically, given the values of a_2 and a_3.

Appendix D

Loop Transfer Functions

In this Appendix we provide details of the loop transfer functions of the CP PLL. We refer to the model presented by Perrott *et al.* in [20]. Considering a tristate PFD, the frequency-domain model of the linear synthesizer is shown in Fig. 2.4. For further details about how the model in Fig. 2.4 is obtained, we refer the reader to [20]. The closed-loop transfer function $G(f)$ is given by:

$$G(f) = \frac{T_s N_{div} I_{CP} L(f) K_{VCO}}{j2\pi f N_{div} + I_{CP} L(f) K_{VCO}}, \tag{D.1}$$

where $L(f)$ is the loop-filter transfer function. Once the linearized model of the nonlinear system is given in Fig. 5.3, the $G_{NL}(f)$ is obtained as:

$$G_{NL}(f) = \frac{T_s N_{div} C_{NL} I_{CP} L(f) K_{VCO}}{j2\pi f N_{div} + C_{NL} I_{CP} L(f) K_{VCO}}. \tag{D.2}$$

In conclusion, the output VCO noise component is evaluated from the VCO noise, once it is filtered by the respective transfer function, denoted by $G_{NL,VCO}(f)$. This latter is given by:

$$G_{NL,VCO}(f) = \frac{j2\pi f N_{div}}{j2\pi f N_{div} + C_{NL} I_{CP} L(f) K_{VCO}}, \tag{D.3}$$

where C_{NL} is unity when the system is linear.

Appendix E

Example of calculating $S_{e_{acc}^{NL}}$

In this Appendix we provide a detailed example of how to calculate $S_{e_{acc}^{NL}}$. This should allow one to understand the procedure and replicate it for other cases. Let us suppose we have a MASH 1-1-1 and a quadratic nonlinearity as in (5.8). According to (4.3), the accumulated quantization error is given by:

$$e_{acc}[n] = e[n] - 2e[n-1] + e[n-2]. \tag{E.1}$$

Substituting (5.8) and (E.1) in (5.6), yields:

$$\begin{aligned} R_{e_{acc}^{NL}}[n_0] = E\Big[&\Big((e[n] - 2e[n-1] + e[n-2] + \tau_{os}) + \\ &\quad +a_2\left(e[n] - 2e[n-1] + e[n-2] + \tau_{os}\right)^2\Big) \\ &\Big((e[n-n_0] - 2e[n-n_0-1] + e[n-n_0-2] + \tau_{os}) + \\ &\quad + a_2\left(e[n-n_0] - 2e[n-n_0-1] + e[n-n_0-2] + \tau_{os}\right)^2\Big)\Big], \end{aligned} \tag{E.2}$$

where τ_{os} has to be valued so that $E\left[e_{acc}^{NL}[n]\right] = 0$. Considering the expressions in (5.8) and (E.1), the expected value of $e_{acc}^{NL}[n]$ can be written as:

$$\begin{aligned} E\left[e_{acc}^{NL}[n]\right] = \tau_{os} + E\left[e[n] - 2e[n-1] + e[n-2]\right] + \\ + a_2 E\left[\left(e[n] - 2e[n-1] + e[n-2] + \tau_{os}\right)^2\right]. \end{aligned} \tag{E.3}$$

From the assumptions made in Sec. 5.2, for e to be $\mathcal{U}(-1,0)$ and i.i.d, equation (E.3) reduces to:

$$E\left[e_{acc}^{NL}[n]\right] = \tau_{os} + a_2\left(\tau_{os}^2 + \frac{1}{2}\right), \tag{E.4}$$

which is zero for two values of τ_{os}. However, one of the two has to be discarded as it returns a huge value for τ_{os}, which is in conflict with the fact that a truncated power series is only a local representation of the nonlinearity. Therefore, τ_{os} is given by:

$$\tau_{os} = \frac{-1+\sqrt{1-2a_2^2}}{2a_2}. \tag{E.5}$$

The result in (E.5) can be substituted into (E.2) to evaluate $R_{e_{acc}^{NL}}[n_0]$ which, according to the assumptions made for e, becomes:

$$\begin{aligned} R_{e_{acc}^{NL}}[n_0] = \frac{10-13a_2^2}{20}\delta[n_0] - \frac{15-37a_2^2}{45}\left(\delta[n_0+1]+\right. \\ \left.\delta[n_0-1]\right) + \frac{15-29a_2^2}{180}\left(\delta[n_0+2]+\delta[n_0-2]\right). \end{aligned} \tag{E.6}$$

Before evaluating the Fourier transform of $R_{e_{acc}^{NL}}[n_0]$, the expression (E.6) can be rewritten as:

$$\begin{aligned} R_{e_{acc}^{NL}}[n_0] = \frac{121}{180}a_2^2\delta[n_0] - \frac{8}{45}a_2^2\big(2\delta[n_0] - (\delta[n_0+1]+ \\ +\delta[n_0-1])\big) + \frac{1}{12}\left(1-\frac{29}{15}a_2^2\right)\big(6\delta[n_0]+ \\ -4(\delta[n_0+1]+\delta[n_0-1]) + \delta[n_0+2]+\delta[n_0-2]\big). \end{aligned} \tag{E.7}$$

Similarly to what we have seen while obtaining (5.5) from (5.3) and (5.4), one can deduce that the Fourier transform of (E.7) returns:

$$S_{e_{acc}^{NL}}(f) = \frac{121}{180}a_2^2 - \frac{8}{45}a_2^2\left(2\sin\left(\pi f T_s\right)\right)^2 + \frac{1}{12}\left(1-\frac{29}{15}a_2^2\right)\left(2\sin\left(\pi f T_s\right)\right)^4. \tag{E.8}$$

In conclusion, considering the expression of $S_{e_{acc}}$ in (5.5) for $l=3$, the result in (E.8) becomes that given in (5.9).

Appendix F

Evaluation of p for representative ENOP-DDSM Architectures

In Section 4.3, we discussed the possibility of predicting the spur immunity of a DDSM for a given nonlinearity, through the evaluation of the PNN. Moreover, we have analyzed and proven the level of spur immunity p listed in Table 6.1 for the case of P1. In this Appendix, we extend the analysis to the other ENOP-DDSMs presented in Table 6.1. In order to do so, we need to evaluate the probability distribution functions of e_{acc} for the ENOP modulators P2–P7. The generic procedure for the evaluation of $P(\cdot)$ was given in Appendix A. Following the same procedure for architectures P2 and P3, the predicted $P(\cdot)$ is given by:

$$P(x) = \begin{cases} \frac{1}{60}\left(33 - 30x^2 + 15x^4 - 5|x|^5\right) & \text{if } 0 \le |x| \le 1 \\ \frac{51+75|x|-210x^2+150|x|^3-45x^4+5|x|^5}{120} & \text{if } 1 \le |x| \le 2 \\ \frac{1}{120}(3-|x|)^5 & \text{if } 2 \le |x| \le 3 \\ 0 & \text{elsewhere} \end{cases} \tag{F.1}$$

Similarly, the pairs of architectures P4 and P5 also share a common $P(\cdot)$ which is expressed in (F.2)[1].

$$P(x) = \begin{cases} \frac{2416-1680x^2+560x^4-140x^6+35|x|^7}{5040} & \text{if } 0 \leq |x| \leq 1 \\ \frac{2472-392|x|-504x^2-1960|x|^3+2520x^4-1176|x|^5+252x^6-21|x|^7}{5040} & \text{if } 1 \leq |x| \leq 2 \\ \frac{-1112+12152|x|-19320x^2+13720|x|^3-5320x^4+1176|x|^5-140x^6+7|x|^7}{5040} & \text{if } 2 \leq |x| \leq 3 \\ \frac{1}{5040}(4-|x|)^7 & \text{if } 3 \leq |x| \leq 4 \\ 0 & \text{elsewhere} \end{cases} \tag{F.2}$$

Finally, the probability distribution of e_{acc}, for cases P6 and P7 is given in (F.3).

---

[1] All the probability density functions provided in this appendix have been calculated with the aid of Wolfram Mathematica [65].

$$P(x) = \begin{cases} \frac{78095-44100x^2+11970x^4-2100x^6+315x^8-63|x|^9}{181440} & \text{if } 0 \leq |x| \leq 1 \\ \frac{77990+945|x|-47880x^2+8820|x|^3-1260x^4+13230|x|^5-10920x^6+3780|x|^7-630x^8+42|x|^9}{181440} & \text{if } 1 \leq |x| \leq 2 \\ \frac{108710-137295|x|+228600x^2-313740|x|^3+240660x^4-107730|x|^5+29400x^6-4860|x|^7+450x^8-18|x|^9}{181440} & \text{if } 2 \leq |x| \leq 3 \\ \frac{-668315+2382615|x|-3085740x^2+2128140|x|^3-896490x^4+243810|x|^5-43260x^6+4860|x|^7-315x^8+9|x|^9}{362880} & \text{if } 3 \leq |x| \leq 4 \\ \frac{1}{362880}(5-|x|)^9 & \text{if } 4 \leq |x| \leq 5 \\ 0 & \text{elsewhere} \end{cases} \qquad (\text{F.3})$$

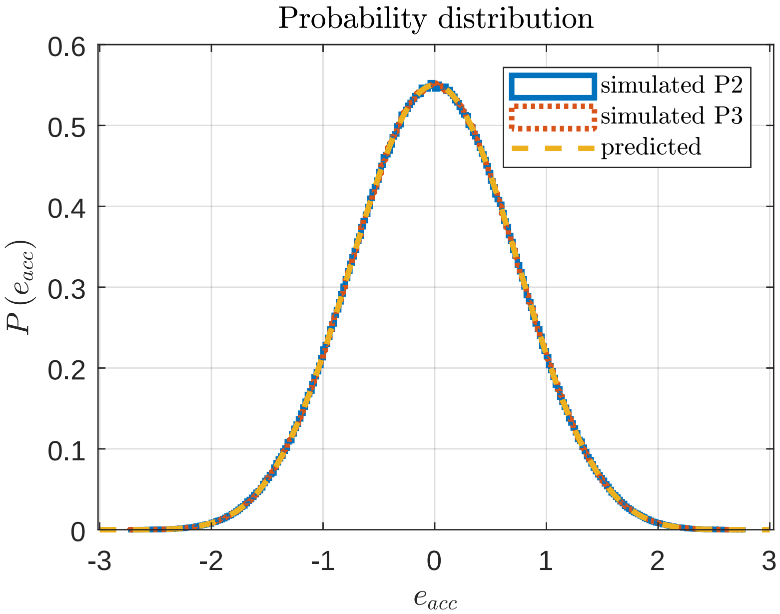

Figure F.1: Predicted and simulated probability distribution of e_{acc} in the cases of P2 and P3 ENOP-DDSMs; $r = 3$.

The predicted probability distributions shown in (F.1)–(F.3) are compared to simulation results in Figs. F.1, F.2 and F.3, respectively. Notice that all the simulated distributions $P(e_{acc})$ closely match the predictions, confirming the validity of the approximation made about e_{acc}.

Let us now evaluate the the spur immunity order, p, of P2 and P3 ENOP-DDSM architectures. The PNN can be evaluated from the definitions in (2.14)–(2.16), (4.4) and the expression for the predicted $P(\cdot)$ given in (F.1). If we assume a generic fifth-order nonlinearity expressed as $\mathcal{N}(x) = \sum_{i=0}^{5} a_i x^i$, we obtain:

$$\begin{aligned} PNN[n] = a_0 + a_1\tau_{os} + a_2\left(\frac{1}{2} + \tau_{os}^2\right) + a_3\left(\frac{3}{2}\tau_{os} + \tau_{os}^3\right) + \\ + a_4\left(\frac{7}{10} + 3\tau_{os}^2 + \tau_{os}^4\right) + a_5\left(\frac{7}{2}\tau_{os} + 5\tau_{os}^3 + \tau_{os}^5\right) \end{aligned} \quad \text{(F.4)}$$

The resulting PNN is independent of n. As discussed in Section 4.3, this means that the system does not experience fractional spurs and, therefore, that the

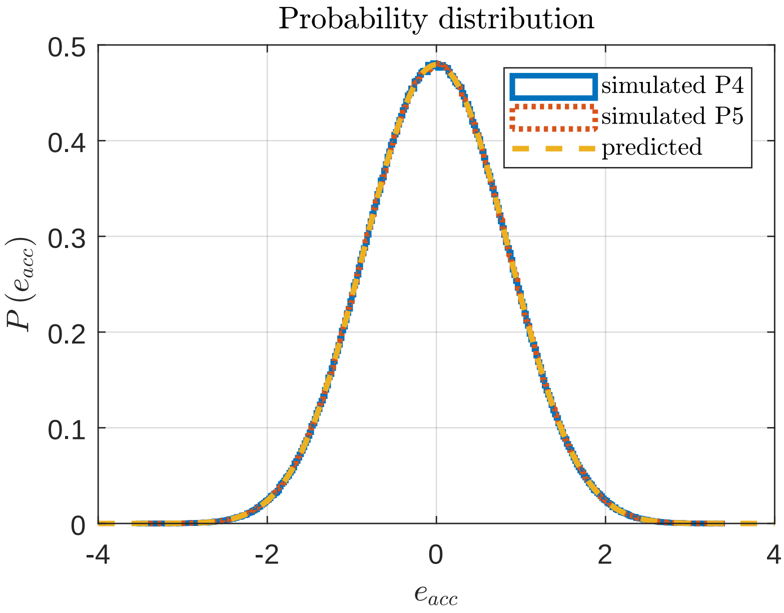

Figure F.2: Predicted and simulated probability distribution of e_{acc} in the cases of P4 and P5 ENOP-DDSMs; $r = 4$.

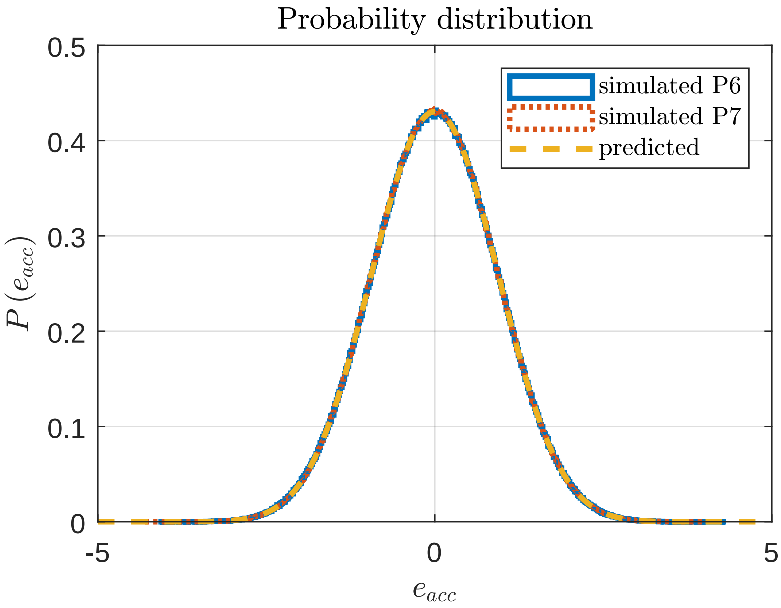

Figure F.3: Predicted and simulated probability distribution of e_{acc} in the cases of P6 and P7 ENOP-DDSMs; $r = 5$.

P2 and P3 ENOP-DDSMs provide a level of spur immunity p equal to 5, as anticipated in Table 6.1.

Then, we analyze the cases of P4 and P5 architectures. They share the same probability distribution function for e_{acc}, which is given in (F.2). Following the same procedure for evaluating the PNN and considering a seventh-order nonlinearity, $\mathcal{N}(x) = \sum_{i=0}^{7} a_i x^i$, one finds that:

$$\begin{aligned} PNN[n] = {} & a_0 + a_1\tau_{os} + a_2\left(\frac{2}{3} + \tau_{os}^2\right) + a_3(2\tau_{os} + \tau_{os}^3) + a_4\left(\frac{19}{15} + 4\tau_{os}^2 + \tau_{os}^4\right) + \\ & + a_5\left(\frac{19}{5}\tau_{os} + \frac{20}{3}\tau_{os}^3 + \tau_{os}^5\right) + a_6\left(\frac{80}{21} + 19\tau_{os}^2 + 10\tau_{os}^4 + \tau_{os}^6\right) + \\ & + a_7\left(\frac{80}{3}\tau_{os} + \frac{133}{3}\tau_{os}^3 + 14\tau_{os}^5 + \tau_{os}^7\right), \end{aligned} \tag{F.5}$$

which is again independent of n. This result confirms that P4 and P5 architectures achieve $p = 7$.

Lastly, we consider the cases of P6 and P7 ENOP-DDSMs. In Table 6.1, we stated that these architectures achieve spur immunity for polynomials up to ninth order. To prove this, let us consider a nonlinearity $\mathcal{N}(x) = \sum_{i=0}^{9} a_i x^i$. Then, we evaluate the PNN using the expression of $P(\cdot)$ given in (F.3). Doing so, one obtains:

$$\begin{aligned} PNN[n] = {} & a_0 + a_1\tau_{os} + a_2\left(\frac{5}{6} + \tau_{os}^2\right) + a_3\left(\frac{5}{2}\tau_{os} + \tau_{os}^3\right) + a_4\left(2 + 5\tau_{os}^2 + \tau_{os}^4\right) + \\ & + a_5\left(10\tau_{os} + \frac{25}{3}\tau_{os}^3 + \tau_{os}^5\right) + a_6\left(\frac{215}{28} + 30\tau_{os}^2 + \frac{25}{2}\tau_{os}^4 + \tau_{os}^6\right) + \\ & + a_7\left(\frac{215}{4}\tau_{os} + 70\tau_{os}^3 + \frac{35}{2}\tau_{os}^5 + \tau_{os}^7\right) + a_8\left(\frac{713}{18} + 215\tau_{os}^2 + 140\tau_{os}^4 + \right. \\ & \left. + \frac{70}{3}\tau_{os}^6 + \tau_{os}^8\right) + a_9\left(\frac{713}{2}\tau_{os} + 645\tau_{os}^3 + 252\tau_{os}^5 + 30\tau_{os}^7 + \tau_{os}^9\right) \end{aligned} \tag{F.6}$$

This shows that the PNN is constant and confirms that architectures P6 and P7 are immune from spurious tones in the case of polynomial nonlinearities with order up to nine. It should be clear that the method can be extended to higher orders albeit with more terms in the expressions for $P(x)$ and $PNN[n]$.

Appendix G

Evaluation of hardware cost and operating speed for different ENOP-related architectures

In this appendix we give further details on how we calculated the hardware cost and operating speed results shown in Table G.1. In order to perform such evaluations we will use the results shown in [71], while calculating the cost in terms of 1-bit flip flops and 1-bit full-adders separately.

G.1 Hardware cost

Let us first evaluate the hardware costs of the different 20-bit modulators listed in Table G.1. The MASH 1-1-1 is composed of three EFM1 stages, each of which requires a 20-bit register and a 20-bit adder. Furthermore, an error feedback modulator is employed which requires an additional three flip flops and five full-adders. If we denote as C_{FF} the unit hardware cost of a 1-bit flip flop and as C_{add} that of a 1-bit full-adder, one would obtain that a 20-bit MASH 1-1-1 costs

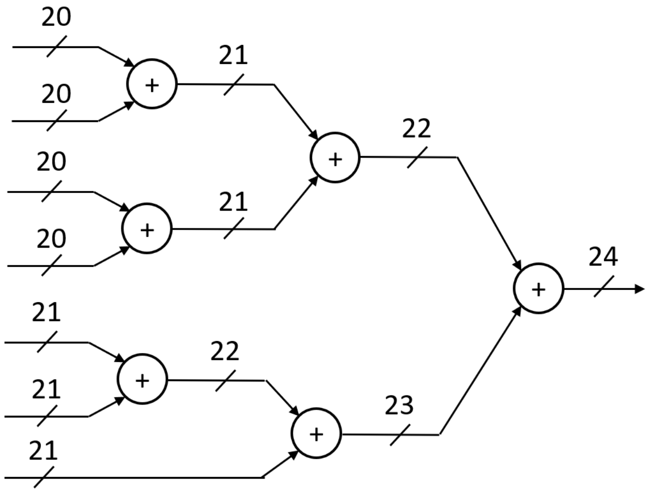

Figure G.1: Block diagram of a proposed implementation of the 7 addends addition in the SQ P3 modulator.

$63C_{FF} + 65C_{add}$.

Next, we consider the SQ P3 ENOP which is shown in Fig. 7.4. It requires seven 20-bit registers, and must add together 7 addends. The latter can be implemented with 6 full-adders with different sizes. In fact, some of the addends are scaled by factor of ±2. Moreover, since more than two addends are summed, some of the adders are required to have a larger width in order not to overflow. The diagram showing a proposed implementation of such addition is given in Fig. G.1 We have estimated that, in order to implement the additions correctly, two 20-bit full-adders, two 21-bit full-adders, one 22-bit full-adder and one 23-bit full-adder are required. It is worth noting that the SQ configuration does not require an error cancellation network. Therefore, the 20-bit SQ P3 ENOP modulator costs $120C_{FF} + 127C_{add}$.

Next we consider the P3 ENOP cascaded structure shown in Fig. 7.5(a). As discussed previously, the first two 20-bit EFM1s lead to a cost of $40C_{FF} + 40C_{add}$. The last stage instead is more complex and requires five 20-bit registers, two 20-bit

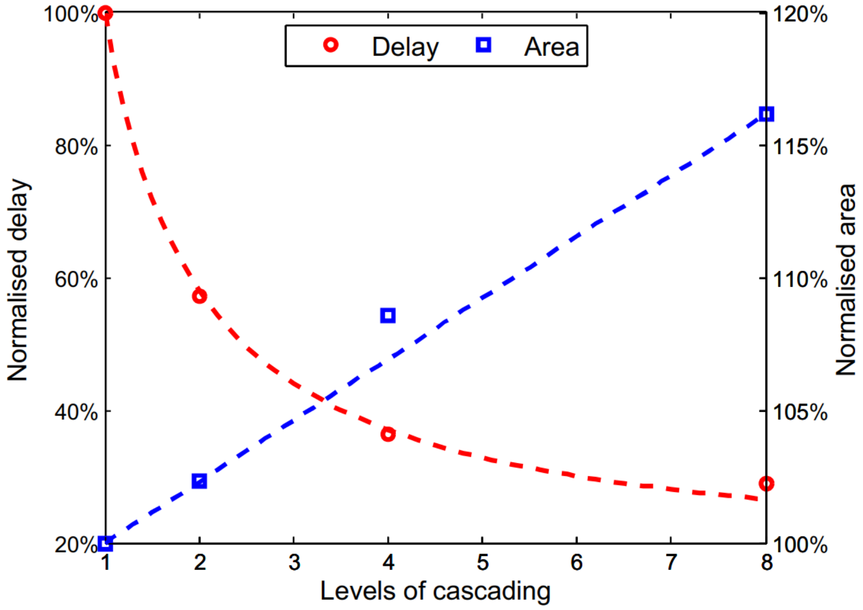

Figure G.2: Results reported in [71, Fig. 5] that show the trade-off in the nested cascaded MASH 1-1-1 between speed and area for various levels of cascading.

full-adders and one 21-bit full-adder. Moreover, the error cancellation network can be implemented with six flip-flops and seven 1-bit full-adders. Adding up, we obtain a total hardware cost of $146C_{FF} + 108C_{add}$.

The evaluation of the hardware cost of a two-level NC P3 ENOP is obtained using the results in [71]. In particular, we use the results reported in Fig. G.2. It shows that, for a two-level NC MASH 1-1-1, one should expect a 2% increase in area. Then, since the first two stages of the NC P3 ENOP in Fig. 7.7 share a similar structure to an NC MASH 1-1-1, we would expect a similar increase of area that is $(63C_{FF} + 65C_{add}) \times 2\% \approx C_{FF} + C_{add}$. In addition to that, the nested cascading of the last stage of the P3 ENOP requires more hardware, since the signal $y_{B,3}[n]$ in Fig. 7.7 is not expressed on a single bit. In particular, three 1-bit full-adders and nine 1-bit half-adders are required with an approximate cost of $8C_{add}$[1]. Therefore, the overall hardware cost of a 20-bit NC P3 ENOP with $j = 2$ and $N_A = 10$ amounts to $147C_{FF} + 117C_{add}$.

Lastly, we need to evaluate the hardware cost of a 20-bit hybrid two-level NC MASH-ENOP with $N_A = 2$. This means that the auxiliary has a hardware cost of an 18-bit MASH 1-1-1, that can be calculated to be $54C_{FF} + 54C_{add}$. The cost of the primary and the related error cancellation network can be evaluated as the hardware cost of a 2-bit cascaded P3 ENOP with $j = 2$, that amounts to $20C_{FF} + 18C_{add}$. Then, an additional cost of $(63C_{FF} + 65C_{add}) \times 2\%$ has to be taken in account for the nested cascading structure, leading to a total of $75C_{FF} + 73C_{add}$.

G.2 Operating speed

Let us evaluate now the operating speed of the aforementioned modulator architectures. These will be calculated and normalized to that of a MASH 1-1-1. The speed of a MASH modulator is limited by the operation in the single stages and can be evaluated as a function of two delays, namely the delay through the multi-bit adder and the delay due to the output flip flop [71]. In particular, in the case of a MASH 1-1-1, the total delay, denoted by D, is equal to:

$$D = D_{FF} + D_{add}, \tag{G.1}$$

where D_{FF} is the delay of a flip-flop and D_{add} is the delay of the adder of each EFM1. The authors in [71] show that, when the MASH modulator is nested cascaded in two evenly-split levels, the delay of the modulator reduces $\approx D_{FF} + D_{add}/2$. Moreover, the results in Fig. G.2 show that the delay decreases

---

[1] We assume that the hardware cost of an half-adder is half that of a full-adder.

to ≈ 57.5% when two levels of cascading are used. Therefore, we can write that:

$$D_{FF} + \frac{D_{add}}{2} \approx 0.575 \left(D_{FF} + D_{add} \right). \tag{G.2}$$

From the results in (G.1) and (G.2), one can obtain that:

$$D_{add} \approx 0.85D, \tag{G.3}$$

$$D_{FF} \approx 0.15D. \tag{G.4}$$

That being said, we can now evaluate the speed of the SQ P3 ENOP. According to the implementation of the addition discussed above, we notice that the largest combinatorial delay is set by three adders of 21, 22 and 23 bits, respectively. According to (G.2) and (G.3), and considering that D_{add} is evaluated for a 20-bit adder, one can obtain that:

$$D_{SQ} = \frac{21}{20} D_{add} + \frac{22}{20} D_{add} + \frac{23}{20} D_{add} + D_{FF} \approx 2.96D, \tag{G.5}$$

where D_{SQ} is the maximum delay in the SQ P3 ENOP. This result leads to an operating speed of approximately 34% that of the MASH 1-1-1.

In the case of the cascaded P3 ENOP modulator with $j = 2$, the speed is limited by the third stage which provides a maximum delay of a 20-bit adders, a 21-bit adder and a flip-flop. In this case, the total delay is $\approx 1.89D$, which returns a speed of 53% that of the MASH 1-1-1.

In the case of a nested cascaded P3 ENOP modulator with $j = 2$ and $N_A = 10$, the speed is limited by the third stage. In particular, the delay of each level of the third stage is characterized by a 10-bit adder, an 11-bit adder and a flip-flop. Moreover, an extra adder is placed in the first level because of the addition of $y_{B,3}[n]$, as explained before. The delay of the latter adder is obtained while assuming that the delay of a half-adder is half that of a full-adder. Then, the maximum delay can be evaluated as:

$$D_{NC} = \frac{10}{20} D_{add} + \frac{11}{20} D_{add} + \frac{7.5}{20} D_{add} + D_{FF} \approx 1.36D, \tag{G.6}$$

which leads to an operating speed of 73% that of the MASH 1-1-1.

Lastly, we consider the case of the hybrid NC MASH-P3 ENOP with $N_A = 2$. Even though the primary modulator is more complex and requires more additions than the auxiliary, the latter is going to limit the operating speed because it has a much larger number of bits. Then, the maximum delay is set by an 18-bit adder and a flip-flop, that is equal to $0.92D$, leading to an operating speed of 109% that of a MASH 1-1-1.

Table G.1: Hardware cost and operating speed normalized to that of a MASH 1-1-1 DDSM with $N = 20$.

DDSM	Hardware cost		Operating speed
	Flip-flops	Adders	
MASH 1-1-1	100%	100%	100%
SQ P3 ENOP	222%	195%	34%
Cascaded P3 ENOP ($j = 2$)	232%	166%	53%
Two-level NC P3 ENOP ($j = 2$, $N_A = 10$)	233%	180%	73%
Hybrid two-level NC MASH-ENOP ($N_A = 2$)	119%	112%	109%

References

[1] B. Miller and R. J. Conley, "A multiple modulator fractional divider," *IEEE Trans Instrum. Meas.*, vol. 40, no. 3, pp. 578–583, 1991.

[2] T. A. D. Riley, M. A. Copeland, and T. A. Kwasniewski, "Delta-Sigma modulation in fractional-N frequency synthesis," *IEEE J. Solid-State Circuits*, vol. 28, no. 5, pp. 553–559, May 1993.

[3] *ADF 4159 Direct Modulation/Fast Waveform Generating, 13 GHz, Fractional-N Frequency Synthesizer*, Analog Devices, Accessed: Dec. 17, 2019. [Online]. Available: https://www.analog.com/media/en/technical-documentation/data-sheets/ADF4159.pdf

[4] *ADF4356: 6.8 GHz Wideband Synthesizer with Integrated VCO* , Analog Devices, Accessed: Apr. 16, 2020. [Online]. Available: https://www.analog.com/media/en/technical-documentation/data-sheets/ADF4356.pdf

[5] H. Arora, N. Klemmer, J. C. Morizio, and P. D. Wolf, "Enhanced phase noise modeling of fractional-N frequency synthesizers," *IEEE Transactions on Circuits and Systems I: Regular Papers*, vol. 52, no. 2, pp. 379–395, Feb. 2005.

[6] H. Hedayati, B. Bakkaloglu, and W. Khalil, "Closed-loop nonlinear modeling of wideband $\Sigma\Delta$ fractional-N frequency synthesizers," *IEEE Transactions*

on Microwave Theory and Techniques, vol. 54, no. 10, pp. 3654–3663, Oct. 2006.

[7] V. Mazzaro and M. P. Kennedy, "Observations concerning "horn spurs" in a MASH-based fractional-N CP-PLL," in *2019 26th IEEE International Conference on Electronics, Circuits and Systems (ICECS).* IEEE, 2019, pp. 17–20.

[8] D. Mai, H. Mo, and M. P. Kennedy, "Observations and analysis of wandering spurs in MASH-based fractional-N frequency synthesizers," *IEEE Transactions on Circuits and Systems II: Express Briefs*, vol. 65, no. 5, pp. 662–666, May 2018.

[9] D. Mai and M. P. Kennedy, "Analysis of wandering spur patterns in a fractional-N frequency synthesizer with a MASH-based divider controller," *IEEE Transactions on Circuits and Systems I: Regular Papers*, vol. 67, no. 3, pp. 729–742, Mar. 2020.

[10] ——, "Influence of initial condition on wandering spur pattern in a MASH-based fractional-N frequency synthesizer," *IEEE Transactions on Circuits and Systems II: Express Briefs*, vol. 67, no. 12, pp. 2968–2972, Dec. 2020.

[11] D. Mai and M. P. Kennedy, "MASH-based divider controllers for mitigation of wandering spurs in a fractional-N frequency synthesizer," *IEEE Transactions on Circuits and Systems I: Regular Papers*, vol. 68, no. 1, pp. 126–137, 1 2021.

[12] L. Grimaldi, D. Cherniak, W. Grollitsch, and R. Nonis, "Analysis of spurs impact in PLL-based FMCW radar systems," in *2020 IEEE International Symposium on Circuits and Systems (ISCAS).* IEEE, Oct. 2020.

[13] V. Mazzaro and M. P. Kennedy, “Mitigation of “horn spurs” in a MASH-based fractional-N CP-PLL,” *IEEE Transactions on Circuits and Systems II: Express Briefs*, vol. 67, no. 5, pp. 821–825, 2020.

[14] ——, “Spur immunity in MASH-based fractional-N CP-PLLs with polynomial nonlinearities,” *IEEE Transactions on Circuits and Systems I: Regular Papers*, pp. 1–12, 2021.

[15] ——, “Folded noise prediction in nonlinear fractional-N frequency synthesizers,” *IEEE Transactions on Circuits and Systems I: Regular Papers*, pp. 1–11, 2021.

[16] ——, “A family of $\Delta\Sigma$ modulators with high spur immunity and low folded nonlinearity noise when used in fractional-N frequency synthesizers,” *IEEE Transactions on Circuits and Systems I: Regular Papers*, 2022.

[17] ——, “Immunity of ENOP-based fractional-N frequency synthesizer to wandering and horn spurs,” in *2022 17th International Conerence on PhD Reearch in Microelectronics and Electronics (PRIME)*. IEEE, 2022, pp. 1–4.

[18] ——, “Implementation of ENOP and hybrid nested ENOP divider controllers for fractional-N frequency synthesizers,” *IEEE Transactions on Circuits and Systems I: Regular Papers*, in preparation.

[19] ——, “A family of $\Delta\Sigma$ modulators with inherent spur immunity when interacting with a nonlinearity,” *IEEE Transactions on Circuits and Systems II: Express Briefs*, in preparation.

[20] M. H. Perrott, M. D. Trott, and C. G. Sodini, “A modeling approach for fractional-N frequency synthesizers allowing straightforward noise analysis,” *IEEE J. Solid-State Circuits*, vol. 37, no. 8, pp. 1028–1038, 2002.

[21] R. B. Staszewski, J. L. Wallberg, S. Rezeq, C.-M. Hung, O. E. Eliezer, S. K. Vemulapalli, C. Fernando, K. Maggio, R. Staszewski, N. Barton *et al.*, "All-digital PLL and transmitter for mobile phones," *IEEE journal of Solid-State circuits*, vol. 40, no. 12, pp. 2469–2482, 2005.

[22] S. Levantino, G. Marzin, and C. Samori, "An adaptive pre-distortion technique to mitigate the DTC nonlinearity in digital PLLs," *IEEE Journal of Solid-State Circuits*, vol. 49, no. 8, pp. 1762–1772, 2014.

[23] K. Raczkowski, N. Markulic, B. Hershberg, and J. Craninckx, "A 9.2–12.7 GHz wideband fractional-N subsampling PLL in 28 nm cmos with 280 fs rms jitter," *IEEE Journal of Solid-State Circuits*, vol. 50, no. 5, pp. 1203–1213, 2015.

[24] B. Razavi, *Design of Analog CMOS Integrated Circuits*, 1st ed. New York, NY, USA: McGraw-Hill, Inc., 2001.

[25] S. Pamarti and I. Galton, "LSB dithering in MASH delta–sigma D/A converters," *IEEE Transactions on Circuits and Systems I: Regular Papers*, vol. 54, no. 4, pp. 779–790, 2007.

[26] F. Bizzarri, A. M. Brambilla, and S. Callegari, "On the mechanisms governing spurious tone injection in fractional PLLs," *IEEE Transactions on Circuits and Systems II: Express Briefs*, vol. 64, no. 11, pp. 1267–1271, 2016.

[27] D. Biswas and T. K. Bhattacharyya, "Spur reduction architecture for multi-phase fractional PLLs," *IET Circuits, Devices Systems*, vol. 13, no. 8, pp. 1169–1180, 2019.

[28] H. Arora, N. Klemmer, J. C. Morizio, and P. D. Wolf, "Enhanced phase noise modeling of fractional-N frequency synthesizers," *IEEE Transactions on Circuits and Systems I: Regular Papers*, vol. 52, no. 2, pp. 379–395, 2005.

[29] B. De Muer and M. S. Steyaert, “A CMOS monolithic $\Delta\Sigma$-controlled fractional-N frequency synthesizer for DCS-1800,” *IEEE Journal of Solid-State Circuits*, vol. 37, no. 7, pp. 835–844, 2002.

[30] ——, “On the analysis of $\Delta\Sigma$ fractional-N frequency synthesizers for high-spectral purity,” *IEEE Transactions on Circuits and Systems II: Analog and Digital Signal Processing*, vol. 50, no. 11, pp. 784–793, 2003.

[31] P. V. Brennan, H. Wang, D. Jiang, and P. M. Radmore, “A new mechanism producing discrete spurious components in fractional-n frequency synthesizers,” *IEEE Transactions on Circuits and Systems I: Regular Papers*, vol. 55, no. 5, pp. 1279–1288, 2008.

[32] Y. Donnelly and M. P. Kennedy, “Prediction of phase noise and spurs in a nonlinear fractional-N frequency synthesizer,” *IEEE Transactions on Circuits and Systems I: Regular Papers*, vol. 66, no. 11, pp. 4108–4121, 2019.

[33] A. Swaminathan, A. Panigada, E. Masry, and I. Galton, “A digital requantizer with shaped requantization noise that remains well behaved after nonlinear distortion,” *IEEE Transactions on Signal Processing*, vol. 55, no. 11, pp. 5382–5394, 2007.

[34] *Microwave Wideband Synthesizer with Integrated VCO*, Analog Devices, Accessed: Oct. 18, 2020. [Online]. Available: https://www.analog.com/media/en/technical-documentation/data-sheets/adf4371.pdf

[35] K. Hosseini and M. P. Kennedy, *Minimizing Spurious Tones in Digital Delta-Sigma Modulators.* Springer Science & Business Media, 2011.

[36] V. Mazzaro and M. P. Kennedy, “Another moving spur phenomenon observed in a MASH-based fractional-N PLL,” in *2019 30th Irish Signals and Systems Conference (ISSC).* IEEE, 2019, pp. 1–5.

[37] D. Banerjee, *PLL performance, simulation and design.* Dog Ear Publishing, 2006.

[38] K. Hosseini and M. Kennedy, "Maximum sequence length mash digital delta sigma modulators," *IEEE Transactions on Circuits and Systems I*, vol. 54, no. 12, pp. 2628–2638, Dec 2007.

[39] S. E. Meninger and M. H. Perrott, "A 1-MHz bandwidth 3.6-GHz 0.18-μm CMOS fractional-N synthesizer utilizing a hybrid PFD/DAC structure for reduced broadband phase noise," *IEEE Journal of Solid-State Circuits*, vol. 41, no. 4, pp. 966–980, 2006.

[40] L. Zhang, X. Yu, Y. Sun, W. Rhee, D. Wang, Z. Wang, and H. Chen, "A hybrid spur compensation technique for finite-modulo fractional-N phase-locked loops," *IEEE journal of solid-state circuits*, vol. 44, no. 11, pp. 2922–2934, 2009.

[41] E. Temporiti, G. Albasini, I. Bietti, R. Castello, and M. Colombo, "A 700-KHz bandwidth $\Sigma\Delta$ fractional synthesizer with spurs compensation and linearization techniques for WCDMA applications," *IEEE Journal of Solid-State Circuits*, vol. 39, no. 9, pp. 1446–1454, 2004.

[42] E. Familier and I. Galton, "A fundamental limitation of DC-free quantization noise with respect to nonlinearity-induced spurious tones," *IEEE Transactions on Signal Processing*, vol. 61, no. 16, pp. 4172–4180, 2013.

[43] ——, "Second and third-order noise shaping digital quantizers for low phase noise and nonlinearity-induced spurious tones in fractional-N PLLs," *IEEE Transactions on Circuits and Systems I: Regular Papers*, vol. 63, no. 6, pp. 836–847, 2016.

[44] C.-W. Yao, R. Ni, C. Lau, W. Wu, K. Godbole, Y. Zuo, S. Ko, N.-S. Kim, S. Han, I. Jo *et al.*, “A 14-nm 0.14-ps rms fractional-N digital PLL with a 0.2-ps resolution ADC-assisted coarse/fine-conversion chopping TDC and TDC nonlinearity calibration,” *IEEE Journal of Solid-State Circuits*, vol. 52, no. 12, pp. 3446–3457, 2017.

[45] E. Familier and I. Galton, “Second and third-order successive requantizers for spurious tone reduction in low-noise fractional-N PLLs,” in *2017 IEEE Custom Integrated Circuits Conference (CICC)*. IEEE, 2017, pp. 1–4.

[46] Y. Donnelly, M. P. Kennedy, J. Breslin, S. Tulisi, S. Patil, C. Curtin, S. Brookes, B. Shelly, P. Griffin, and M. Keaveney, “4.48-GHz fractional-N frequency synthesizer with spurious-tone suppression via probability mass redistribution,” *IEEE Solid-State Circuits Letters*, vol. 2, no. 11, pp. 264–267, 2019.

[47] M. Kozak and I. Kale, “A pipelined noise shaping coder for fractional-N frequency synthesis,” *IEEE Transactions on Instrumentation and Measurement*, vol. 50, no. 5, pp. 1154–1161, 2001.

[48] M. J. Borkowski, T. A. D. Riley, J. Hakkinen, and J. Kostamovaara, “A practical Δ-Σ modulator design method based on periodical behavior analysis,” *IEEE Transactions on Circuits and Systems II: Express Briefs*, vol. 52, no. 10, pp. 626–630, 2005.

[49] B. De Muer and M. Steyaert, *CMOS fractional-N synthesizers: design for high spectral purity and monolithic integration.* Springer Science & Business Media, 2006, vol. 724.

[50] S. Pavan, R. Schreier, and G. C. Temes, *Understanding delta-sigma data converters.* John Wiley & Sons, 2017.

[51] B. Razavi, "An alternative analysis of noise folding in fractional-N synthesizers," in *2018 IEEE International Symposium on Circuits and Systems (ISCAS)*, 2018, pp. 1–4.

[52] A. Buck, "Phase Noise to Jitter," https://www.mathworks.com/matlabcentral/fileexchange/22038-phase-noise-to-jitter, MATLAB Central File Exchange. Retrieved January 22, 2021.

[53] S. Pamarti, L. Jansson, and I. Galton, "A wideband 2.4-GHz delta-sigma fractional-N PLL with 1-Mb/s in-loop modulation," *IEEE Journal of Solid-State Circuits*, vol. 39, no. 1, pp. 49–62, 2004.

[54] H.-M. Chien, T.-H. Lin, B. Ibrahim, L. Zhang, M. Rofougaran, A. Rofougaran, and W. J. Kaiser, "A 4GHz fractional-N synthesizer for IEEE 802.11a," in *2004 Symposium on VLSI Circuits. Digest of Technical Papers (IEEE Cat. No. 04CH37525)*. IEEE, 2004, pp. 46–49.

[55] K. Hosseini, M. P. Kennedy, S. H. Lewis, and B. C. Levy, "Prediction of the spectrum of a digital delta–sigma modulator followed by a polynomial nonlinearity," *IEEE Transactions on Circuits and Systems I: Regular Papers*, vol. 57, no. 8, pp. 1905–1913, 2010.

[56] B. Razavi, "An alternative analysis of noise folding in fractional-N synthesizers," in *2018 IEEE International Symposium on Circuits and Systems (ISCAS)*, 2018, pp. 1–4.

[57] R. Price, "A useful theorem for nonlinear devices having gaussian inputs," *IRE Transactions on Information Theory*, vol. 4, no. 2, pp. 69–72, 1958.

[58] S. B. Sleiman, J. G. Atallah, S. Rodriguez, A. Rusu, and M. Ismail, "Optimal $\Sigma\Delta$ modulator architectures for fractional-N frequency synthesis," *IEEE*

transactions on very large scale integration (VLSI) systems, vol. 18, no. 2, pp. 194–200, 2009.

[59] X. Huang, B. Wang, W. Rhee, and Z. Wang, "A 5.4 GHz $\Delta\Sigma$ bang-bang PLL with 19dB in-band noise reduction by using a nested PLL filter," in *2020 International Symposium on VLSI Design, Automation and Test (VLSI-DAT)*. IEEE, 2020, pp. 1–2.

[60] S. Pamarti, J. Welz, and I. Galton, "Statistics of the quantization noise in 1-bit dithered single-quantizer digital delta–sigma modulators," *IEEE Transactions on Circuits and Systems I: Regular Papers*, vol. 54, no. 3, pp. 492–503, 2007.

[61] F. M. Dekking, C. Kraaikamp, H. P. Lopuhaä, and L. E. Meester, *A Modern Introduction to Probability and Statistics: Understanding why and how.* Springer Science & Business Media, 2005.

[62] N. Wiener *et al.*, "Generalized harmonic analysis," *Acta mathematica*, vol. 55, pp. 117–258, 1930.

[63] A. Khintchine, "Korrelationstheorie der stationären stochastischen prozesse," *Mathematische Annalen*, vol. 109, no. 1, pp. 604–615, 1934.

[64] I. Florescu, *Probability and stochastic processes.* John Wiley & Sons, 2014.

[65] W. R. Inc., "Mathematica, Version 12.2," champaign, IL, 2020. [Online]. Available: https://www.wolfram.com/mathematica

[66] H. Park, C. Hwang, T. Seong, Y. Lee, and J. Choi, "A 365fsrms-jitter and -63dBc-fractional spur 5.3GHz-ring-DCO-based fractional-N DPLL using a DTC second/third- order nonlinearity cancelation and a probability-density-

shaping ΔΣM," in *2021 IEEE International Solid- State Circuits Conference (ISSCC)*, vol. 64, 2021, pp. 442–444.

[67] E. Familier, C. Venerus, and I. Galton, "A class of quantizers with DC-free quantization noise and optimal immunity to nonlinearity-induced spurious tones," *IEEE Transactions on Signal Processing*, vol. 61, no. 17, pp. 4270–4283, 2013.

[68] H. Hernandez, "Multivariate probability theory: Determination of probability density functions," *ForsChem Research Reports*, vol. 13, 2017.

[69] G. Casella and R. L. Berger, *Statistical inference.* Cengage Learning, 2021.

[70] V. Mazzaro and M. P. Kennedy, "A family of ΔΣ modulators with high spur immunity and low folded nonlinearity noise when used in fractional-N frequency synthesizers," *IEEE Transactions on Circuits and Systems I: Regular Papers*, pp. 1–10, 2021.

[71] Y. Donnelly, H. Mo, and M. P. Kennedy, "High-speed nested cascaded MASH digital delta-sigma modulator-based divider controller," in *2018 IEEE International Symposium on Circuits and Systems (ISCAS)*, 2018, pp. 1–5.

[72] Z. Li, H. Mo, and M. P. Kennedy, "Comparative spur performance of a fractional-n frequency synthesizer with a nested MASH-SQ3 divider controller in the presence of memoryless piecewise-linear and polynomial nonlinearities," in *25th IET Irish Signals Systems Conference 2014 and 2014 China-Ireland International Conference on Information and Communications Technologies (ISSC 2014/CIICT 2014)*, 2014, pp. 374–379.

[73] B. Fitzgibbon, M. P. Kennedy, and F. Maloberti, "Hardware reduction in digital delta-sigma modulators via bus-splitting and error masking—Part

I: Constant input," *IEEE Transactions on Circuits and Systems I: Regular Papers*, vol. 58, no. 9, pp. 2137–2148, 2011.

[74] ——, "Hardware reduction in digital delta-sigma modulators via bus-splitting and error masking—Part II: Non-constant input," *IEEE Transactions on Circuits and Systems I: Regular Papers*, vol. 59, no. 9, pp. 1980–1991, 2012.

[75] J. Zhuang, K. Waheed, and R. B. Staszewski, "Design of spur-free $\Delta\Sigma$ frequency tuning interface for digitally controlled oscillators," *IEEE Transactions on Circuits and Systems II: Express Briefs*, vol. 62, no. 1, pp. 46–50, 2015.

[76] E. Alvarez-Fontecilla, C. Venerus, and I. Galton, "Multi-rate DEM with mismatch-noise cancellation for DCOs in digital PLLs," *IEEE Transactions on Circuits and Systems I: Regular Papers*, vol. 65, no. 10, pp. 3125–3137, 2018.

[77] W. R. Bennett, "Spectra of quantized signals," *The Bell System Technical Journal*, vol. 27, no. 3, pp. 446–472, 1948.

[78] R. M. Gray and D. L. Neuhoff, "Quantization," *IEEE transactions on information theory*, vol. 44, no. 6, pp. 2325–2383, 1998.

[79] R. Wannamaker, S. Lipshitz, J. Vanderkooy, and J. Wright, "A theory of nonsubtractive dither," *IEEE Transactions on Signal Processing*, vol. 48, no. 2, pp. 499–516, 2000.

[80] R. Gray and T. Stockham, "Dithered quantizers," *IEEE Transactions on Information Theory*, vol. 39, no. 3, pp. 805–812, 1993.